

Techniques for Pixelated Ambipolar-Sensitive Semiconductor Gamma-Ray Spectrometers

by

Charles Olson Leak

A dissertation submitted in partial fulfillment
of the requirements for the degree of
Doctor of Philosophy
(Nuclear Engineering and Radiological Sciences)
in the University of Michigan
2021

Doctoral Committee:

Professor Zhong He, Chair
Dr. Mark Hammig
Professor Zetian Mi
Professor David K. Wehe

The wisdom of this world is foolishness before God.

Charles Olson Leak

cleak@umich.edu

© Charles Olson Leak 2021

Acknowledgements

I would first like to acknowledge the past members of the Orion Measurements Group who developed the technology on which this work was built. I thank the current and recent members of the Orion Measurements Group for their patience with me and for their discussion, honest feedback, and timely contributions over the years which made this work possible. I want to specifically acknowledge Professor Zhong He, Dr. Yuefeng Zhu, James Berry, Matthew Petryk, Erik Hall, and Dr. Sean O’Neal in this respect. I am personally so very grateful that Professor Zhong He invited me to study in this research group, and I appreciate his impeccable intellectual honesty, his professionalism, and his compassion for and desire to invest in his students.

Towards the degree for which this dissertation is submitted, I thank our professors and professors emeriti for their fascinating curricular and extracurricular instruction and discussion and for their sincere enthusiasm, and I would like to especially acknowledge Dr. Daniel Shy and Dr. Niral Shah, my academic brothers; William Steinberger; and Matthew Petryk; whose shared passion for detector physics and attention to detail made discussing work enjoyable and whose companionship made conferences and road trips delightful.

My opportunity to join this group and ultimately complete this work is a result of the favor of many who contributed to my development, but I want to recognize Dr. Adam Kellam, who first suggested I study engineering; Professor Nolan Hertel at Georgia Tech, who first gave me the opportunity to fiddle in a laboratory; and Dr. Benjamin McDonald at PNNL, who gave me my first job in the field. Above these, I am most grateful for the favor of the Lord God Almighty, my heavenly Father, whose provision and forgiveness directed me to this undertaking and allowed me to complete it despite my shortcomings.

I am especially thankful that he provided me caring friends within the department—too many to name; Christ-following peaceable roommates Malcolm Ammons and William Steinberger; a new family connected through Ann Arbor Baptist Church, whose sincerity, steadfastness, and openness has humbled me; the long-suffering

friendship of George Perkins, with whom I was never alone; and my mother, uncle, and grandmother, whose love continually encouraged me, and whose impressions, in addition to my grandfather's, are responsible for my character and ability in more ways than I understand.

Table of Contents

Acknowledgements	ii
List of Tables	vii
List of Figures	viii
Abstract	xiv
Chapter 1 Introduction and Background	1
1.1 Signal Generation	1
1.2 Position Reconstruction	2
1.3 Incomplete Charge Collection	3
1.4 Material Selection	5
1.5 Ion Migration	5
1.5.1 Thallium Bromide	5
1.5.2 Halide Perovskites	6
1.6 Auger Recombination	6
1.7 Challenges of Time-dependence	7
Chapter 2 Equipment and Procedures	9
2.1 Crystals	9
2.2 Electrode Readout	12
2.2.1 GaGe-based	12
2.2.2 ASIC-based	16
2.2.3 Bondless Connectors	16
2.3 Procedures	18
Chapter 3 Software and Processing	21
3.1 Important Functions and Data types	22
3.1.1 Accessing Waveform Files	22
3.1.2 Operating on Essences	23
3.1.3 Operating on Counts	24
3.1.4 Operating on Relations	24
3.2 Workflow	25
3.3 Processing Example	26
3.3.1 Waveform Processing	26
3.3.2 Depth Calibrations	31
3.3.3 Event Screening	33

Chapter 4	Anomalies Observed	36
4.1	Isolating Anomalous Events	36
4.1.1	Event-by-event Parameters	36
4.1.2	Distribution-determined Parameters	39
4.2	Anomalies Observed in Thallium Bromide	40
4.2.1	Transient Electron Lifetime and Leakage Current	40
4.2.2	Other Examples of Transient τ_e and IL	45
4.2.3	Binary Distributions	48
4.2.4	Localized Auger Recombination	51
4.2.5	Variable Incomplete Charge Collection	53
4.2.6	Subpixel Variations	56
4.2.7	Inter-pixel Shorting in ASIC Systems	56
4.2.8	Electrical Treeing	59
Chapter 5	Ambipolar Pixel Sensitivity	62
5.1	Simulation	62
5.1.1	Signal Induction	62
5.1.2	Novel Depth Parameter	64
5.2	Experimental Validation	65
5.2.1	Signal Induction	65
5.2.2	Novel Depth Parameter	66
Chapter 6	Treating Incomplete Charge Collection	70
6.1	Methods of Identification	70
6.1.1	Comparing Charge Reconstructions	70
6.1.2	Comparing Depth Reconstructions	75
6.2	Experimental Results	77
6.2.1	Comparing Charge Reconstructions	77
6.2.2	Comparing Depth Reconstructions	79
6.3	Inferences on Hole Transport	80
Chapter 7	Best Performance	81
7.1	Performance of TlBr	81
7.1.1	11×11-pixel Detectors	81
7.1.2	Performance Limitations	85
7.1.3	Bias and Calibration Dependence	88
7.2	Performance of CdZnTeSe	94
7.3	Performance of CsPbBr ₃	100
Chapter 8	Conclusion	104

8.1	Summary	104
8.2	Continuing Work	105
Bibliography		108

List of Tables

Table 3.1. Essences distilled directly from the raw waveforms.	28
Table 3.2. Parameters used in the instructions in Table 1.....	29
Table 3.3. Mixed essences and their origins.	30
Table 3.4. Number of bins used to represent different distributions.....	30
Table 4.1. Leakage currents through electrodes of 138BS6(R).	45
Table 4.2 Low resistance paths found between pixels of two flip-chip-bonded crystals.	59
Table 5.1. Energy resolutions from different calibrations.	69
Table 6.1. Values used to simulate waveforms.	72
Table 6.2. Fit parameters for all pixels.	80
Table 7.1. Performance of 935-38AS3 at -1250 V before and after each processing step. Improvements relative to the raw performance are shaded green.	83
Table 7.2. Energy resolutions of 128BAS3 recording Cs-137 gamma rays, self-calibrated using plane-pixel ratio and using drift duration.....	89
Table 7.3. Single-pixel drift-duration-calibrated energy resolutions of 935-38AS3.	92
Table 7.4. Depth-corrected energy resolutions of a Cs-137 source.	96
Table 7.5. Resistivity of each pixel calculated from the currents measured at positive biases.	103

List of Figures

Figure 1.1. Theoretical weighting potentials of the collecting pixel electrode (red) and the plane electrode (blue) for a 5-mm-thick detector with 1-mm pixel pitch.	2
Figure 2.1. Photo of BNL1-S2 showing unbonded face as received.....	9
Figure 2.2. Photos of BNL2-S2 showing cathode guard ring and wire bonding.....	10
Figure 2.3. Photo of a) planar perovskite crystal manufactured by Yihui He and b) pixelated perovskite crystal manufactured by Teddy Feng installed in readout system.	10
Figure 2.4. Photos of a) small and b) large crystals manufactured by RMD after electrode deposition.	11
Figure 2.5. GaGe-based readout system: a) front view, b) rear view, c) top view, lid off, d) bottom view, lid off.....	13
Figure 2.6. Circuit schematic of the GaGe-based readout system. The bottom right circuit group is repeated for all pixel connections.	13
Figure 2.7. Crystal-carrier boards compatible with the GaGe-based readout system.	14
Figure 2.8. Rendering of updated unassembled backplane of GaGe-based readout system.	15
Figure 2.9. a) Front and b) back rendering of updated crystal-carrier board for GaGe-based readout system which allows rotationally-symmetric mating with ASIC-based readout systems.....	15
Figure 2.10. Photos of a) a board with Invisipins mounted and b-c) the sandwich assembly with BNL1-S2 installed.....	17
Figure 2.11. a,b) Renders and b,c) photographs of a,c) a bondless frame without crystal and b,d) bondless frame with crystal installed, connected to an ASIC system.....	18
Figure 3.1. Distribution of waveform shapes created by superposing pixel waveforms with reconstructed amplitude greater than 6000 ADC.....	23
Figure 3.2. a) A typical workflow using the code. Begin at top, following arrows. Paths indicated by gold arrows were used to investigate anomalies. b) Expanded diagram of three functions with dependence indicated by blue arrows. Blue blocks represent code which may need to be adjusted if there are anomalies; red represents unavoidably slow code; green represents otherwise uninteresting code.	26
Figure 3.3. a) Raw waveforms and b) raw waveforms overlaid with waveform reconstructions.....	27
Figure 3.4. Distribution of pixel trapezoidal amplitudes a) univariate and b) vs. drift durations.....	31

Figure 3.5. Pixel trapezoidal amplitudes for each pixel.....	31
Figure 3.6. Bivariate distribution of prompt-final ratios and drift durations.....	32
Figure 3.7. Bivariate distributions of pixel trapezoidal amplitude and prompt-final ratio a) within a pixel-pitch of the pixel and b) at drift durations greater than 8 μ s.	32
Figure 3.8. Bivariate distribution of pixel trapezoidal amplitude and drift duration a) after prompt-final-ratio calibration and b) after an additional drift-duration calibration.....	33
Figure 3.9. a) Bivariate distribution of the plane-pixel ratios and drift durations with upper and lower boundaries defining typical relations. b) Energy spectra within and without these bounds.	34
Figure 3.10. a) Overall single-pixel and b) best-pixel energy spectrum after ICC-screening.	34
Figure 3.11. a) Relationship between iterations of photopeak-FWHM calculations for each voxel. b) Histogram of voxel resolutions after the final iteration.	35
Figure 4.1. a) Plane-pixel ratio vs. pixel amplitude and b) drift duration vs. pixel amplitude for the four pixels of BNL2-S2.	36
Figure 4.2. Drift durations vs. plane-pixel ratio for the four pixels of BNL2-S2 a) before and b) after anomalous events were removed.	37
Figure 4.3. A a) typical and b-d) atypical pixel (red) and plane (blue) waveforms from one gamma-ray interaction in TlBr and their approximations (black).	38
Figure 4.4. An example relationship between selective criterion (voxel energy resolution) and resolution, photofraction, and photopeak efficiency from 935-38AS3 (after depth corrections and screening of incomplete charge collection).	40
Figure 4.5. Cs-137 energy spectra from 1-cm-thick 138BS6(R) at -1000 V separated by depth from a) hours 1-10 and b) hours 42-51 of operation.	41
Figure 4.6. Distribution of drift durations for 138BS6(R) during hours 1-10 and 42-51 showing no increase in drift duration despite a change in photopeak amplitude.	41
Figure 4.7. Finely time-binned energy resolution from the center pixel of 138BS6(R). .	42
Figure 4.8. Self-calibrated Cs-137 energy spectra from 138BS6(R) from hours 1-10 and hours 42-51 of operation.	43
Figure 4.9. I-V curve of 138BS6(R) before operation.....	44
Figure 4.10. a) Leakage current measured through the pixels of 138BS6(R) during the beginning and end of operation over about a day a month later. b) Pixel locations.	44
Figure 4.11. Bivariate histograms showing response of 175CS5-4 over four periods during the same experimental conditions at -1200 V over 12 mm.	46
Figure 4.12. Leakage current during the measurement shown in Figure 4.11.	46
Figure 4.13. Unstable current observed in 175CS5-4.....	47
Figure 4.14. Leakage current through 171A2 showing temporary recoveries of stability.	47

Figure 4.15. Pixel map of 935-38AS3 indicating where each phenomenon was observed. Red indicates electron lifetime decrease, green indicates low-SP-region disappearance, and X indicates double peaking.	49
Figure 4.16. Bivariate histograms showing combined response of all pixels marked in green in Fig. 19 one day apart showing recovery of low-SP regions.	50
Figure 4.17. Bivariate histogram showing the response of a) pixel 58 (i.e. pixel (3,6) in Fig. 19) and b) of the plane from events which triggered pixel 58, which exhibit double peaking.	50
Figure 4.18. Count rate as a function of collimated depth showing region of low counts from all pixels after biasing.	51
Figure 4.19. Bivariate histograms showing superposed pixel waveforms (amplitude vs. digitized sample number) from a) photopeak events exhibiting Auger recombination b) ordinary photopeak events which occurred at a slightly shallower depth in 935-38AS3 at -1250 V.	52
Figure 4.20. Bivariate histogram showing response of pixel 70 from 935-38AS3 at a) -1250 V and b) -1000 V. Most pixels were similar.	52
Figure 4.21. Relation between prompt-final ratio and drift duration for pixel 70 of 935-38AS3 at -1250 V showing near-plane distortion from Auger recombination (drift durations greater than 8 μ s).	53
Figure 4.22. Bivariate histogram showing response of all pixels from 935-38AS3 during operation at -1250 V a) at the beginning of the measurement and b) over two hours into the measurement.	53
Figure 4.23. Energy spectra from 139BS3-1(R) separated by depth calculated using a) plane-pixel ratio and b) drift duration.	54
Figure 4.24. Bivariate histograms showing relations between plane-pixel ratio and pixel amplitude given events a) from a slice of the middle of the detector thickness and b) from a slice directly under the planar cathode.	54
Figure 4.25. Bivariate histograms showing relations between plane amplitude and pixel amplitude for the events shown in Figure 4.24.	55
Figure 4.26. Bivariate histograms showing depth-separated energy spectra for 171BS5-2(R) given different subpixel slices equidistant from the center of the pixel. Color scale shows counts per bin area.	56
Figure 4.27. Cell calibration of a typical channel without low-resistance paths to other channels. a) a cell's response to a pulser. b) "FWHM of cells' responses to pulser" vs. "cell index".	57
Figure 4.28. a-b) Cell calibration of one channel with a 11.6 Ω resistance path to another channel. c-d) Cell calibration of the connected channel.	58
Figure 4.29. a-b) Cell calibration of one channel with a 120.7 Ω resistance path to another channel. c-d) Cell calibration of the connected channel.	58

Figure 4.30. a-b) Cell calibration of one channel with a 12.07 k Ω resistance path to another channel. c-d) Cell calibration of the connected channel.....	58
Figure 4.31. a-b) Cell calibration of one channel with a 1.01 M Ω resistance path to another channel. c-d) Cell calibration of the connected channel.	59
Figure 4.32. a) A photo from the side and b) a series of photos with different focal lengths of TlBr crystal 150BA4 showing the electrical tree which developed during extended high bias.....	60
Figure 5.1. Theoretical pixel- (red) and plane- (blue) electrode pulse waveform pairs for events at depths throughout the detector for material with an electron-hole mobility ratio of a) 50, b) 10, c) 3, and d) 1. Dotted lines show final amplitudes excluding hole signal.	63
Figure 5.2. Relations between the new depth parameter and depth of interaction from simulated waveforms given a) high and b) low electron-hole mobility ratios and assuming electron collection time is known.	65
Figure 5.3. 200 typical pairs of photopeak pulse waveforms showing hole induced signal from interactions which occurred a) near the planar electrode and b) near the pixel electrode. Cf. Fig. 2b.....	66
Figure 5.4. Prompt-final ratio versus drift duration for all single-pixel Cs-137 gamma-ray interactions in ambipolar-sensitive TlBr. Cf. Figure 5.2.	67
Figure 5.5. Waveform amplitude versus a) plane-pixel ratio and b) prompt-final ratio for Cs-137 gamma-ray interactions within a pixel pitch of the pixel surface as determined by the drift duration.	68
Figure 5.6. Waveform amplitude vs. drift duration a) before and b) after calibration using prompt-final ratio.....	68
Figure 5.7. Cs-137 energy spectra measured by ambipolar-sensitive TlBr self-calibrated using the methods discussed.....	69
Figure 6.1. Simulated planar waveform in blue from an event which occurred at half the thickness of the detector. Components of the waveform from electron and hole motion are shown in orange and yellow.	72
Figure 6.2. Reconstruction of a unit charge from simulated waveforms from all depths of interaction (where 0 is the pixel-electrode surface) showing electron and hole components.	73
Figure 6.3. Simulated distortion of CAR reconstruction for different amounts of electron trapping.	76
Figure 6.4. Simulated distortion of CAR reconstruction for different amounts of charge leakage.	76
Figure 6.5. Charge freed under one TlBr pixel during Cs-137 flood irradiation reconstructed using the naïve method in Equation 6.2 plotted vs. interaction depth. ...	78
Figure 6.6. Energy deposited vs. f (Equation 6.13) for all events recorded by one pixel of a TlBr detector irradiated by Cs-137.	79

Figure 6.7. Energy spectra of Cs-137 gamma rays recorded by TlBr before and after screening events for ICC.	79
Figure 7.1. Overall single-pixel energy spectra from each step of processing listed in Table 3.	83
Figure 7.2. Pixel resolutions a) before any correction, b) after calibrating by PFR, c) after also calibrating by drift duration, and d) after also removing ICC events.	84
Figure 7.3. Relationship between selective criterion (voxel energy resolution) and Table 3 parameters from 935-38AS3 (after depth corrections and screening of incomplete charge collection).	85
Figure 7.4. Maximum drift duration of each pixel of 935-38AS3 during operation at -1250 V.	86
Figure 7.5. Photopeak centroid a) before depth correction and b) after depth correction for the pixels of 935-38AS3 throughout operation at -1250 V.	87
Figure 7.6. Photopeak distribution for pixel 110 as a function of time a) before depth correction and b) after depth correction.	87
Figure 7.7. Depth-separated energy spectrum from pixel 110 from the first two hours of operation a) before depth correction and b) after depth correction.	88
Figure 7.8. Raw drift-duration-separated energy spectra of Cs-137 as recorded by device 128BAS3 at a) -800 V and b) -2000 V.	89
Figure 7.9. -800 V bias (a,c) and -2000 V bias (b,d) single-pixel spectra self-calibrated using plane-pixel ratio (a,b) and using drift duration (c,d) from device 128BAS3.	90
Figure 7.10. Bias and current for high-bias (>1000 V) testing of 935-38AS3. The actual voltage applied to the planar electrode was negative.	92
Figure 7.11. Distribution of self-calibrated single-pixel energy resolutions at 662 keV for the pixels of 935-38AS3 at a) -1000 V, b) -1250 V, c) -1750 V, and d) -2000 V.	93
Figure 7.12. Distribution of self-calibrated single-pixel energy resolutions at 662 keV for the pixels of 935-38AS3 at -1250 V after thorough depth correction.	94
Figure 7.13. Total leakage current across crystal versus voltage applied to cathode showing nonlinearity.	95
Figure 7.14. Average observed electron drift time and calculated electron drift speed for each depth bin under a) pixel 1 and b) pixel 2 during day 1 at -1000 V.	95
Figure 7.15. Depth-corrected anode energy spectrum from pixel 2 on day 1 with peak (green) and continuum (red) regions marked.	97
Figure 7.16. Typical waveforms comprising the a) peak of the depth-corrected energy spectrum and b) the continuum of the depth-corrected energy spectrum.	97
Figure 7.17. Waveforms from interactions near the planar cathode showing hole collection by the cathode.	98
Figure 7.18. Drift duration vs. pixel amplitude of BNL2-S2 under Cs-137 irradiation at 10 °C and -10 V.	98

Figure 7.19. (a) Self-calibrated spectra for each pixel and (b) total single-pixel self-calibrated spectrum for BNL2-S2 at -2000 V irradiated by Cs-137 and at room temperature.	99
Figure 7.20. Energy spectrum from BNL2-S2 after screening noise triggers.	100
Figure 7.21. Co-57 spectra measured two days apart by a planar CsPbBr ₃ detector using 1 μ s shaping analog electronics. Gain may be slightly different between measurements.	101
Figure 7.22. I-V curve measured from the CsPbBr ₃ detector manufactured by Teddy Feng of UNC.	102
Figure 7.23. Leakage current components through the pixels and guard ring.	102

Abstract

Electrode pixelation of CdZnTe gamma-ray spectrometers has historically led to extraordinary energy resolutions for room-temperature operation and has enabled solid-state single-crystal Compton imaging. In this work, pixelated alternative room-temperature semiconductors, especially TlBr, were tested as gamma-ray spectrometers, and digital processing techniques were developed to improve their performance.

Pixel ambipolar (electron and hole) sensitivity was observed in TlBr, CdZnTeSe, and CsPbBr₃. The effects on traditional depth-reconstruction techniques were studied, and a technique to extract near-pixel position from the pixel waveform shape caused by ambipolar signals was devised. The new technique was implemented on TlBr spectrometers and used to perform an additional energy calibration, improving energy resolutions. This new technique may be used to probe charge transport properties on small length scales, and the improvement in resolution increases the viability of new ambipolar-sensitive spectrometers.

Several anomalies such as transient leakage currents, transient bulk electron lifetimes, and transient cathode-localized Auger recombination were observed in TlBr. Some of these anomalies necessitated an increase in trigger thresholds, raising the fraction of single-pixel events experiencing incomplete charge collection. Methods to identify and remove these events were developed accounting for ambipolar signals and applied to TlBr spectrometers, improving photofractions. These methods can be applied to other ambipolar-sensitive spectrometers, increasing their viability.

The additional energy calibration and the methods of reducing incomplete charge collection were applied to the best recent 11×11-pixel (22×22×5 mm³) TlBr detector, which improved from 4% uncalibrated to between 1.4% and 2.1% FWHM at 662 keV, dependent on the fraction of the active volume used, and improved the photofraction from 15% to 30%.

Chapter 1 Introduction and Background

Pixelated room-temperature semiconductor gamma-ray spectrometers fabricated from CdZnTe (CZT) have been commercially successful. Research is ongoing to apply similar fabrication methods and event reconstruction techniques to spectrometers of alternative materials, such as TlBr, CdZnTeSe, and halide perovskites. The hole mobility in these materials can be within an order of magnitude of electron mobility, allowing signal induction by ambipolar carriers [1]–[6].

1.1 Signal Generation

Electron-hole pairs are freed within a semiconductor crystal by a gamma-ray interaction and drift due to an externally applied electric field. The number of charge carriers freed is proportional to the energy deposited by the gamma ray. The time it takes for these charge carriers to drift some distance, Δx , can be modeled according to their mobility in the material, μ , and the electric field internal to the crystal, E , which may be perturbed by space charge:

$$t = \frac{\Delta x}{v} = \frac{\Delta x}{\mu E} \quad \text{Equation 1.1}$$

Charge carriers travel a much longer random path during the duration of their drift across the crystal due to thermal motion, during which an electron or hole may interact with an impurity or crystallographic defect, trapping it. Charge trapping can thus be modeled as an exponential decay in time, t , of the population of charge carriers, q , dependent on their probabilistic lifetime in the material before being trapped, τ , [7]:

$$q(t) = q_0 e^{-\frac{t}{\tau}} = q_0 e^{-\frac{\Delta x}{\mu \tau E}} \quad \text{Equation 1.2}$$

The Shockley-Ramo theorem can be used to explain the signals induced by these electrons and holes on pixelated and planar electrodes [8],

$$\Delta Q(t) = -q \Delta \phi_w(x(t)) \quad \text{Equation 1.3}$$

where ΔQ is the charge induced on the preamplifier input, q is the moving charge, $\phi_w(x)$ is the electrode's weighting potential at the charge's position, x , and $\Delta \phi_w(x)$ is the

difference between the weighting potential at the charge's initial and final positions. Theoretical weighting potentials for electrodes typical of the detectors herein (specifically those of the electrodes used in Chapter 5) are shown in Figure 1.1.

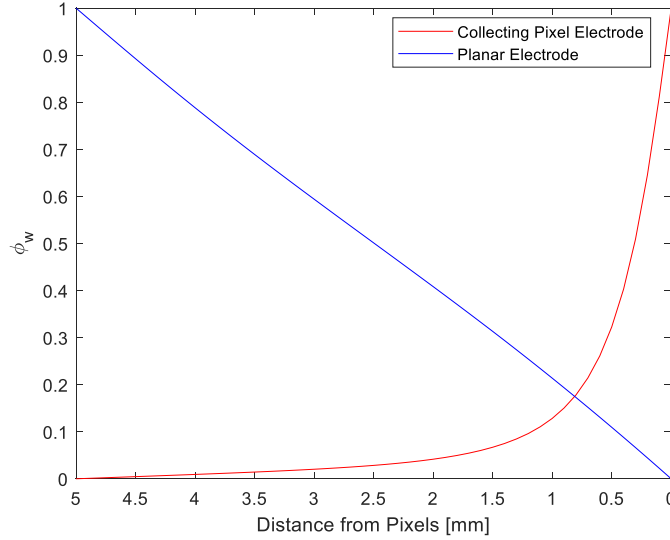


Figure 1.1. Theoretical weighting potentials of the collecting pixel electrode (red) and the plane electrode (blue) for a 5-mm-thick detector with 1-mm pixel pitch.

Electrons and holes freed by a gamma-ray interaction drift through the pixel and planar weighting potentials, inducing charge on the inputs of charge-sensitive preamplifiers, the outputs of which are recorded as pulse waveforms. The pulse waveforms measured from the preamplifier output can thus be studied to reveal the position and quantity of the freed charges during their drift between the gamma-ray interaction location and either their collection at the electrode(s) or their trapped locations.

1.2 Position Reconstruction

The maximum amplitude of the pulse waveform usually occurs at the time the charge is collected by the electrode and can of course also be predicted using the Shockley-Ramo theorem. The pixel signal amplitude is mostly invariant to the depth of the gamma-ray interaction, while the plane signal amplitude is linearly dependent on depth for unipolar-sensitive detectors, so the ratio of these two amplitudes (the cathode-anode ratio, CAR) has historically been used as a depth analog [9] for events in which only one gamma-ray interaction occurred. An event is an occurrence of one or multiple gamma-

ray interactions which cause a triggered readout of the electronic hardware. This work studied only single-pixel events with few exceptions.

If the time of the interaction and the time of charge collection can be precisely recorded, then the charge drift duration can also be used as a depth analog. These depth analogs can be used to calibrate the response of a pixelated semiconductor detector since the detector's primary gain variations should be from 1) the freed charge's initial weighting potential, which is directly dependent on depth (Equation 1.3), and 2) from the distribution of the fraction of the freed charge which was trapped throughout the duration of its drift, which is dependent on depth via the charge's velocity and the depth distribution of traps (Equation 1.2).

The use of pixelated electrodes was historically chosen to reduce the signal from heavily-trapped holes in semiconductor-based gamma-ray spectrometers [10], but significant hole motion has been shown to affect depth reconstructions when calibrating with CAR by altering planar-cathode signals. This was previously addressed by fitting and removing the hole-induced component of the signal from the planar-cathode waveform [11], but the effect on pixel signals was not discussed. An understanding of the effects of ambipolar sensitivity on 3D reconstruction techniques is more important as new materials with high electron and hole mobility-lifetime products are developed. Effects of ambipolar signal are studied in Chapter 5, including the development of a new depth parameter.

The general relations between waveform shape and depth have also been leveraged directly in system response fitting [12] and indirectly in principal component analysis [13] for CZT detectors. These techniques should extend well to ambipolar-sensitive detectors but were not used in this work.

1.3 Incomplete Charge Collection

Methods have been developed to address phenomena called incomplete charge collection in pixelated CZT, but are restricted by the assumption that hole motion is negligible [14]–[16].

Incomplete charge collection (ICC) occurs when the freed charge which induces signal on a triggered pixel electrode is less than the freed charge which induces signal on the planar electrode. This is caused by one of three cases:

- 1) Significant charge trapping occurs before the charge cloud nears the collecting pixel. Drifting charge which is quickly trapped induces a charge on the planar electrode proportional to its drift distance but induces a negligible charge on the pixel electrode unless it is close to the pixel electrode. This is due to the linear weighting potential of the planar electrode and the nonlinear weighting potential of the pixel electrode shown in Figure 1.1.
- 2) The charge cloud leaks to a neighboring electrode because of its initial size, because of diffusion, or because of a lateral electric field, but does not cause a secondary trigger. Charge which is collected by a neighboring pixel or the guard ring surrounding the pixels does not contribute to the final amplitude of the collecting pixel signal. Techniques such as forced readout of the neighboring pixels mitigate this problem but are not always employed. Trigger thresholds are often set higher ($\sim 50+$ keV) for alternative materials because of their higher amplitude noise, exacerbating the problem of charge leakage. Some leaked charge may also drift into a weak-field region in the gap between pixels, causing significant charge trapping.
- 3) A recorded event includes multiple photon-electron interactions but is misclassified as a single-interaction event. Single-pixel events are assumed to be either a single photoelectric absorption or a single Compton scatter, but additional interactions can occur without causing a secondary trigger if they occur under the unmonitored guard ring, under the already triggered pixel, or even under another pixel if the secondary interaction produces a signal with an amplitude below the trigger threshold. Additional interactions may be with a scattered primary photon or with a secondary bremsstrahlung photon or characteristic x ray generated by the primary photoelectron. As in the second case, any charge not collected by the triggered pixel will be lost from the recorded event. ¹

The first case, charge trapping, will be found more often in crystals of poor quality with extended trapping sites. The second and third cases, both of which are classified as charge sharing, will be found more often in materials with greater diffusion, harder

¹ The case in which a secondary interaction occurs under the triggered pixel is not ICC but another anomaly which is identified by the techniques presented in this work.

characteristic x rays and bremsstrahlung, and in crystals in which the guard ring is a larger fraction of the total active area (generally smaller crystals).

Methods to identify ICC are presented in Chapter 6 and Section 4.2.5.

1.4 Material Selection

Alternatives to CZT are investigated because they may perform better than CZT or because the same techniques may be applied to cheaper materials to easily fill a different market role than CZT. CdZnTeSe is expected to have higher yield than CZT but should otherwise perform similarly except for an increased hole mobility, which can be marketed towards high-flux applications.

There has been interest in TlBr for decades because of its high atomic number, high density, simple crystal structure, low melting point, and wide bandgap. TlBr is therefore expected to have greater stopping power and a higher photofraction, be cheaper to produce, and be able to operate at higher temperatures than CZT.

Halide perovskites, including CsPbBr₃, have recently seen interest because of their rapid development in photovoltaics and boast long carrier lifetimes but low mobility. Over the course of this work, tremendous leaps forward in the performance of perovskite detectors were achieved, greatly increasing interest in the material.

1.5 Ion Migration

1.5.1 *Thallium Bromide*

The best energy resolution recorded of TlBr at 662 keV remains 0.72% FWHM at 662 keV which was the best-pixel under cooled operation observed by Thrall in 2013 [17]. Stability at room temperature has been greatly improved since 2013 as growth and manufacturing processes have evolved [18], so it is unfair to compare recent room-temperature operation to previous cooled operation.

The changes observed in the performance of TlBr when operated as a gamma-ray spectrometer can generally be characterized into one of two categories: failure, often called “polarization,” and conditioning.

Failure is characterized by a decrease in measured photopeak energy, by a degradation of resolution [19]–[22], and sometimes by a decrease in leakage current and average drift velocity [20], [23], [24]. A mechanistic explanation including the most

recent work on the matter is that edge dislocations migrate under an electric field, ejecting charged ionic vacancies [25], [26] which migrate toward the anode, sometimes creating a strong field (hence the name “polarization,” though the strong field is not necessary for the process) [22]–[25], allowing anode metal to diffuse into the bulk (most easily along grain boundaries), creating electron traps over the first days to months of operation which inhibit signal induction by information carriers [22], [24].

Conditioning is characterized by an increase in photopeak centroid [17] due to a homogenizing of the electric field which relaxes during inoperation. The rate of conditioning has been observed to be dependent on applied bias. Trap centers which hold space charge appear to be migrating out of or disappearing from the bulk during conditioning. The studies of conditioning which led to these conclusions were performed at -20 °C to delay device failure. At this temperature, conditioning occurred over the first one to five days of operation [2].

An effect previously labeled conditioning at room temperature was found to be more like the failure mechanism and is presented in Section 4.2.1. General performance of TlBr tested during this work is reported in Section 7.1.

1.5.2 Halide Perovskites

While some halide perovskites have seen success as radiation detectors [27], they are still materials in early development plagued with issues such as temporal instability, and low reproducibility. Low-bias current instability in MAPbBr₃ has been mitigated by reducing the operating temperature and by well-timed bias cycling. Irreversible high-bias hysteresis has been thought to cause electric field instability as Br⁻ ions collect at and react with the anode [28], like the previously proposed failure mechanism in TlBr. Similar instabilities were observed in CsPbBr₃ during this work and are briefly reported in Section 7.3.

1.6 Auger Recombination

Auger recombination occurs when a trapped electron is freed by the trapping of an adjacent hole. A positive skew (high-energy tail) in TlBr photopeaks was previously observed and explained by Auger recombination following the example of HgI₂ [29]. The necessary filling of traps by electrons was believed to be a gradual process dependent on bias time since the skew was observed to appear gradually during days of operation and

its growth could be reset using sub-bandgap LED illumination [2]. The Auger trap sites were believed to exist uniformly throughout the bulk since the magnitude of the extra charge which caused the skew was correlated with hole drift distance [30].

Localized Auger recombination was observed and is described in Section 4.2.4.

1.7 Challenges of Time-dependence

Identification of the causes of anomalies in the responses of alternative room-temperature semiconductors (ARTS) is vital because the exploratory nature of the research continually leads to unexpected observations. Detectors made from exploratory materials are often fabricated one-off by manufacturers which does not give time for manufacturing errors to be corrected and which reduces repeatability compared to methods of mass production. Manufacturing errors might include excess or loose wiring which cause electromagnetic interference, microphonics, electrical arcing, or improper surface passivation which allows chemical reactions at the crystal surface that ultimately change detector performance. Imperfections in material growth like the presence of grain boundaries or regions of high defect concentration within the crystal bulk might be solved by accepting a low yield from mass production but must be circumvented and ideally explained during small-scale or one-off production.

The biggest obstacle to investigation into the cause of many anomalies is the transience of the anomalies. For example, bulk and surface properties have been observed to change in TlBr over days to weeks even at -20°C [2], [17], [24]. Changes in performance on the scale of hours or less preclude investigation by experiment (repeating measurements with controlled independent variables) thus may be better understood through observational study because a single measurement may take several hours to accumulate sufficient statistics to characterize the change. Furthermore, detector performance may be affected by multiple multivariate hysteretic mechanisms operating on different timescales. For example, if resistivity is strongly dependent on the concentrations of ion species in the bulk and there are multiple species with different mobilities and diffusion coefficients within crystallographic defects, the detector's energy resolution may change during biased operation as the ions drift in a way that is dependent on the initial spatial distribution of all ion species, which is neither controllable nor practically measurable nor revertible (due to entropy). Hysteresis is clearly present in this

work, and multistage anisotropic interplays between different defect types are believed to occur in materials used in this work [26], [31], so such unpredictability is possible.

Experiments consisting of consecutive measurements having even a single independent variable are untrustworthy unless the results of consecutive measurements with constant independent variables are predictable, therefore it is important to begin the study of a detector by studying the evolution of its response under fixed conditions. Some mechanisms may relax during unbiased storage, such as TlBr conditioning [2], while others take place during unbiased storage, such as TlBr surface degradation [32], so continuity between inconsecutive measurements should not necessarily be assumed. If detector performance changes unpredictably, conclusions about the changes should be drawn from a detailed time-dependent analysis of a dataset taken under fixed conditions. For example, choosing events with long drift times or high plane-pixel ratios may be more reliable than a follow-up collimated irradiation to investigate depth-dependent effects because the detector behavior could change before the consecutive collimated experiment could be conducted.

For this reason, most anomalies were investigated in this work by post processing digitized waveforms recorded under conditions held as constant as possible, not by intentionally changing independent variables. A report of all important anomalies observed is given in Chapter 4.

Chapter 2 Equipment and Procedures

Semiconductor crystals manufactured for use as radiation detectors were received from companies and labs outside of the University of Michigan and tested using equipment designed in-house at the University of Michigan in the Orion Research Group. Electrical responses to gamma radiation were digitized and saved for analysis.

2.1 Crystals

Throughout this work, crystals are called by their alphanumeric code identifiable to the Orion Group at the University of Michigan so that any data mentioned herein can be easily revisited.

Two $\text{Cd}_{0.90}\text{Zn}_{0.10}\text{Te}_{0.98}\text{Se}_{0.02}$ (CZTS) crystals with 2×2 -pixel anodes, anode grids, and planar cathodes were received by the University of Michigan from Utpal Roy of Brookhaven National Laboratory (BNL). The first CZTS crystal, BNL1-S2, was $10.5\times 10.0\times 9.9\text{ mm}^3$ and was not wire-bonded or flip-chip-bonded to any carrier board, shown in Figure 2.1. A new bondless connector described in Section 2.2.3 was designed and used to avoid a potential destructive misapplication of permanent conductive epoxy.



Figure 2.1. Photo of BNL1-S2 showing unbonded face as received.

The second CZTS crystal, BNL2-S2, was $11.0\times 10.8\times 19.3\text{ mm}^3$ and had a Frisch collar near the planar cathode visible in Figure 2.2. The grid and guard ring were

electrically floating. The crystal was adhered and wire-bonded by BNL to a carrier board with GaGe-system-compatible signal pins designed by the University of Michigan.

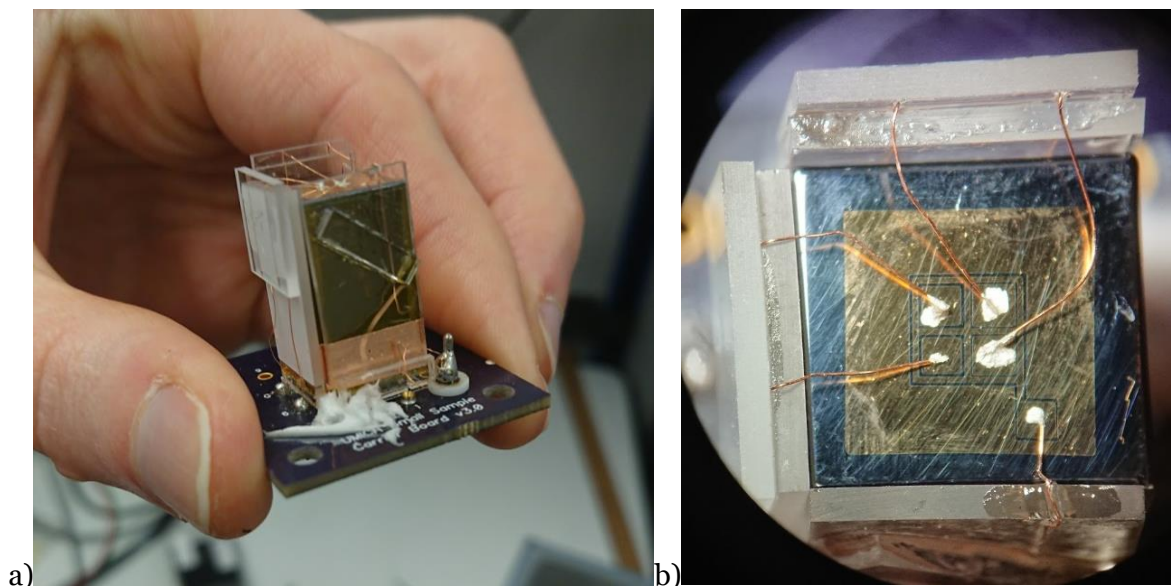


Figure 2.2. Photos of BNL2-S2 showing cathode guard ring and wire bonding.

Two CsPbBr_3 perovskite crystals were received. A 1-mm-thick crystal with planar electrodes was received from Yihui He and Mercouri Kanatzidis of Northwestern University, shown in Figure 2.3a, and a crystal with dimensions $8.12 \times 6.72 \times 3.27 \text{ mm}^3$ having 2×2 1-mm² pixelated cathodes, a guard ring, and a 16-mm² planar anode was received from Teddy Feng and Jinsong Huang of the University of North Carolina, shown in Figure 2.3b. The top of the orange crystal in Figure 2.3b is obscured by wiring and lacquer.

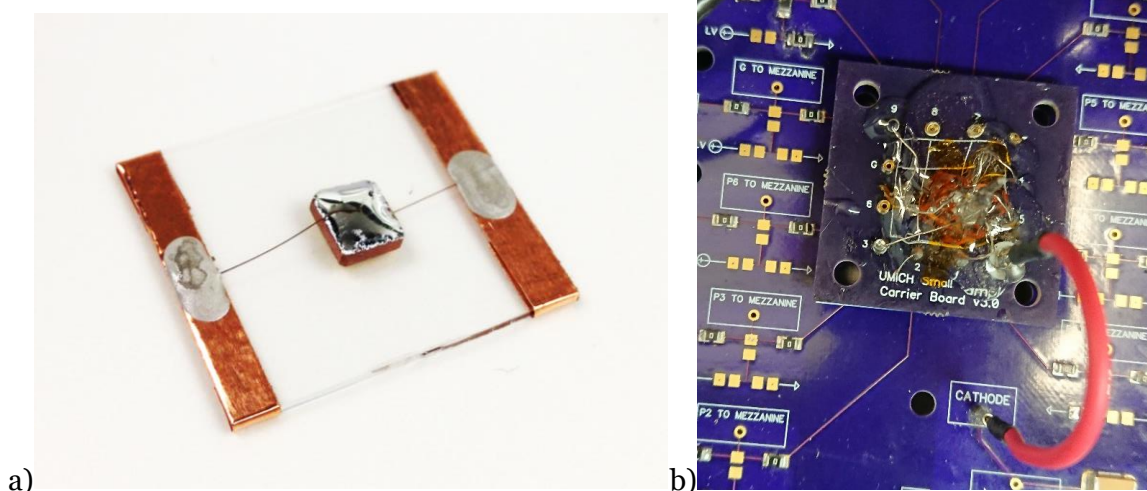


Figure 2.3. Photo of a) planar perovskite crystal manufactured by Yihui He and b) pixelated perovskite crystal manufactured by Teddy Feng installed in readout system.

Many TlBr crystals with 3×3 -pixel anodes and planar cathodes and several crystals with 11×11 -pixel anodes and planar cathodes were received by the University of Michigan from Radiation Monitoring Devices, Inc. in Watertown, Massachusetts. Work using these crystals comprises most of the work in alternative room-temperature semiconductor detectors within the Orion Group at the University of Michigan and most of the work herein. RMD's manufacturing methods are described below [18].

The crystals were grown using commercially available 5N-purity TlBr powder purified through 50-200 passes of zone refining in a horizontal furnace. The ingots grown were cut into wafers using a wire saw and then were lapped, polished, and chemically etched with either Br-MeOH or HCl. Au/Cr, Pd, or Pt electrodes were deposited using e-beam evaporation. Some 11×11 -pixel and 3×3 -pixel crystals were manufactured with 1-mm-pitch pixels and some were manufactured with 1.72-mm-pitch pixels. Most crystals were manufactured with 1-mm-pitch pixels. A $5\times 5\times 5$ mm³ crystal with 3×3 1-mm-pitch pixels and a $22\times 22\times 5$ mm³ crystal with 11×11 1.72-mm-pitch pixels are shown at this stage in Figure 2.4.

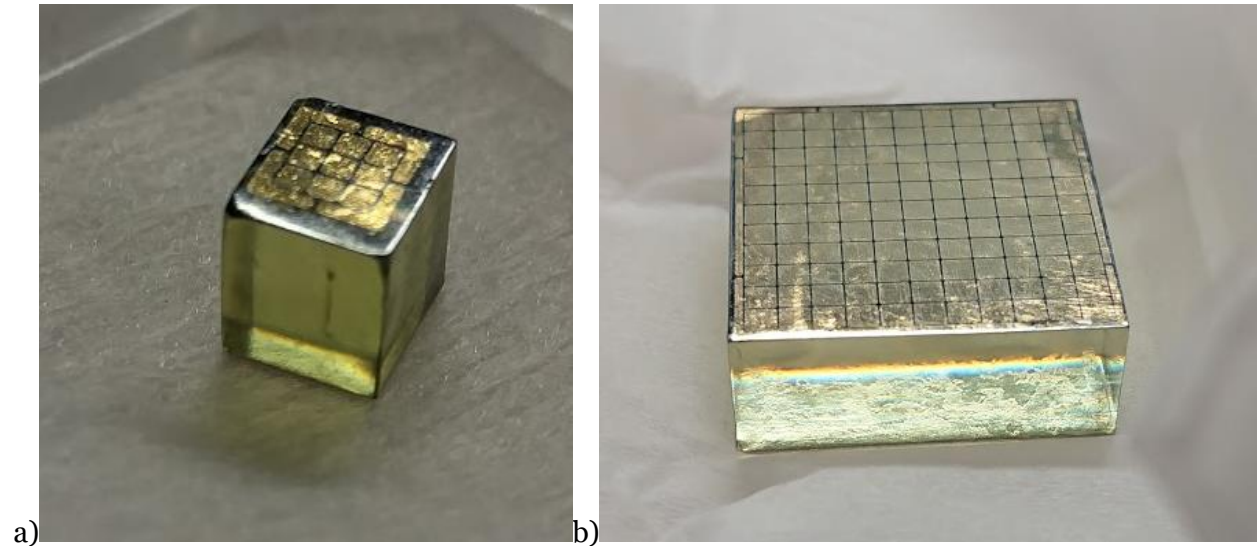


Figure 2.4. Photos of a) small and b) large TlBr crystals manufactured by RMD after electrode deposition.

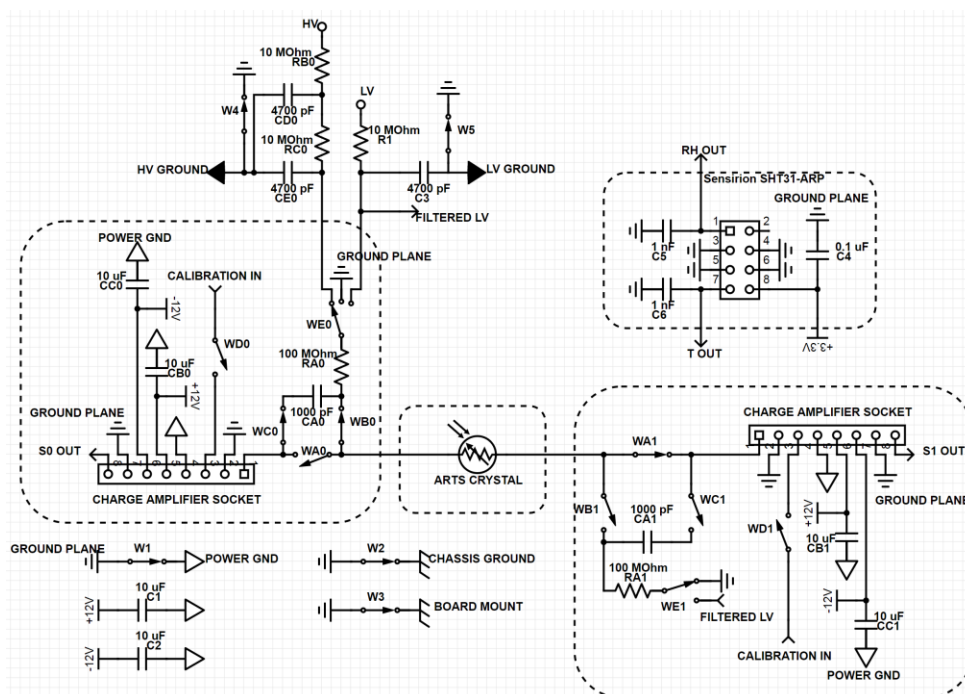
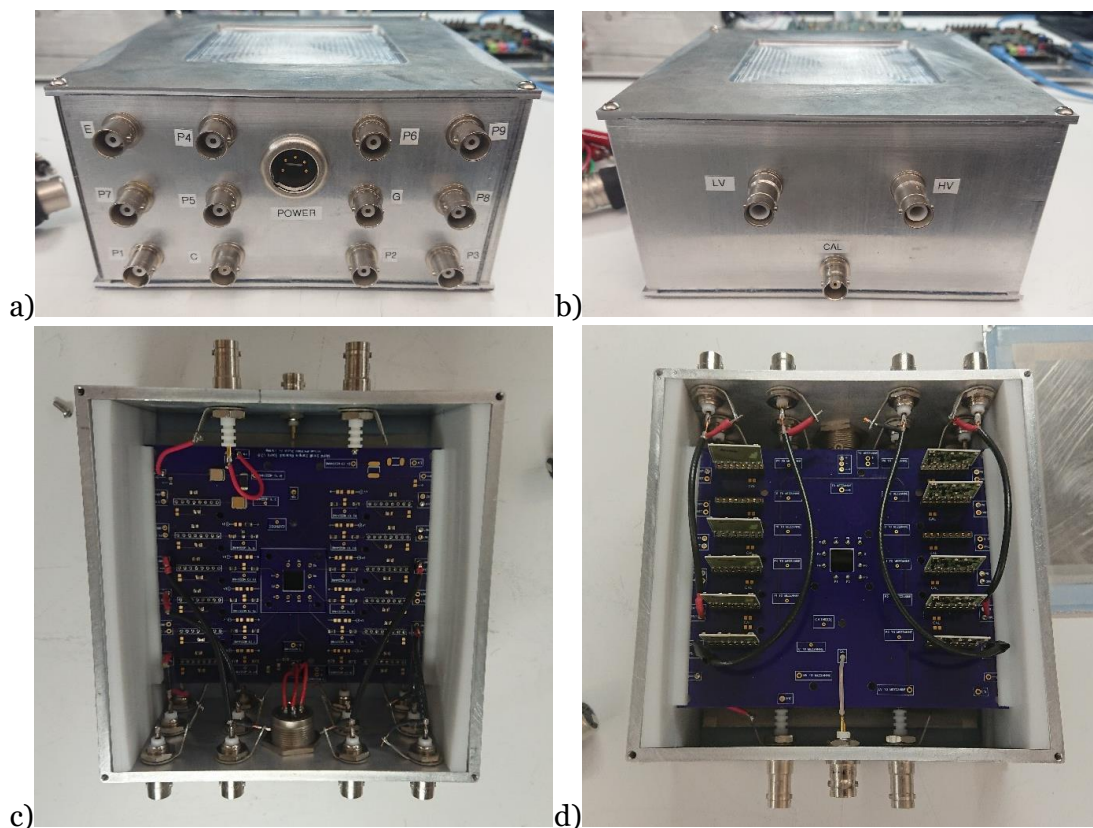
The 3×3 -pixel crystals were mounted to carrier boards and wire bonded to pins on the carrier boards compatible with the Orion GaGe-based readout system. The 11×11 -pixel crystals were flip-chip bonded to a carrier board with pins compatible with the Orion application-specific integrated circuit (ASIC) -based readout systems.

Some crystals were refabricated by RMD after testing to remove a damaged layer of the crystal. Refabrication entailed removing wire bonds, removing the pixelated electrode and a thin layer of TlBr, and then lapping, polishing, etching, depositing contacts, and wire bonding again.

2.2 Electrode Readout

2.2.1 GaGe-based

The electrodes of 3×3 -pixel crystals were electrically coupled to eV-5093 preamplifiers and the planar cathode was also coupled to Keithley or iSeg high voltage (HV) power supplies through a backplane and aluminum enclosure, shown in Figure 2.5. This backplane and enclosure were developed for the work herein based on previous systems designed and assembled by the Orion Group at the University of Michigan. Board layout was performed with DipTrace and boards were printed by OSH Park. The aluminum enclosure and plastic board supports were machined at the LSA Scientific Instrument Shop at the University of Michigan. Connections to preamplifier power supplies and connections between preamplifier signal output pins and GaGe digitizers were facilitated through the backplane and enclosure. A schematic representing the backplane circuit is shown in Figure 2.6. The Sensirion thermometer was not installed. Crystals were mounted and wire bonded by manufacturers to carrier boards like those shown in Figure 2.7 which mate with the readout system.



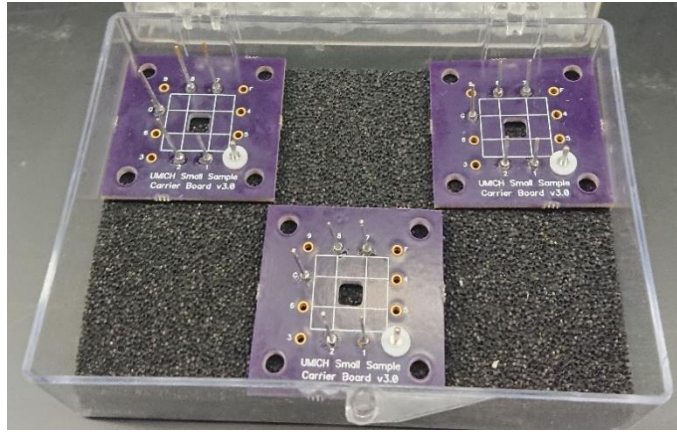


Figure 2.7. Crystal-carrier boards compatible with the GaGe-based readout system.

The primary differences between this readout system and previous GaGe-based readout systems were 1) the enabling of capacitive coupling between pixel electrodes and preamplifier inputs which is required for perovskite crystals with unstable high leakage currents, 2) the repositioning of bulkhead connectors to reduce space requirements outside the enclosure for use in the environmental chamber, and 3) the repositioning of the crystal to the middle of the board to reduce trace length. The last difference did not seem to reduce noise and inhibited side irradiation, so it was reversed in a future iteration. Crystal carrier boards were updated to include tall posts to help manufacturers wire bond.

Another iteration of the GaGe-based readout system was designed which allows the crystal carrier board to mate with an ASIC-based readout system in multiple rotationally symmetric configurations. This system, the boards of which are shown in Figure 2.8 and Figure 2.9, was not assembled but may be useful in future ARTS collaborations. This new iteration allows installation of the temperature sensor indicated in Figure 2.6.

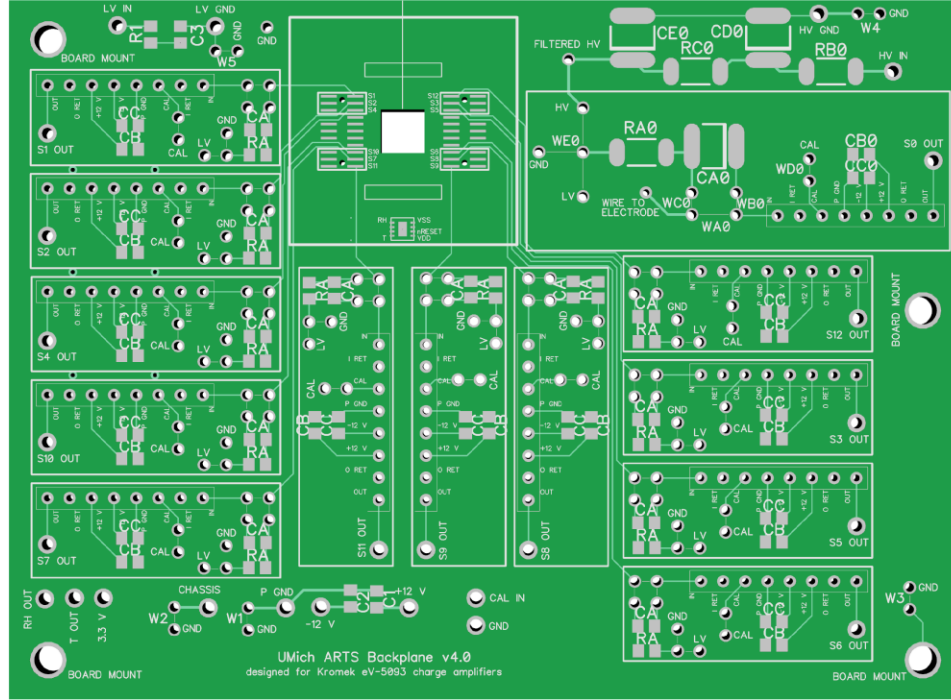


Figure 2.8. Rendering of updated unassembled backplane of GaGe-based readout system.

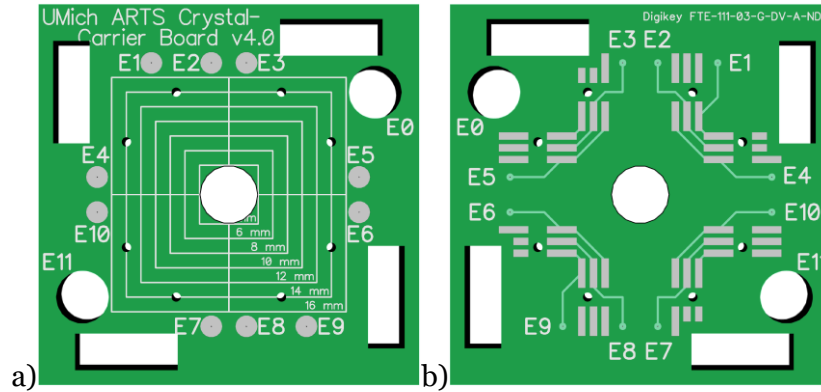


Figure 2.9. a) Front and b) back rendering of updated crystal-carrier board for GaGe-based readout system which allows rotationally symmetric mating with ASIC-based readout systems.

Preamplifier outputs were connected to GaGe Compuscope 14-bit Octopus digitizers having eight or four channels connected via PCI/PCIe to desktop computers. Two digitizer units were used synchronously on each desktop computer to read out all nine pixels and one plane electrode signal, as necessary. The digitizers were operated and waveforms were recorded using a Windows application previously written in-house with the Compuscope SDK in C++. Readout was triggered when any pixel signal crossed a threshold which was set according to the noise of each measurement. Waveforms were

usually sampled at 5 or 10 MHz for 512 samples, which allowed observation of electron collection and ample baseline sampling.

2.2.2 ASIC-based

The electrodes of 11×11-pixel crystals were read out using the Orion Solo system and the UM_VADv2.2 system built in-house around application-specific integrated circuits (ASICs) produced by Integrated Detector Electronics AS – IDEAS in Oslo, Norway. These systems include onboard preamplifiers coupled to each electrode, digitizers, and a Peltier cooling device, and interface with a desktop computer using a Windows application previously written in-house. On-board high-voltage (HV) and ASIC power supplies were available but external power supplies were used instead to ensure consistent low-noise operation. Readout was triggered when any fast-shaped pixel signal crossed a threshold which was set according to the noise of each measurement. Waveforms were sampled at 5 MHz for 160 samples. Preamplifier feedback settings were adjusted according to the leakage current of each measurement.

2.2.3 Bondless Connectors

Attempts were made to isolate electrode manufacturing errors and bonding errors from material performance by developing hardware capable of bondless readout. Four components were tested as potential bondless connectors: an anisotropically conductive tape 3M-9703, a silicone sheet embedded with vertical conductors Fujipoly-WBCo35, individual elastomeric pins RDIS-invisipin-5502-14-0035, and a bondless interposer board used by Redlen technologies which is not commercially available.

The 3M tape required a conductive area larger than 1 mm² provided by small 1-mm-pitch crystals. The Fujipoly connector successfully made vertical electrical connections while insulating lateral connections but abraded the electrodes of a small TlBr crystal. The invisipins successfully made vertical electrical connections and were used to evaluate BNL1-S2, shown in Figure 2.10. Two boards were laid out in DipTrace and printed by OSHPark to act as a sandwich around BNL1-S2, allowing electrical connections of the invisipins via compression, also shown in Figure 2.10.

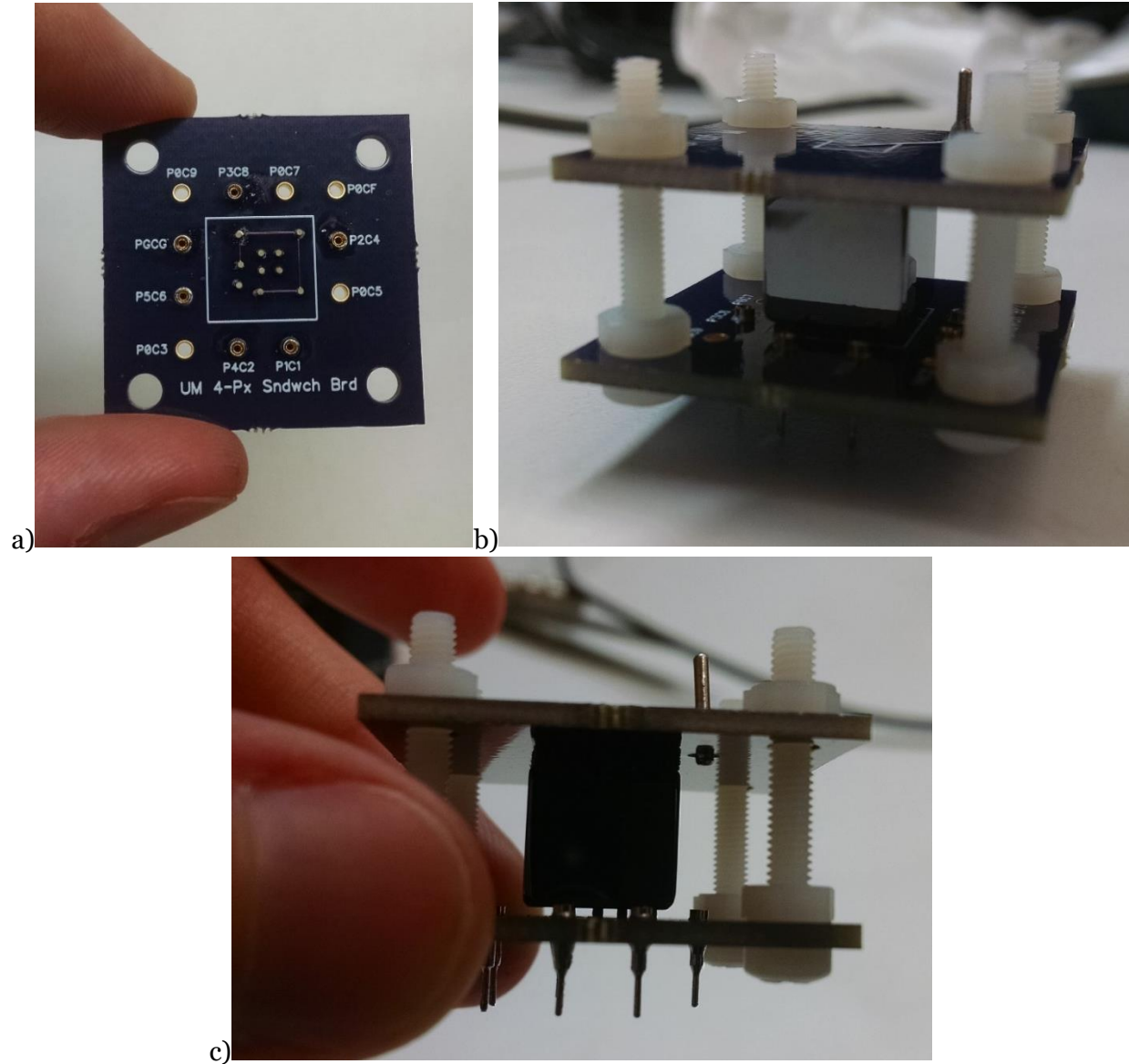


Figure 2.10. Photos of a) a board with Invisipins mounted and b-c) the sandwich assembly with BNL1-S2 installed.

A frame and HV-coupling circuit compatible with Redlen's bondless interposer board and the VAD_UMv2.2 system were designed using Autodesk Fusion 360 and DipTrace and printed using the Duderstadt Center's Fabrication Studio and OSHPark, respectively. The frame was capable of translating, yawing, and compressing a crystal relative to the interposer board, and is shown in Figure 2.11. An unbonded 11×11 -pixel TlBr crystal, 157A52, was tested in this frame using Redlen's bondless interposer board and the VAD_UMv2.2 system, and radiation-induced pixel signals were recorded, but a

photopeak could not be observed and more unbonded crystals were not received, so this hardware was not used further.

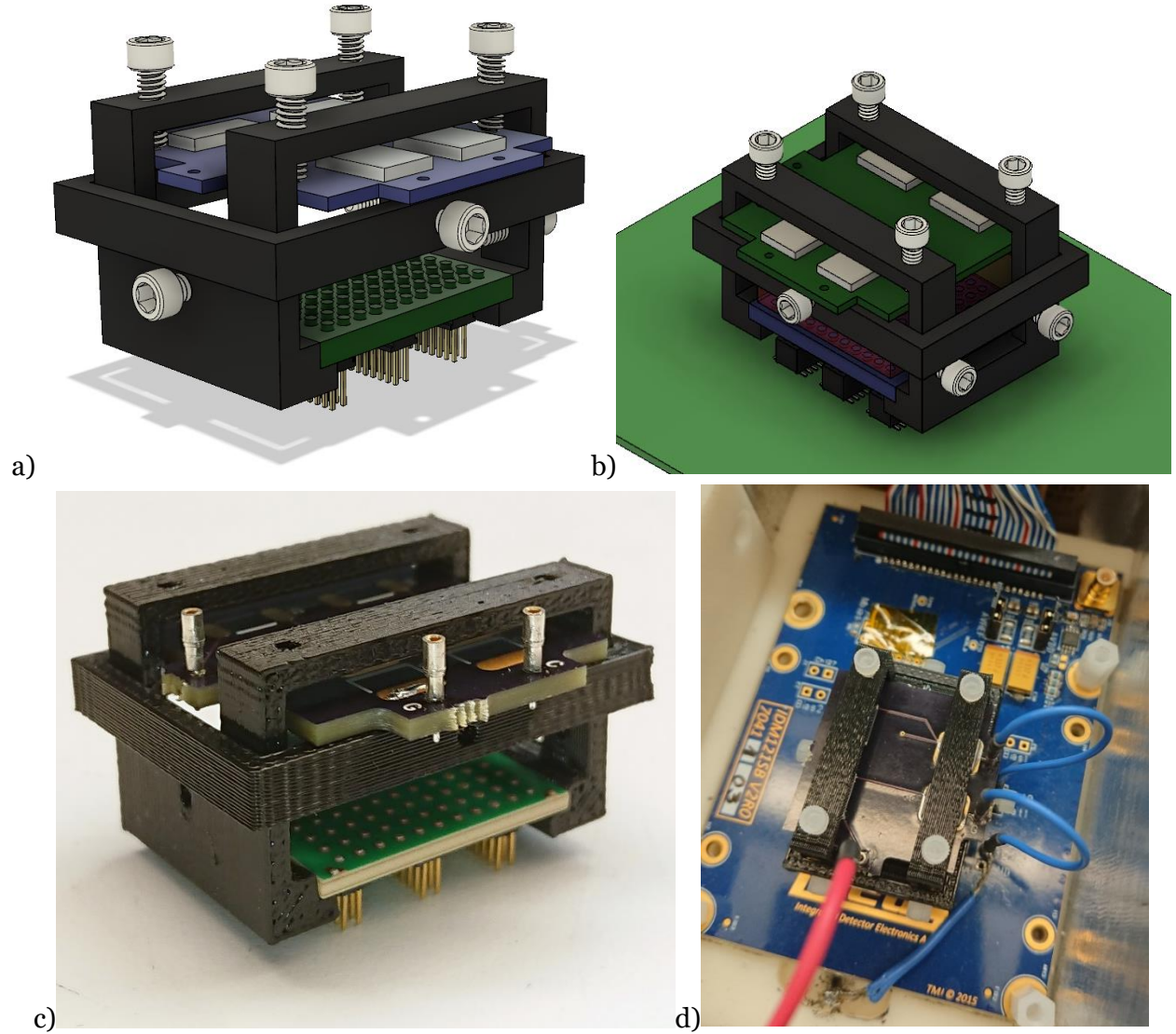


Figure 2.11. a,b) Renders and b,c) photographs of a,c) a bondless frame without crystal and b,d) bondless frame with crystal installed, connected to an ASIC system.

2.3 Procedures

A negative bias was applied to the planar electrode for TlBr and CZTS crystals and a positive bias was applied for perovskite crystals after a crystal was installed in one of the systems mentioned above (called “operating”). Pixels were held at ground by preamplifier inputs and guard rings were usually connected directly to a ground plane. The bias was increased in steps of 100 to 500 volts every 12 or 24 hours with a ramp speed between 0.25 and 4 volts per second between steps. Leakage current through the planar electrode

was generally monitored and the bias was reduced to zero if the leakage current increased during a dwell period by an order of magnitude.

This slow bias stepping was adopted from collaborators at Lawrence Livermore National Laboratory who observed increased stability of the leakage current through TlBr crystals operated initially using slow bias stepping. The bias was rapidly applied in a few cases, such as the second operation of 175CS5-4, which revealed slow changes in detector response that were not visible during its first operation which included slow bias stepping, as with the operation of 935-38AS3, the best performing 11x11-pixel detector at room temperature presented in Section 7.1.1. Bias stepping was not implemented during low-bias testing of perovskite crystals.

Electric fields of 2 kV/cm are usually used in CZT and have been applied to TlBr, and fields approaching 4 kV/cm have also been used to produce promising results in TlBr [21]. A range of bias voltages were applied in this work. An electric field of 1 kV/cm was applied to CZTS and perovskite crystals and a voltage of -1000 V was applied to TlBr crystals unless otherwise stated. The practice of limiting the bias voltage to -1000 V for TlBr crystals was adopted from collaborators at Lawrence Livermore National Laboratory who observed equivalent or worse performance when applying biases higher than -1000 V to a roughly 1-cm-thick crystal. Additionally, extended application of a high bias was suspected to cause permanent failure of TlBr detectors. The bias was not limited for all detectors, such as for the bias-dependent results given in Section 7.1.3, including operation of 935-38AS3 at -1250 V, the best performing 11x11-pixel detector at room temperature.

The leakage currents through each pixel were measured in a few cases by measuring the offset of each pixel's preamplifier output voltage when those pixels were directly coupled to the preamplifier input (not capacitively coupled) before and after applying a bias. Constant current being drained by the preamplifier will flow through the feedback resistor and generate a voltage drop across the feedback resistor which is measurable in the preamplifier output voltage. The preamplifier feedback resistors were assumed to have a resistance of $9.7 \times 10^8 \Omega$, following Koehler's method with the same equipment [24].

A Cs-137 button source of gamma rays was usually placed on top of the aluminum detector housing during the 12- or 24-hour dwell periods between steps and the detector's

radiation response was recorded (called a “measurement”). This source position is on the planar-electrode side for ASIC-based systems and on the pixel-electrode side for GaGe-based systems. A Co-57 source was used to irradiate thin planar perovskite crystals because of its lower-energy gamma rays’ lower mean free path.

In some cases, a Cs-137 source was collimated to verify depth-dependent performance. A tungsten collimator made of two 4-cm-thick slabs of tungsten separated by 1 mm was placed between the source and the side of the aluminum detector enclosure, limiting the depths irradiated but irradiating all pixels.

Detectors were operated at room temperature (roughly 20° C) unless otherwise stated. Peltier coolers operated continuously in the Orion Solo system to remove heat from the ASICs. Temperature was not usually controlled within the VAD_UMv2.2 system nor in the GaGe-based readout systems. Temperature control around the GaGe-based readout box was achieved in a few cases with a Thermotron S-1.2-3200 environmental chamber. The environmental chamber stabilized the temperature read by a thermometer located inside the environmental chamber but outside the readout box. Vibrations caused by the mechanical cooling system within the environmental chamber introduced excess microphonic noise which made the environmental chamber undesirable when testing crystals which could operate at room temperature.

Waveforms from the pixel and plane were recorded for each single-pixel trigger during a measurement. Waveforms from neighboring pixels were also recorded in a few cases so that sub-pixel position could be calculated using the opposing neighbor ratio [33]. Events which triggered multiple pixels (multi-pixel events) were generally not analyzed during this work. Including multi-pixel events in a final energy spectrum will increase efficiency but the resolution from single-pixel events is better and anomalies are easier to localize by studying only single-pixel events.

Chapter 3 Software and Processing

Digitized waveforms which were recorded during each measurement were digitally processed to reconstruct the 3D position and energy deposited in each single-pixel event. Calibrations were then performed to homogenize the response of the detector under test for all interaction positions within the crystal, improving each pixel's energy resolution.

Lateral (x and y) positions were reconstructed coarsely using the location of the pixel electrode which collected the freed charge. Subpixel positions were rarely calculated using the relative ratios of the neighbor signal amplitudes according to the technique of opposing neighbor ratios (ONR) [33]. Depth (z) was reconstructed using the ratio of the amplitude of the signal from the planar electrode to the amplitude of the signal from the pixel electrode which collected the freed charge. Depth was also reconstructed using the difference between the time that signal was first induced on the planar electrode by the motion of the freed charge and the time that the freed charge was collected by the pixel electrode. A justification for calibration according to these depth parameters is given in Section 1.2. Another depth-dependent parameter, the ratio between the prompt amplitude of the pixel signal and the final amplitude of the pixel signal, was used in a few cases to apply an additional calibration, a detailed explanation of which can be found in Chapter 5.

Calibrations were performed by generating an energy spectrum of detected Cs-137 gamma rays for each voxel (discrete x, y, z location) within the crystal and normalizing the amplitude of all events which occurred in a voxel by the Cs-137 photopeak centroid of that voxel. This is called "self-calibrating" when the photopeak centroid is found from the same data to which the calibration is being applied. All results herein are self-calibrated. Material stability must be guaranteed before a past calibration can be reliably applied to live data.

In the Orion Measurements Group at the University of Michigan, position and energy reconstructions have historically been calculated using the Polaris Waveform Analyzer and Polaris Interaction Analyzer codes. Reconstructions were calculated using

the Polaris codes for some of this work for verification, but a new code was written in MATLAB (MathWorks) and was used to calculate reconstructions and perform calibrations for nearly all the work herein.

Anomalies in raw data (i.e., waveforms), anomalies in the distributions of reconstructed values (e.g., depth histogram), and anomalies in calibration curves (e.g., relation between calculated photopeak position and depth reconstruction for a pixel) complicate the linear workflow of event reconstruction and calibration because an error in one step of processing may not be found until a later step. These anomalies may be caused by a deficiency in the hardware, software, procedures, or the detector under test. Details of anomalies encountered during this work are given in Chapter 4.

The new code was developed because the author found the debugging environment in MATLAB more familiar and flexible than the debugging environment in Microsoft Visual Studios, and the new code came to be the exclusive reconstruction and calibration tool used in this work because it lent itself to rapid algorithm prototyping, complex visualizations, and nonlinear workflows.

Four important capabilities were developed: waveform processing according to arbitrary instructions, arbitrarily dimensioned multivariate histograms, visualization of arbitrarily selected events, and operations on data using arbitrary histogram fits. A description of the important functions, datatypes, visualizations, and the workflow used in the code is given below followed by a processing example to illustrate these capabilities.

3.1 Important Functions and Data types

3.1.1 Accessing Waveform Files

The data acquisition system (DAQ) wrote write time, triggered-channel number, and digitized waveforms to a binary file (a “DAQ file”) for each recorded event during the initial radiation measurements described in Chapter 2.

In one function which accesses DAQ files, the new processing code saved one value from each event of the selected DAQ files into a vector by performing the operations specified in a given instruction set. Examples of instruction sets include “save the triggered-channel number” and “save the maximum of the shaped triggered pixel waveform.” The vector of values was stored with metadata, e.g., a list of processed files and instructions, in a MATLAB struct datatype. This process was called “distilling,” and

the struct created is herein called an “essence.” All event reconstructions were calculated from essences.

Through another function, the code read any number of selected events from the DAQ files, manipulated the waveforms according to given instructions, and binned the amplitude of each sample of each waveform into a bivariate histogram (amplitude versus sample number) to produce a distribution of waveform shapes, visualized in Figure 3.1. The histogram was stored with metadata in a MATLAB struct. This process was useful in, e.g., investigating near-plane Auger recombination discussed in Section 4.2.4. (Plotting without binning was also possible, e.g., Figure 3.3.)

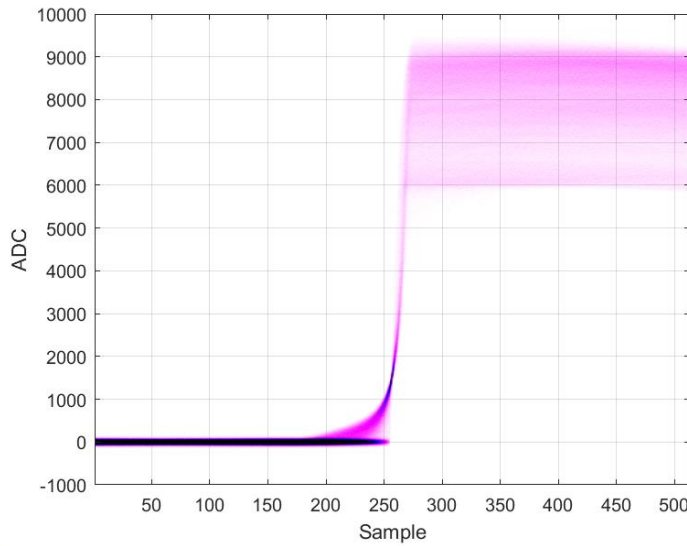


Figure 3.1. Distribution of waveform shapes created by superposing pixel waveforms with reconstructed amplitude greater than 6000 ADC.

3.1.2 Operating on Essences

Essences like the plane-pixel ratio were created using operations after distillation. Element-wise arithmetic was performed using multiple essences, such as dividing each event’s plane amplitude by each event’s pixel amplitude. This process is herein called “mixing essences.”

Essences were binned into histograms using another function. E.g., triggered-pixel amplitudes were binned into a univariate histogram (forming an energy spectrum). Furthermore, any number of essences could be binned together, with each successive essence defining a higher dimension of binning. E.g., an energy spectrum was created for each triggered channel number, creating a bivariate histogram, and that was repeated for

each depth bin creating a trivariate histogram, and so on. The result was a nested array of univariate histograms which was stored with metadata in a MATLAB struct. Any events could be excluded from binning so that specific data could be studied (or “related” using a function below). This process is herein called “binning an essence,” and the struct created is herein called a “count.”

3.1.3 Operating on Counts

A function was written to plot counts with as many as five dimensions. E.g., a univariate histogram was visualized as a single curve, and a quinquevariate histogram was visualized as a video of rows and columns of colored surfaces. Figure 3.1 is an example of the default visualization of a bivariate histogram, a colored surface.

The goal of creating a multivariate histogram was to visualize data to find patterns by eye which were not apparent in lower-dimensional projections or to find a relation between the dimensions of the data, such as how amplitude changed with depth for the purpose of a depth calibration. A function was written to find these relations for arbitrarily high-dimensional counts by finding one value for each nested univariate histogram according to a given method, such as “take the mode of each univariate histogram,” “take the centroid of a Gaussian fit of each univariate histogram,” or “find where the curve falls below 10% of its maximum on the right side.” The result was a nested array of curves with one less dimension than the input count. These curves were stored with metadata as a MATLAB struct. This process was called “relating,” and the struct created was called a “relation.”

3.1.4 Operating on Relations

Relations were visualized the same way as counts, and any relation could be plotted on top of the count from which it was derived, e.g., Figure 3.9a later in this chapter.

When a relation was used to calibrate data, such as normalizing gain across all depths and pixels, an essence was first created which represented the relation. This essence was then mixed with an existing essence to create a new calibrated essence. E.g., the triggered-pixel amplitudes were divided by the photopeak centroids for each depth and channel to create depth- and channel- normalized triggered-pixel amplitudes.

An essence was also created from a relation when combining events according to an arbitrary parameter. An example of this is elaborated in Section 3.3.3.

A function was also written to perform element-wise arithmetic between relations from the same count. E.g., a count of events per energy bin per pixel was first binned – the energy spectrum per pixel. The relation between energy and pixel was then found for this count by geometrically calculating the FWHM of the data in the energy bins above 500 keV – the FWHM in keV for each pixel. The relation between energy and pixel was then also found for this count by taking the mode of the data in the energy bins above 500 keV – the peak position in keV of each pixel. The FWHM in keV was then divided by the mode and multiplied by 100 to yield the FWHM in percent.

Relations were found for existing relations just like relations were found for counts. E.g., a relation storing the FWHM for each pixel could be related by taking the minimum to find the best pixel’s resolution.

3.2 Workflow

A script was written to automate event reconstruction and calibration and to save the results, such as the calibrated energy spectrum and its FWHM, however this automation could not be optimized for the unpredictable anomalies found in many datasets. The purpose of the code often became to investigate these anomalies, thus the results of each step in the code were visualized and the next step in the code usually decided after each step of processing. The series of steps in processing a dataset is herein called a workflow.

A typical workflow when investigating data is shown in Figure 3.2. Depth calibration is represented as a single loop through the left-most black arrows. Multiple nonlinear paths appear because continual visualization is best when working with unpredictable data and because an anomaly may not be apparent until after the code has accounted for other anomalies.

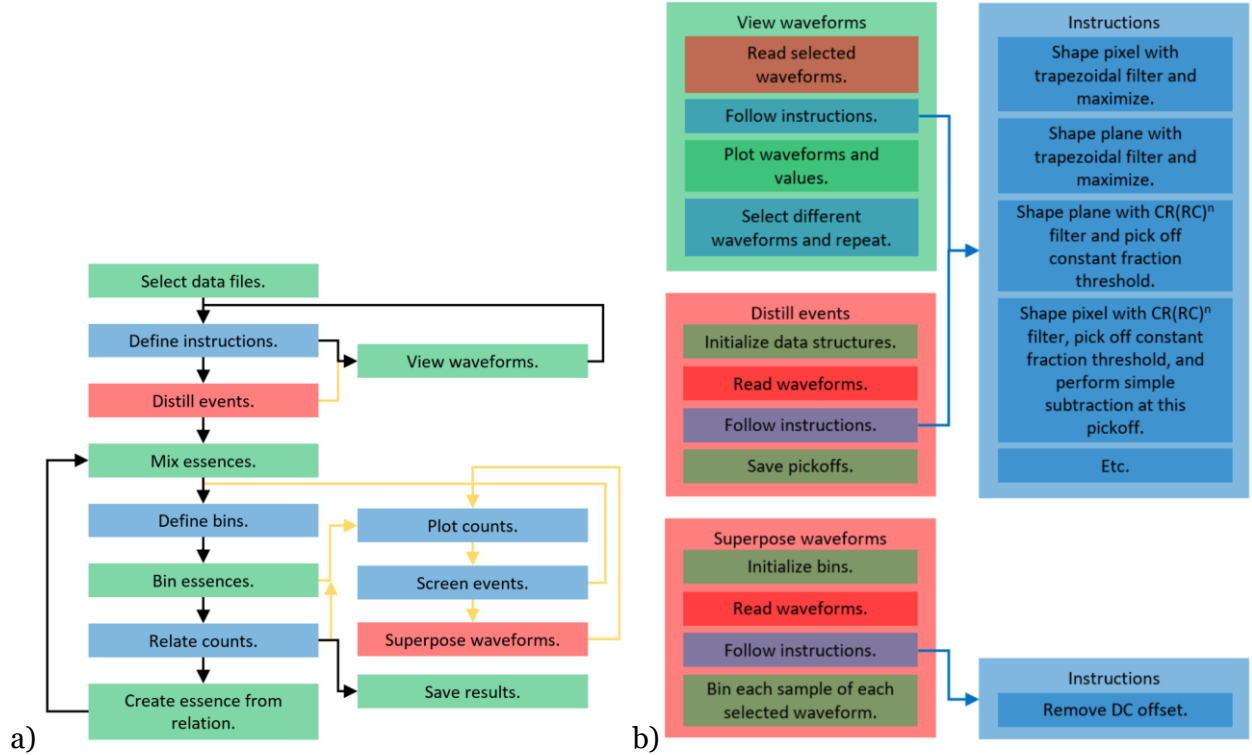


Figure 3.2. a) A typical workflow using the code. Begin at top, following arrows. Paths indicated by gold arrows were used to investigate anomalies. b) Expanded diagram of three functions with dependence indicated by blue arrows. Blue blocks represent code which may need to be adjusted if there are anomalies; red represents unavoidably slow code; green represents otherwise uninteresting code.

Waveforms were read from file as infrequently as possible because accessing the hard disk drives on which data was normally stored was relatively slow. Waveforms could not all be kept in RAM because raw data from a measurement often exceeded 100 GB.

3.3 Processing Example

The results of most steps in the workflow used to process the best measurement (-1250 V) from 11×11-pixel TlBr crystal 935-38AS3 are shown below, excluding investigations of anomalies, which are given in Chapter 4. Numerical results are shown in Section 7.1.1. These steps were typical of the processing of other crystals except where noted otherwise.

3.3.1 Waveform Processing

Raw waveforms, e.g., Figure 3.3a, were processed according to lists of instructions described in Table 3.1 to produce essences. The essences simplify the waveform into a few amplitude and timing values. These values were used to reconstruct a waveform

approximation, e.g. Figure 3.3b, which was checked by eye or occasionally with the reconstruction accuracy score discussed in Section 4.1.1 to ensure proper instructions were being used. The expressions defining the digital filter parameters were determined empirically through trial and error, but the predicted maximum drift duration was a motif. The expressions are shown in Table 3.2. They were frequently adjusted as waveform reconstructions deviated significantly from raw waveforms. Parameters were defined using the total number of samples in the waveform, S , the sampling frequency, f , the crystal thickness, D , the electron mobility, μ_e , the bias, V , and the pixel pitch, p . Trapezoidal filters were defined by a rise time and a flat top duration [34]. Negative times and thresholds indicate that the waveform was reversed in time before filtering. Some of these values were not used in the following example but were used for other investigations, such as pixel simple amplitude.

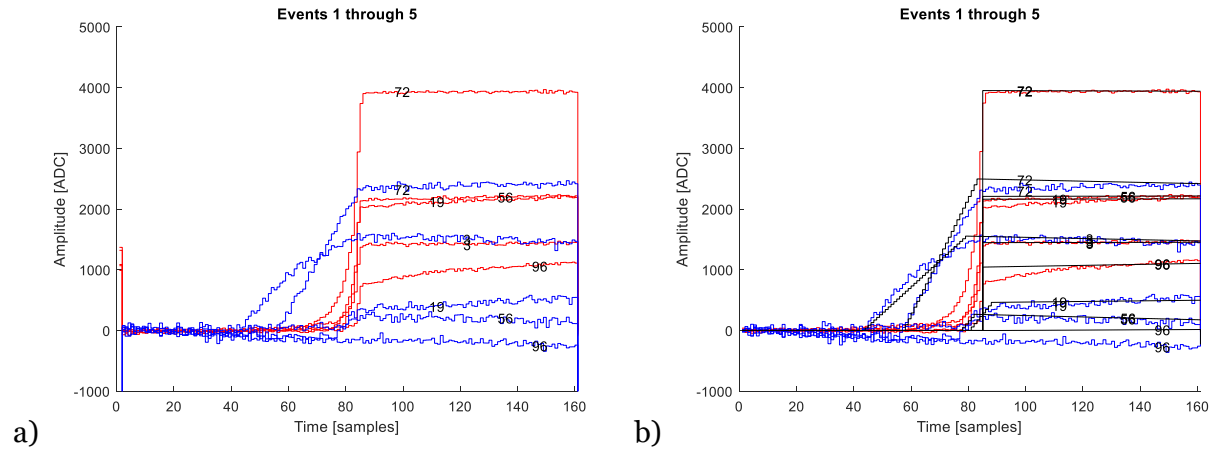


Figure 3.3. a) Raw waveforms and b) raw waveforms overlaid with waveform reconstructions.

Table 3.1. Essences distilled directly from the raw waveforms.

Essence	Instruction List
Triggered channel	(metadata)
Date recorded	(metadata)
Pixel simple amplitude	Simple subtraction
Pixel trapezoidal amplitude	Trapezoidal filter, maximize
Pixel stop time	CRRC filter, constant fraction threshold
Pixel prompt amplitude	Simple subtraction, but the tail is defined from the start of the pixel stop time
Plane simple amplitude	Simple subtraction
Plane trapezoidal amplitude	Trapezoidal filter, maximize
Plane start time	CRRC filter, constant fraction threshold
Plane collection time	CRRC filter, constant fraction threshold

Table 3.2. Parameters used in the instructions in Table 1.

Essence	Instruction Parameter	Value	Unit
Pixel Simple Amplitude	Baseline start	3	Samples
	Baseline end	$S/5$	Samples
	Tail start	$S \times 4/5$	Samples
	Tail end	$S - 3$	Samples
Pixel Trapezoidal Amplitude	Rise time	$S/5$	Samples
	Flat top duration	$1.5 \times f \frac{D^2}{\mu_e V}$	Samples
Pixel Stop Time	RC	$-0.1 \times f \frac{D^2}{\mu_e V} \times \frac{p}{D}$	Samples
	n	1	~
	Fraction threshold	-0.1	~
Pixel Prompt Amplitude	Baseline start	3	Samples
	Baseline end	$S/5$	Samples
	Tail start	pixel stop time	Samples
	Tail end	pixel stop time + 10	Samples
Plane Simple Amplitude	Baseline start	3	Samples
	Baseline end	$S/5$	Samples
	Tail start	$S \times 4/5$	Samples
	Tail end	$S - 3$	Samples
Plane Trapezoidal Amplitude	Rise time	$S/5$	Samples
	Flat top duration	$1.5 \times f \frac{D^2}{\mu_e V}$	Samples
Plane Start Time	RC	$0.04 \times f \frac{D}{\mu_e V}$	Samples
	n	1	~
	Fraction threshold	0.1	~
Plane Stop Time	RC	$-0.04 \times f \frac{D}{\mu_e V}$	Samples
	n	2	~
	Fraction threshold	-0.1	~

These essences were mixed to produce the essences in Table 3.3. (Plane-pixel ratio was not used in this example but was used in many other workflows.) Bins were defined

for each essence automatically by setting the bounds 10-20% outside the edges of each essence's distribution. The number of bins used varied, shown in Table 3.4; n.b., depth-binning has historically been coarser (40-60 depth bins). This work erred on the side of binning too finely to ensure subtle details were noticed during visualization, but this particular dataset was reprocessed with only 60 depth bins and the changes in resolution were less than 0.1 percentage points for overall and single-pixel resolutions.

Table 3.3. Mixed essences and their origins.

Essence	Produced by
Plane-pixel ratio	Plane trapezoidal amplitude / pixel trapezoidal amplitude
Drift duration	(Pixel stop time – plane start time) / f
Prompt-final ratio	Pixel prompt amplitude / pixel trapezoidal amplitude
Pixel	Find channel in a linearized pixel map
Row	Find the row corresponding to the channel in the pixel map
Column	Find the column corresponding to the channel in the pixel map

Table 3.4. Number of bins used to represent different distributions.

Essence Unit	Bins used in Univariate	Bins Used in Multivariate
ADC or keV	1500	750
μs (drift duration)	500	250
ADC/ADC	500	250

The distribution of all pixel trapezoidal amplitudes (the “raw energy spectrum”) and the bivariate distribution of pixel trapezoidal amplitudes and drift durations are shown in Figure 3.4. These distributions were found for each pixel; the distributions of pixel trapezoidal amplitudes for each pixel are shown in Figure 3.5. The photopeak centroid of each pixel was found and the amplitudes of all events for each pixel were divided by the photopeak centroid of their pixel and multiplied by the overall photopeak centroid. This operation corrected for variations in preamplifier gain between pixels so that resolution before depth correction could be calculated.

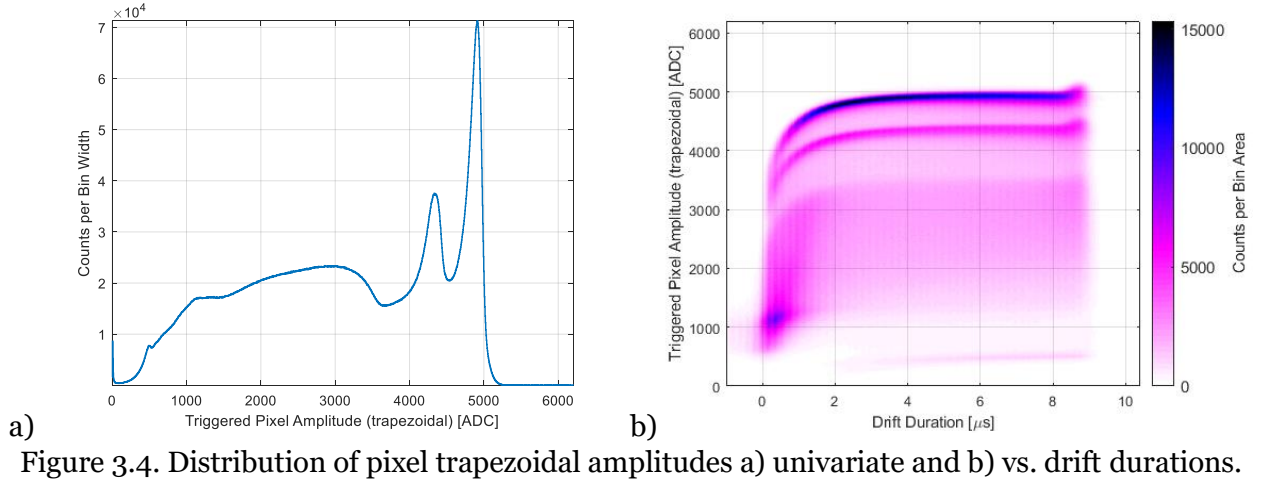


Figure 3.4. Distribution of pixel trapezoidal amplitudes a) univariate and b) vs. drift durations.

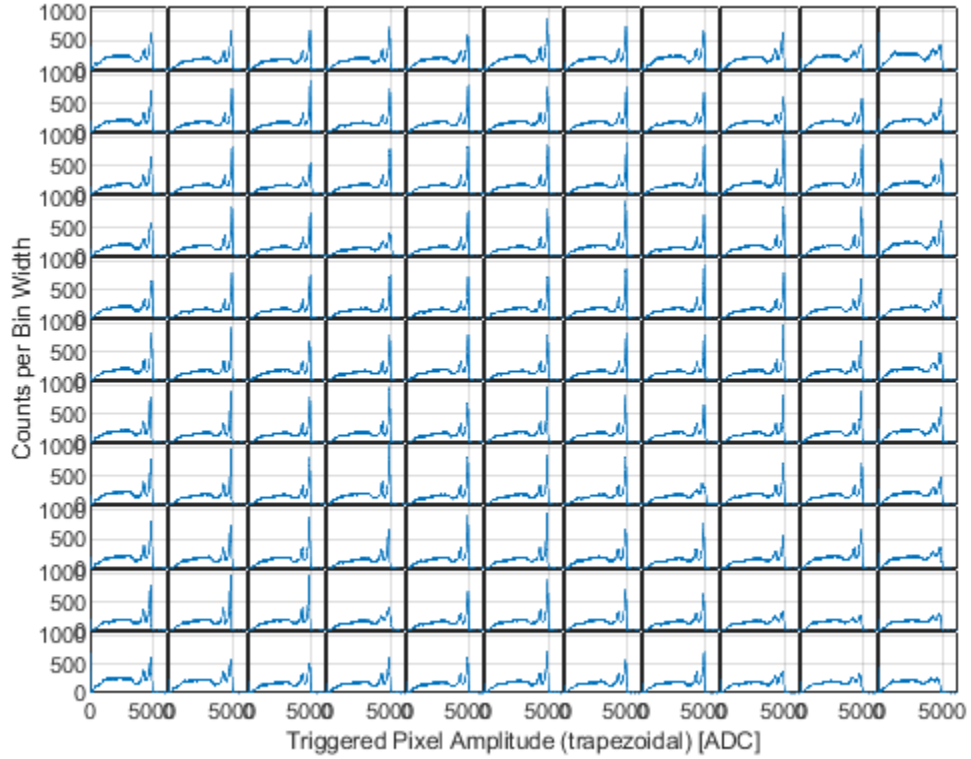


Figure 3.5. Pixel trapezoidal amplitudes for each pixel.

3.3.2 Depth Calibrations

Next, the data were calibrated by prompt-final ratio, the justification for which can be found in Chapter 5. This calibration was developed over the course of this work, so it was not applied to most results from 3×3 -pixel detectors. The bivariate distribution of prompt-final ratio and drift duration is shown in Figure 3.6. Prompt-final ratio is constant for all depths except near-pixel and near-plane. The bivariate distributions of pixel

trapezoidal amplitude and prompt-final ratio for the two regions are shown in Figure 3.7. There are different relationships between pixel trapezoidal amplitude and prompt-final ratio for the two regions as a result of different mechanisms (weighting potential gradient and Auger recombination, discussed in Chapter 5 and Section 4.2.4). Separate calibrations for the two regions were performed because of the different relationships. Both calibrations by prompt-final ratio were performed per pixel.

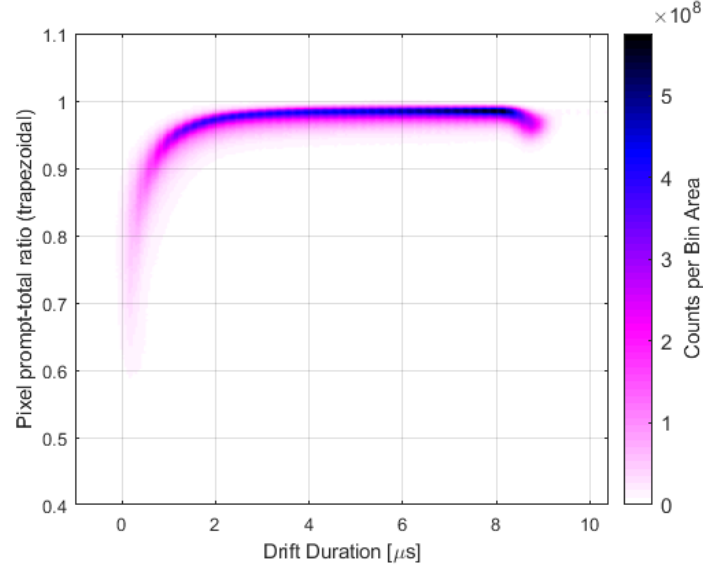


Figure 3.6. Bivariate distribution of prompt-final ratios and drift durations.

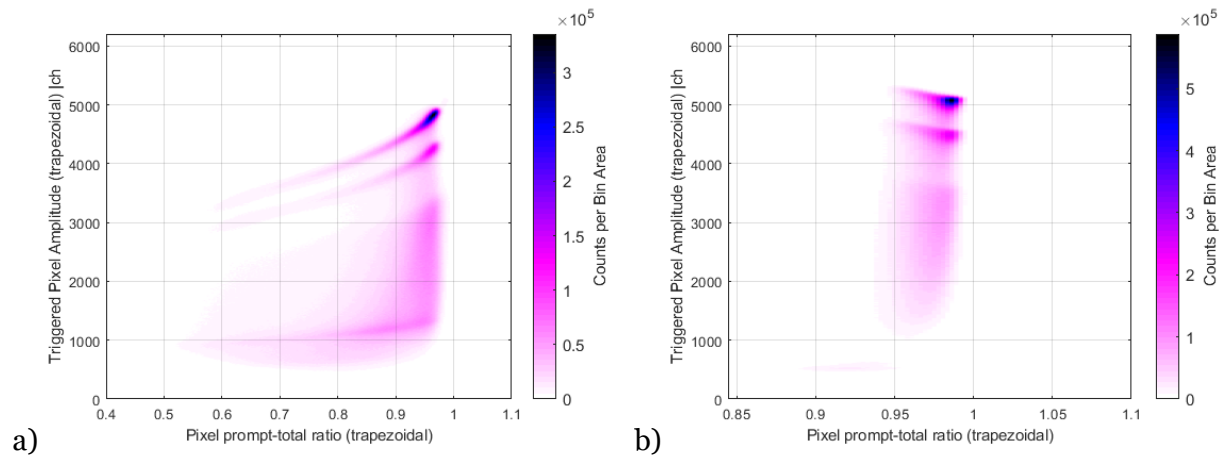


Figure 3.7. Bivariate distributions of pixel trapezoidal amplitude and prompt-final ratio a) within a pixel-pitch of the pixel and b) at drift durations greater than 8 μ s.

The bivariate distribution of prompt-final-ratio-calibrated pixel trapezoidal amplitude and drift duration is shown in Figure 3.8a. The poor resolutions near-pixel and

near-plane were improved (cf. Figure 3.4b). Discontinuities existed where the calibration region boundaries were defined which were corrected after a calibration was also performed by drift duration (per pixel), resulting in Figure 3.8b, which concluded depth calibrations. Calibration by drift duration is standard procedure for TlBr detectors, but sometimes calibration by plane-pixel ratio was used instead (see Section 7.1.3 for a comparison). The mode of the photopeak of the depth-calibrated pixel trapezoidal amplitudes was normalized to 661.7 keV, completing the energy calibration.

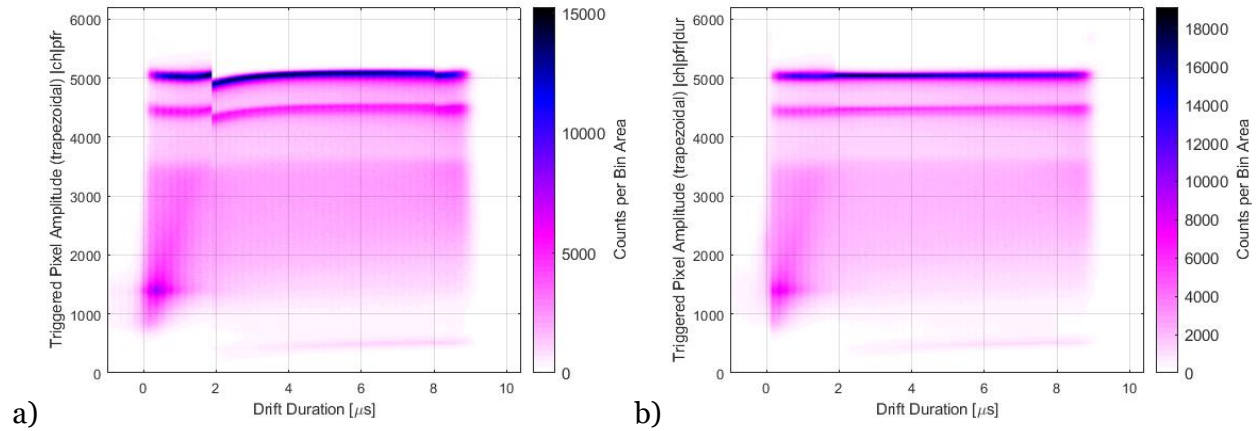


Figure 3.8. Bivariate distribution of pixel trapezoidal amplitude and drift duration a) after prompt-final-ratio calibration and b) after an additional drift-duration calibration.

3.3.3 Event Screening

Events suspected of experiencing incomplete charge collection (ICC) were identified and removed (“screened”) from the event population after depth calibration according to the model described in Chapter 6 by comparing depth reconstructions. ICC screening was only applied to a few crystals in this work.

The plane-pixel ratio was first recalculated using the energy-calibrated pixel amplitude to begin ICC screening. Events which fell within $\pm 0.5\%$ of the photopeak mode were then selected and the bivariate distribution of the plane-pixel ratios and drift durations from these events was found, shown in Figure 3.9a. Upper and lower bounds defining acceptable disagreements between the depth reconstructions were calculated by finding where the edge of each drift-duration-separated plane-pixel-ratio distribution dropped below 10% of its mode, also shown in Figure 3.9a. N.b. events above the upper bound are likely caused by ICC; events below the lower bound are likely caused by multiple interactions under the same pixel or by a vertically extended charge cloud

(consider Tl-x-ray emissions and bremsstrahlung from the photoelectron [35]). These bounds were used to screen events, resulting in the spectra shown in Figure 3.9b.

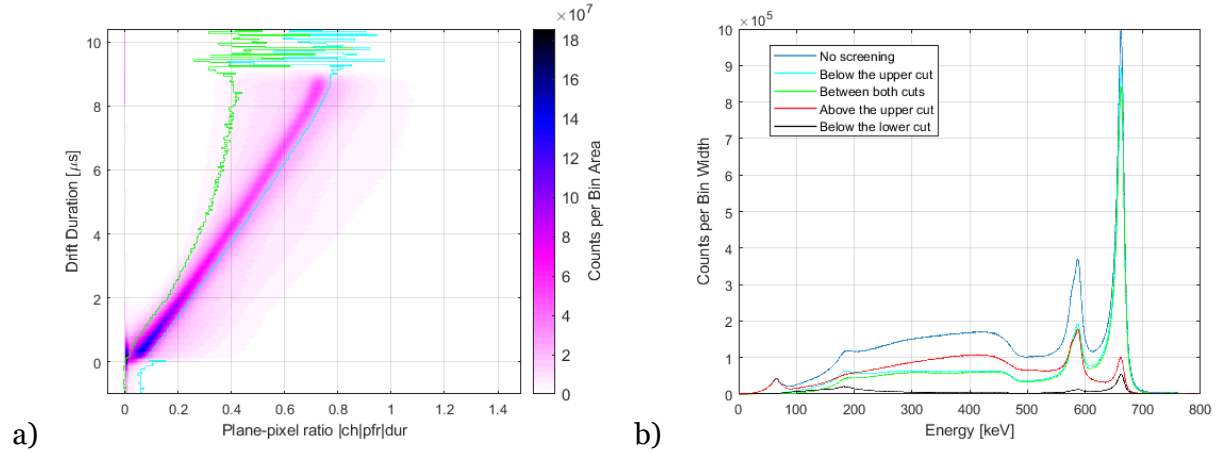


Figure 3.9. a) Bivariate distribution of the plane-pixel ratios and drift durations with upper and lower boundaries defining typical relations. b) Energy spectra within and without these bounds.

Removing events which fell either above the upper bound or below the lower bound resulted in the best energy resolution and highest ratio of photopeak counts to energy resolution (a figure of merit (FOM) used by the sponsor of this work) compared to including counts from outside of the bounds. The energy spectra from all pixels and from the best pixel after this step are shown in Figure 3.10 (cf. Figure 3.4a).

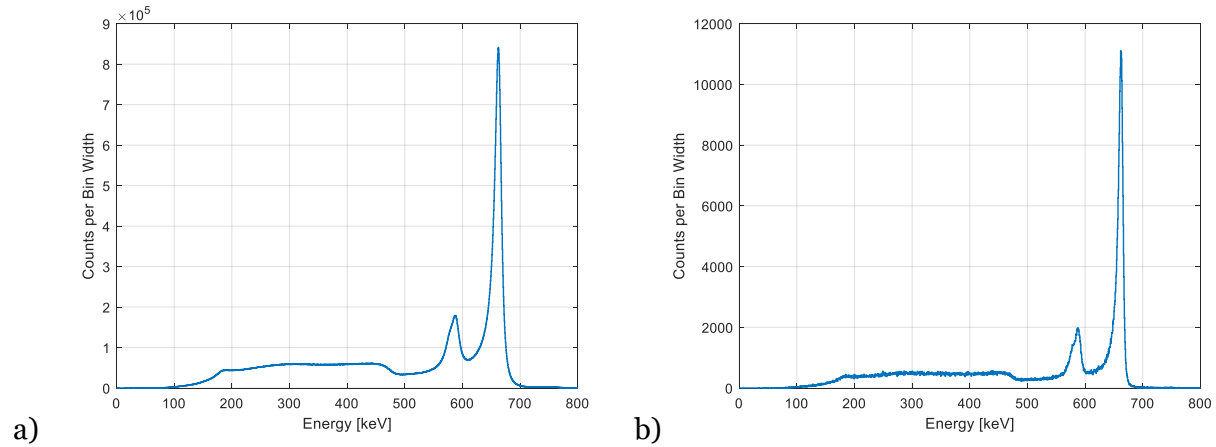
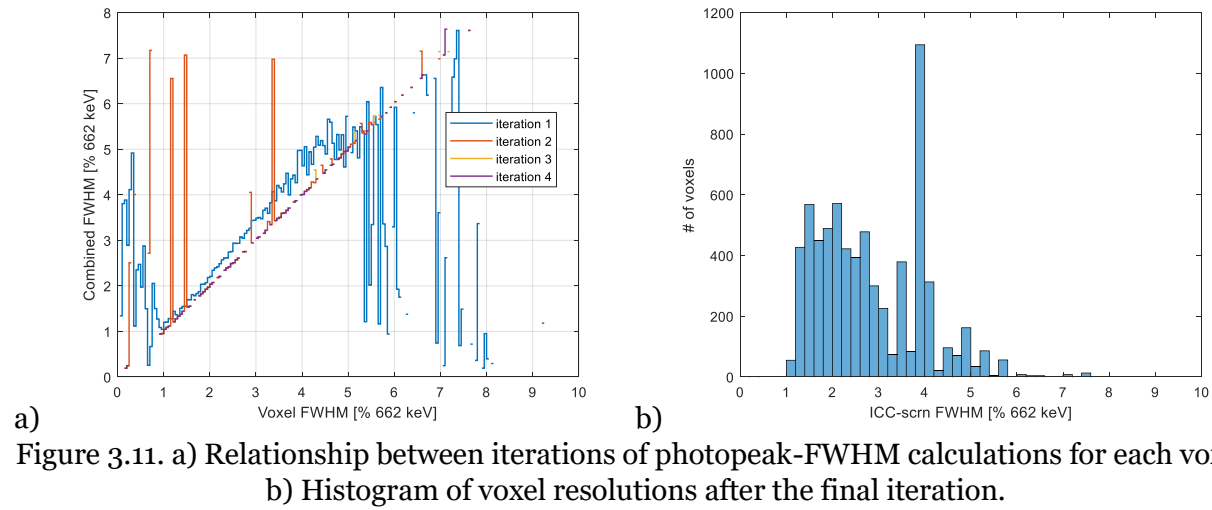


Figure 3.10. a) Overall single-pixel and b) best-pixel energy spectrum after ICC-screening.

Finally, events were screened according to the energy resolution of the voxel in which they occurred, allowing a compromise between better photofraction and FOM from a spectrum comprised of all pixels and the better energy resolution of a best-pixel spectrum. The FWHM for the energy spectrum from each voxel was first calculated (the first iteration), though the FWHM of many voxels was calculated incorrectly because of

poor statistics. The voxels were placed into classes according to their nominal resolution and the FWHM of the whole class was calculated (the second iteration). This was repeated two more times until the nominal FWHMs agreed well with the class FWHMs, shown in Figure 3.11a. The final distribution of voxels among the classes is shown in Figure 3.11b. The benefits of class discrimination are shown in Section 7.1.1.



Chapter 4 Anomalies Observed

4.1 Isolating Anomalous Events

4.1.1 Event-by-event Parameters

The effect of an anomaly often needed to be isolated to predict the ideal detector performance or to study other anomalies when multiple were present and interfering. Anomalous events were isolated and then studied or removed by visualizing the data multidimensionally where the value along each dimension was a parameter derived from the waveforms of an event. Examples are explained below.

Poor raw energy spectra were observed from a CdZnTeSe detector (shown in Section 7.2). The energy spectra were separated by two depth parameters, the plane-pixel ratio and the drift duration, to form two bivariate histograms (shown in Figure 4.1). Artifacts manifesting as vertical bands were identified in these plots. Bivariate histograms of the two depth parameters were then plotted (shown in Figure 4.2) from which the anomalous events could be isolated, studied, and removed. The events were suspected to be spontaneous discharge between the pixels and a secondary guard ring which was ungrounded because of a manufacturing error.

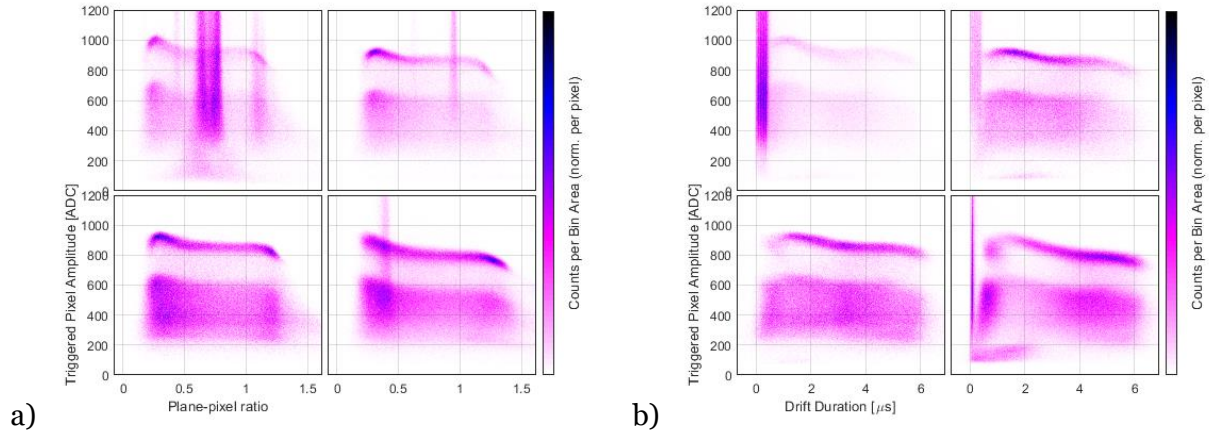


Figure 4.1. a) Plane-pixel ratio vs. pixel amplitude and b) drift duration vs. pixel amplitude for the four pixels of BNL2-S2.

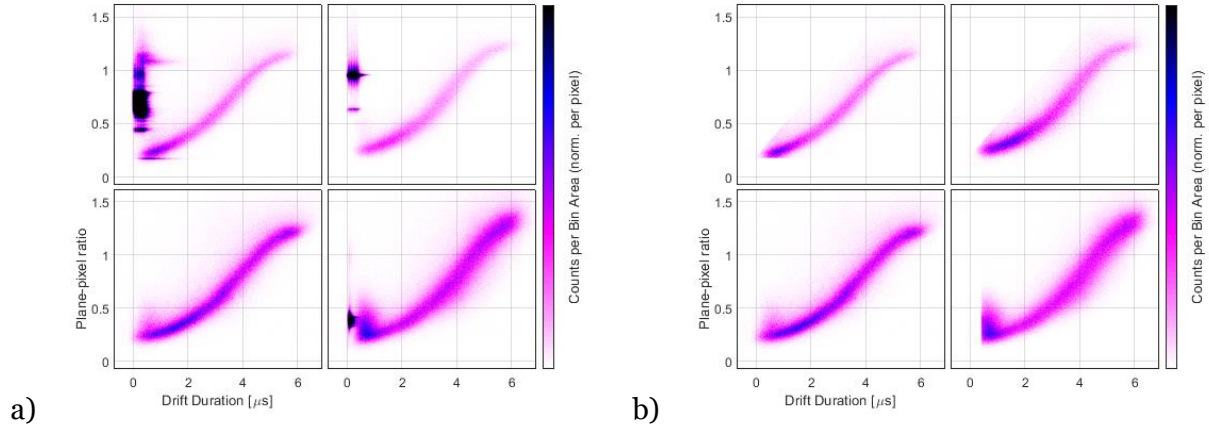


Figure 4.2. Drift durations vs. plane-pixel ratio for the four pixels of BNL2-S2 a) before and b) after anomalous events were removed.

The dimensions used to separate data were sometimes more complicated than a time or amplitude pickoff or a value arithmetically derived therefrom. A score of event-reconstruction accuracy was created and used to investigate some anomalies. Waveforms were approximated as simply connected line segments to calculate the score. The times of signal rise and signal stop for the pixel and plane waveforms were picked off using fast shapers and constant fraction discrimination, and the amplitudes of the waveforms were calculated for these times and at the beginning and end of the waveforms using simple subtraction, prompt subtraction, and trapezoidal filtering to create the waveform approximations. More details are given in Chapter 3. An example of four events' waveforms and their approximations are shown in Figure 4.3a-d.

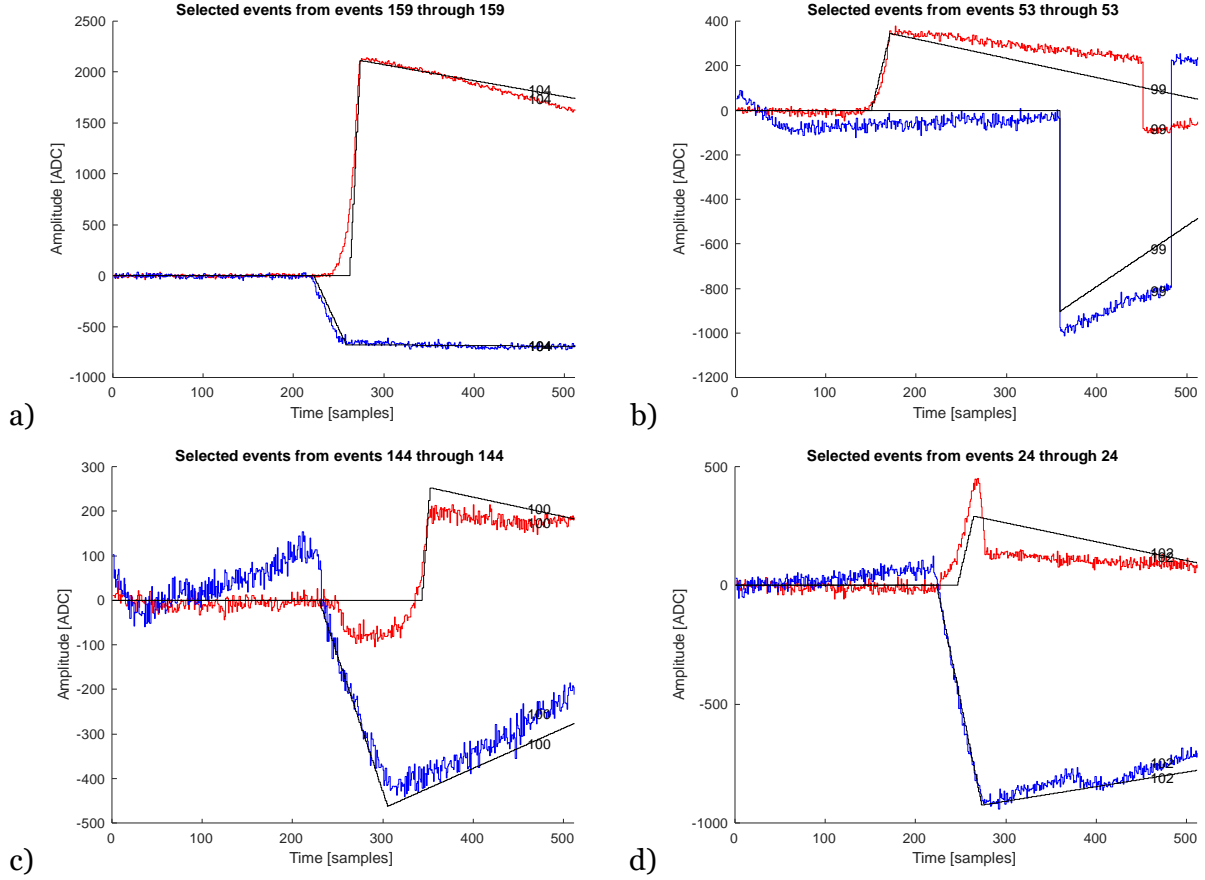


Figure 4.3. A a) typical and b-d) atypical pixel (red) and plane (blue) waveforms from one gamma-ray interaction in TlBr and their approximations (black).

The deviation of each waveform from its reconstructed approximation was quantified using

$$1 - R^2 = \frac{\sum_i (y_i - f_i)^2}{\sum_i (y_i - \bar{y})^2} \quad \text{Equation 4.1}$$

where R^2 is the coefficient of determination, y is the amplitude of an observed waveform sample, \bar{y} is the mean waveform amplitude, and f is the amplitude of a sample of the waveform's approximation; $1 - R^2$ is chosen for its more convenient range of zero to infinity. Zero is a perfect score. Intuitively, this tests how much better the reconstruction is than a horizontal line. Other statistical tests could be used instead. The score was then used as a dimension with which anomalous events were isolated. Figure 4.3a shows an event which scored well. Figure 4.3b-d shows events which scored poorly and contain anomalies identified as a digitizer malfunction, pulse pileup and a secondary neighboring

interaction, and triggering off the transient signal of a neighbor event. Screening by the pixel score alone was most practical because of higher noise on the plane waveforms.²

Other dimensions which physically represent incomplete charge collection were used to separate events and are discussed in Chapter 6.

4.1.2 Distribution-determined Parameters

Dimensions used to isolate events need not be solely defined by parameters defined for individual events. Parameters determined from distributions of grouped events were used to separate data. For example, events from a TlBr dataset were binned by voxel, i.e., binned by pixel and reconstructed depth, and the photopeak full width at half the maximum (FWHM) for the energy spectra produced by the group of events in each voxel were calculated iteratively (described in Section 3.3.3). A tradeoff between photopeak efficiency, resolution, and photofraction were optimized by setting the criterion “highest FWHM allowed of a voxel” from curves such as those in Figure 4.4. Undesirable events were discarded and desirable events were combined for the final energy spectrum. Separation of the data by this distribution-determined parameter was implemented to screen out poor events to estimate the ideal performance of this material, not to study the poor events.

² Because pixel waveform linearity depends on depth of interaction, its score was correlated with depth.

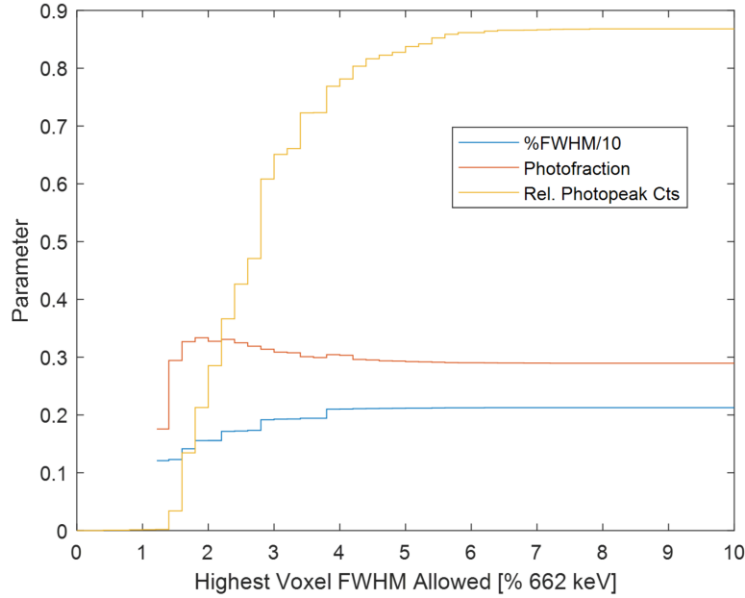


Figure 4.4. An example relationship between selective criterion (voxel energy resolution) and resolution, photofraction, and photopeak efficiency from 935-38AS3 (after depth corrections and screening of incomplete charge collection).

4.2 Anomalies Observed in Thallium Bromide

4.2.1 Transient Electron Lifetime and Leakage Current

Photopeak centroid was previously observed to increase and energy resolution was previously observed to improve during cooled operation of pixelated TlBr detectors in a repeatable way [2]. Photopeak centroid and leakage current were previously observed to decrease and energy resolution was previously observed to worsen during room-temperature operation of pixelated TlBr detectors [24]. A description of the historically accepted models describing these two phenomena is given in Section 1.5.1 with the names “conditioning” and “failure.”

During this work, photopeak centroids were generally observed to decrease as bulk leakage current increased during room-temperature operation of pixelated TlBr detectors. The cause of the photopeak changes was investigated and found to be a spatially homogeneous decrease in electron lifetime throughout the bulk evidenced by the example shown in Figure 4.5 and Figure 4.6. Maximum drift duration would increase if the phenomenon known as conditioning were occurring, but it remained constant. Changes in charge leakage due to a lateral electric field were also ruled out as the primary cause of the decrease in pixel signal because a decrease in plane signal was also observed.

Photopeak centroid remained linearly related to depth for interaction depths outside the near-pixel region indicating uniform trapping, but the relation with depth changed such that the photopeak centroid of events near the planar cathode was reduced by 20%.

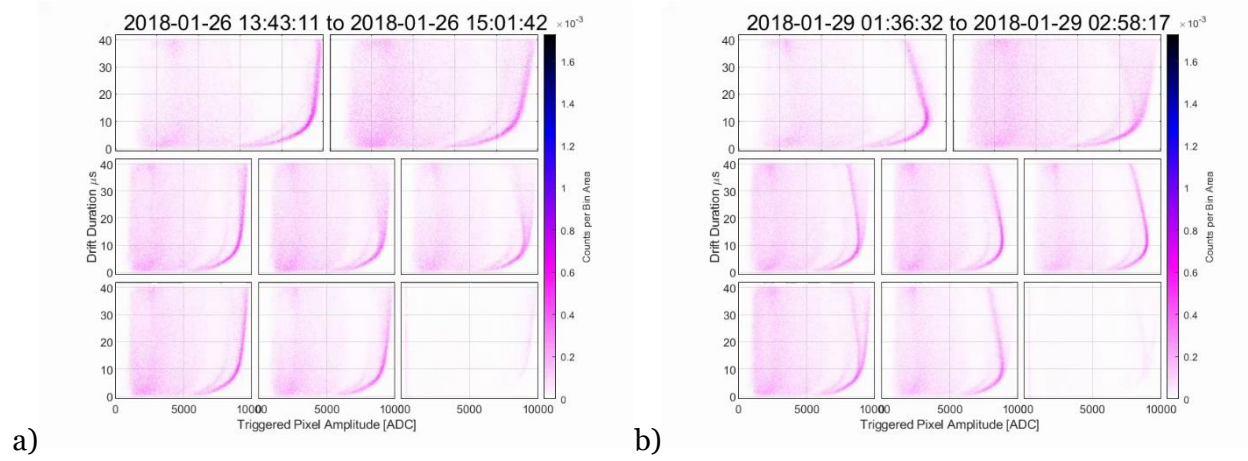


Figure 4.5. Cs-137 energy spectra from 1-cm-thick 138BS6(R) at -1000 V separated by depth from a) hours 1-10 and b) hours 42-51 of operation.

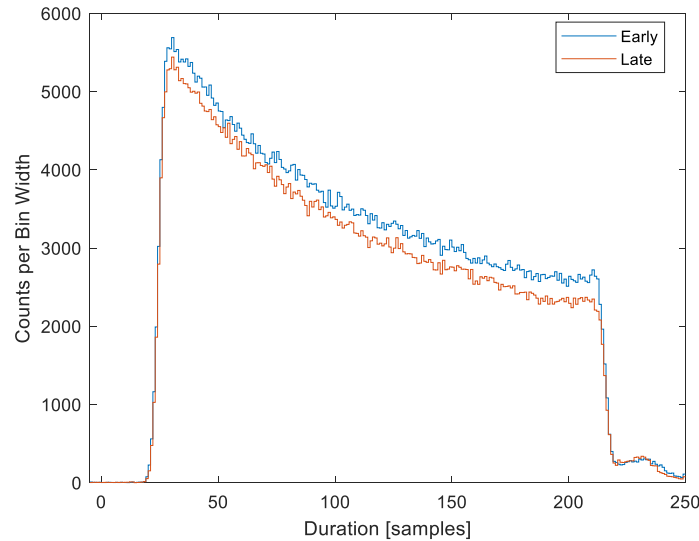


Figure 4.6. Distribution of drift durations for 138BS6(R) during hours 1-10 and 42-51 showing no increase in drift duration despite a change in photopeak amplitude.

The mechanism causing this phenomenon was therefore not a homogenizing of the electric field due to a sweeping out of space charge, which was the cause of conditioning at -20C [2] and presumably at room-temperature operation for HCl-etched crystals a few years ago [36]. These results likely differ from previous results because growth and manufacturing processes have been continually adjusted by RMD, Inc. to improve overall performance [18].

The decrease generally began immediately upon bias, so detector performance before the decrease could not always be well characterized. The energy resolution of the detector during the decrease, which occurred over one-to-several days depending on the detector, was poor because the decrease did not occur simultaneously nor perfectly uniformly throughout the detector, i.e., some subpixel regions underwent the change slightly more quickly than others. An example of a change in resolution is shown in Figure 4.7.

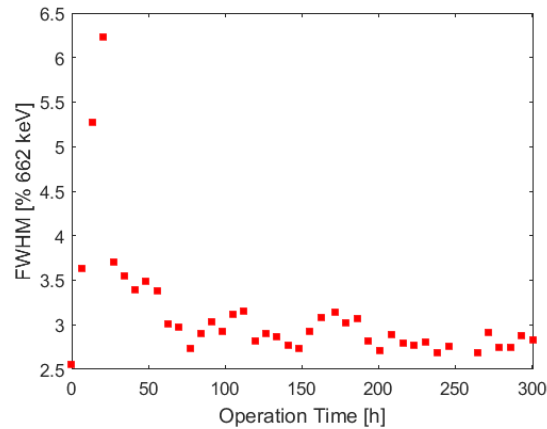


Figure 4.7. Finely time-binned energy resolution from the center pixel of 138BS6(R).

The initially better resolution is not observable with 24-hour time partitions because rapid changes in the response were integrated together (analogous to motion blur), so the energy resolution seemed to simply improve when older processing techniques were used, which deceptively appeared to be the previously classified “conditioning” phenomenon. Since the observed change in material properties was characterized by a decrease in photopeak centroid and did not include a change in electric field, this change in properties was more similar in mechanism to the phenomenon previously classified as “device failure” than conditioning.

The decrease in electron lifetime was very uniform once it finished decreasing in this example despite its magnitude. Figure 4.8 shows the energy spectra after depth correction before and after the change occurred. Both energy spectra have 2.8% energy resolution, therefore the trapping site density did not become less spatially uniform though it did increase. If the change in electron lifetime with time can be predicted or continuously measured, then perhaps a dynamic calibration could be applied which accounts for this temporal change, maintaining the best energy resolution possible during

this period of change. This detector degraded during operation during the month following these results to the point that a depth correction could not be performed.

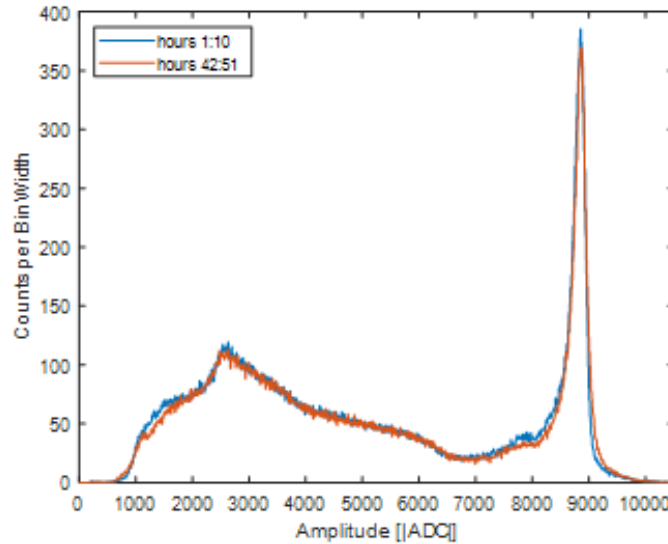


Figure 4.8. Self-calibrated Cs-137 energy spectra from 138BS6(R) from hours 1-10 and hours 42-51 of operation.

The resolution degraded from 3% to 7% depth-corrected during subsequent operation forty days after storing 138BS6(R) after the previously discussed measurement. Electron lifetime was observed to improve, increasing the planar-cathode-side photopeak centroid 20% over the first five days of subsequent operation. This seems to be a reversing of the change shown in Figure 4.5. The cause is unknown. After the first five days of subsequent operation, resolution at all depths worsened, likely caused by conventional failure at the anode, which is a migration of the electrode into the bulk, and testing was ended.

Before operating the detector to produce Figure 4.5–Figure 4.8, an I-V curve of the planar cathode shown in Figure 4.9 was recorded showing hysteresis, i.e. a resistivity that depends on the bias history. Rapid changes in leakage current in the red curve are likely electrical breakdown, and jagged peaks in the blue curve are likely measurement errors due to instantaneous changes in applied bias. This change in resistivity may have had the same cause as the change in electron lifetime.

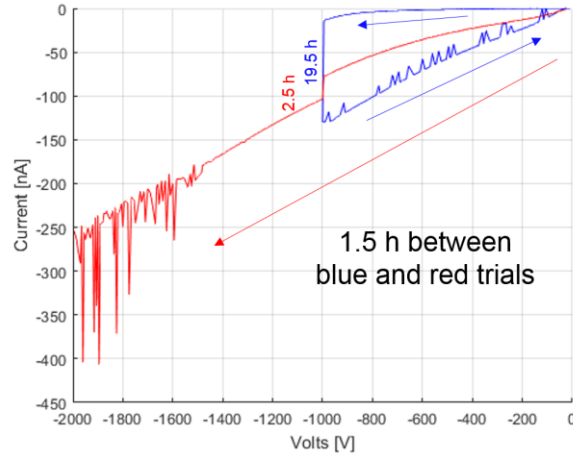


Figure 4.9. I-V curve of 138BS6(R) before operation.

The leakage currents through the pixels of this detector were measured during later operation using the technique described in [24], and the primary increase in leakage current was found to come through the bulk material, not the surface, as shown in Figure 4.10 and Table 4.1. Perhaps the electron lifetime decreased and the leakage current increased because defects formed uniformly throughout the bulk during this time as uniformly distributed neutral complexes dissociated while under bias, forming defects which provided intermediate energy states which act as traps to the freed electron cloud and which act as step stools for thermally excited valence electrons to reach the conduction band.

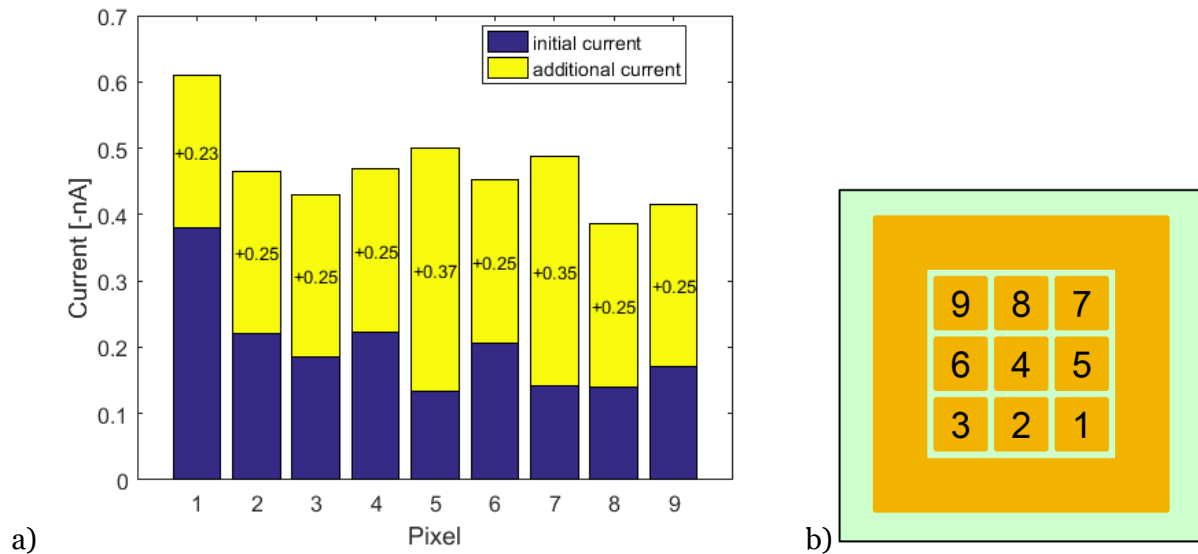


Figure 4.10. a) Leakage current measured through the pixels of 138BS6(R) during the beginning and end of operation over about a day a month later. b) Pixel locations.

Table 4.1. Leakage currents through electrodes of 138BS6(R).

Time	Cathode [nA]	Anodes [nA]	Guard [nA]
Early	7.4	1.8	5.6
Δ	+3.1 (+42%)	+2.4 (+133%)	+0.7 (+13%)
Late	10.5	4.2	6.3

4.2.2 Other Examples of Transient τ_e and I_L

Changes in electron lifetime and leakage current are the most prevalent and hindering issues recent TlBr detectors have faced, so exhaustive examples are given below to demonstrate the types observed.

A change in electron lifetime was first noticed in this work in detector 139BS3-1(R) when pixelated anode amplitudes decreased by 7% and planar cathode amplitudes reduced by 5% over the first day of operation. It was next noticed in 138BS6(R), the case study of which was just shown. It was next noticed in 175CS5-4, in which a profound decrease in electron lifetime, visible in Figure 4.11, was accompanied by an increase in leakage current of about 35%, shown in Figure 4.12.³

³ A growing low-single-pixel-count region, another anomaly, can also be seen at deep depths across the top pixels in Figure 4.11; this type of anomaly will be illustrated later in this section.

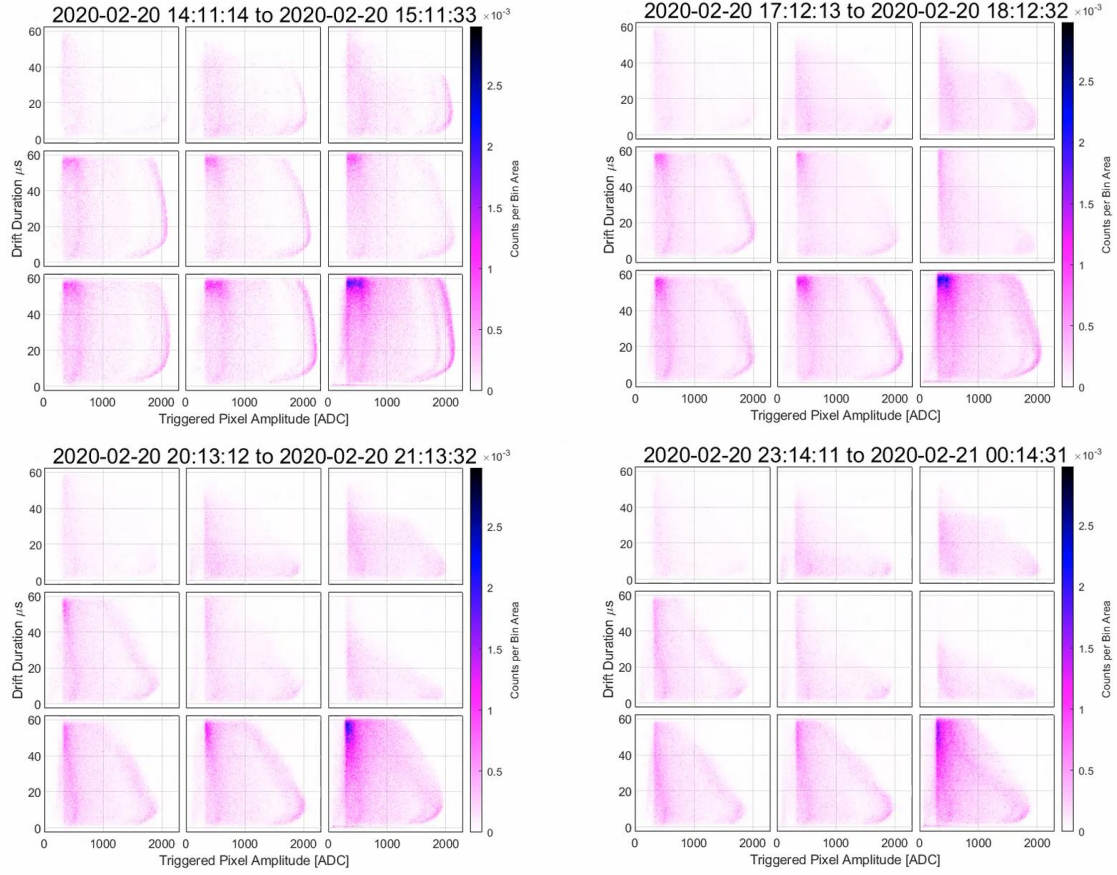


Figure 4.11. Bivariate histograms showing response of 175CS5-4 over four periods during the same experimental conditions at -1200 V over 12 mm.

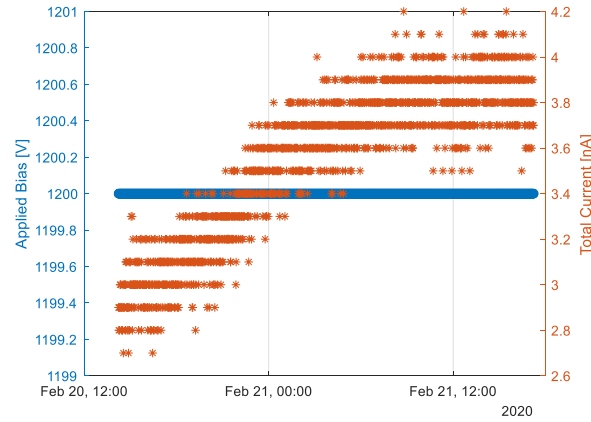


Figure 4.12. Leakage current during the measurement shown in Figure 4.11.

What appeared to be a slight increase in electron lifetime in some pixels of 175CS5-4 was observed over about a day immediately after the bias was raised following the aforementioned measurement, accompanied by a decrease in leakage current shown in Figure 4.13, but photopeaks were not identifiable at any depth. Intermittent spikes in

leakage current historically referred to as “breakdown” began at this higher bias and the leakage current exponentially increased. These current spikes and gradual increase in current were regularly observed in TlBr detectors. The high current was thought to be along the surface of the crystal from the planar cathode to the grounded guard ring since it did not always disrupt pixel signals. It rendered the planar cathode signal useless, effectively halting the measurement.

Figure 4.13. Unstable current observed in 175CS5-4.

The exponential increase in leakage current exemplified by Figure 4.13 was not always plagued with current spikes, nor was it always permanent. Figure 4.14 shows an example of an increase in leakage current which temporarily subsided. Other measurement issues precluded spectroscopic results from this detector.

Figure 4.14. Leakage current through 171A2 showing temporary recoveries of stability.

The reduction in signal amplitudes in Figure 4.5 would theoretically also be explained by a change in charge sharing, not just charge trapping, if full signal induction was observed on the planar cathode. The planar cathode signal amplitudes were studied

and found to decrease over time with the pixel amplitudes. The relations between plane-pixel ratio and depth from drift duration were thus consistent with charge trapping and not charge sharing according to the technique described in Chapter 6.

A change in electron lifetime was next observed in 128BAS3(R), in which bulk electron lifetime increased during the first 36 hours of operation as leakage current decreased. Note that all observations mentioned thus far have displayed a negative correlation between electron lifetime and leakage current. Consecutive biases of 128BAS3(R) showed slight daily oscillations in electron lifetime positively correlated with leakage current. Current peaks occurred at around 21:00-22:00 and current troughs occurred around 08:00 daily. These may correspond to room temperature fluctuations. Perhaps a positive correlation was only observed because there was a mechanistic delay between the two periodic patterns.

A change in electron lifetime was next observed in 175CS5-1(RR). Before refabrication, this crystal performed as well as 2.5% FWHM at 662 keV at low voltages but electron lifetime decreased significantly over time while the bias was ramped. The crystal was refabricated, and electron lifetime slightly improved over days of operation but was still very low. Intermittent spikes in leakage current and an exponential increase in leakage current were eventually observed. This crystal also experienced double peaking in three pixels which changed with time. Double peaking will be illustrated with the next example.

Other examples of changes in electron lifetime, usually decreasing, were observed in 172BS2-2(R), 171CS5-3, 171BS5-1(R), and 171BS5-2(R).

4.2.3 Binary Distributions

Electron-lifetime reduction was also observed in 11×11-pixel 935-38AS3 but only in the pixels marked in red in Figure 4.15. The reduction in photopeak centroid at -1000 V over 5 mm was only 3-4% for these pixels on average and did not continue after about the first 12 hours. Low-single-pixel-count (“low-SP”) regions which recovered were observed in the pixels marked in green, and double peaking was observed in pixels marked with an “X”.

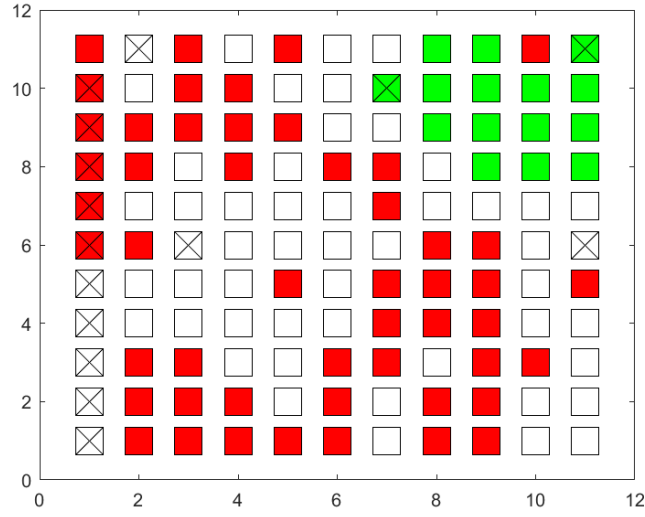


Figure 4.15. Pixel map of 935-38AS3 indicating where each phenomenon was observed. Red indicates electron lifetime decrease, green indicates low-SP-region disappearance, and X indicates double peaking.

Low-SP regions are spatial regions within a detector which produce less single-pixel events than expected either because heavy trapping lowers the amplitude of even photopeak events below the trigger threshold or because lateral drifts of the charge clouds cause ordinarily single-pixel events to be promoted to multi-pixel events by leaking charge to neighboring pixels. The aggregated response from all of 935-38AS3's pixels which initially exhibited low-SP regions is shown in Figure 4.16. The low-SP regions mostly dissipated after one day of bias. These low-SP regions were likely caused by lateral charge drift since a lateral variation in drift durations was also observed (reported in Section 7.1.2).

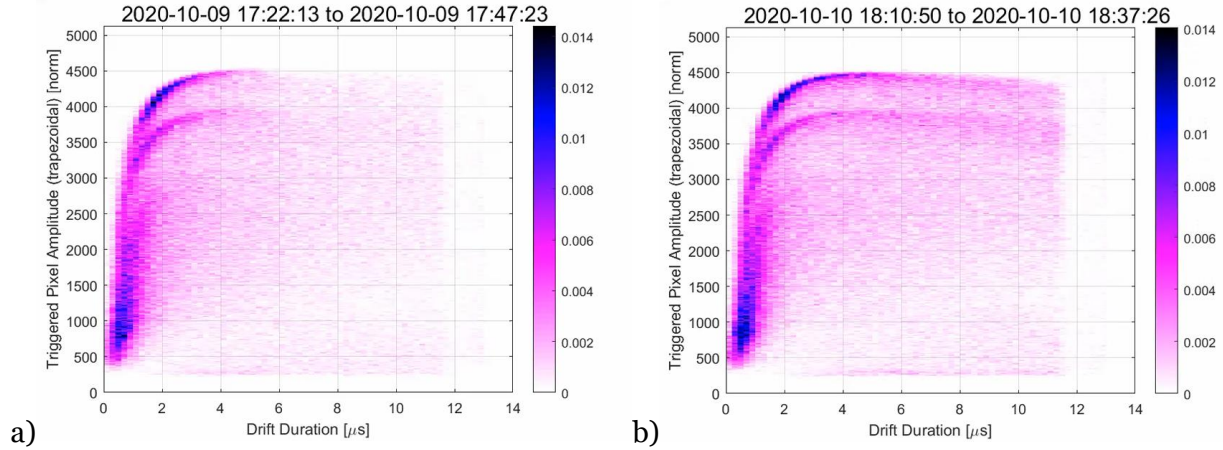


Figure 4.16. Bivariate histograms showing the combined response of all pixels marked in green in Figure 4.15 a) early in the measurement and b) one day into the measurement.

Double peaking occurs when a single pixel's response exhibits two distinct photopeaks (or would-be photopeaks if resolution is very poor) with different centroids. An egregious example is shown in Figure 4.17. Double peaking may be caused by a discrete change in charge collection efficiency with time or by discrete spatial regions underneath a pixel which have different charge collection efficiencies. The double peaking indicated in Figure 4.15, including that displayed in Figure 4.17a, was observed throughout the measurement thus is likely the result of different charge collection efficiencies in discrete spatial regions.

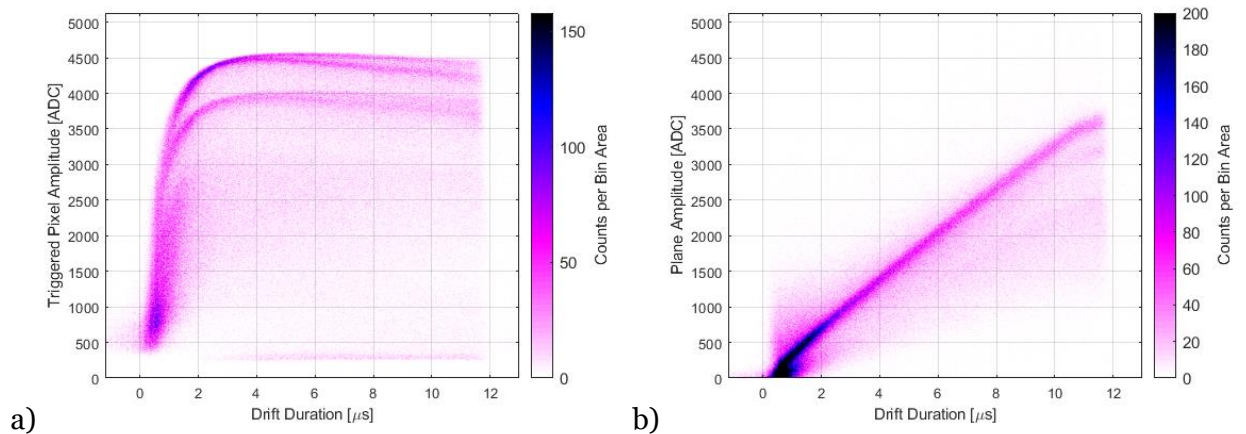


Figure 4.17. Bivariate histogram showing the response of a) pixel 58 (i.e., pixel (3,6) in Fig. 19) and b) of the plane from events which triggered pixel 58, which exhibit double peaking.

The response of the planar cathode was studied to determine the cause of double peaking. No double peaking is easily observed in the photopeaks from the planar cathode at different depths shown in Figure 4.17b, so charge sharing is suspected, though the

energy resolution is poorer and trapping is not expected to reduce the photopeak centroid of the plane as much as the pixel because of its linear weighting potential. The exact cause of decreased charge collection efficiency is not known, but a defect spatially confined to the depths corresponding to between about 4- and 6- μ s drift durations is suspected.

Low-SP regions do not always recover during bias, as is the case of 11 \times 11-pixel 6-mm-thick 150B2, which was operated in the VAD_UMv2.2 system. Collimated irradiation was used to determine which depths produced triggers, the results of which are shown in Figure 4.18. Even after extended bias and high bias, no change in the active depths were observed. In this case, multi-pixel events were also found to be absent at deep depths, so a region of high trapping at around 2 mm from the pixels was suspected.

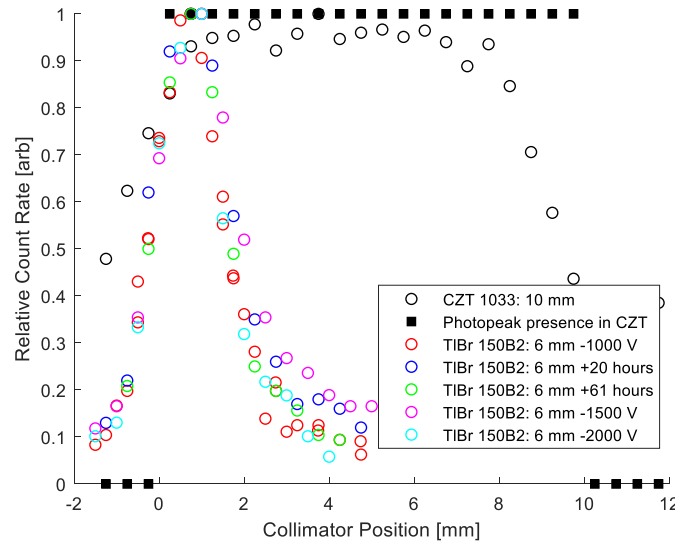


Figure 4.18. Count rate as a function of collimated depth showing region of low counts from all pixels after biasing.

4.2.4 Localized Auger Recombination

Most TlBr detectors do not seem to exhibit Auger recombination. In this work, Auger recombination was observed for events near the planar cathode in 935-38AS3 at -1250 V over 5 mm, but at no other depths, so it can be concluded that Auger traps were only present at the planar cathode's surface. Aggregate waveforms showing the delayed pixel signal characteristic of Auger recombination are shown in Figure 4.19 alongside ordinary photopeak waveforms from the same measurement. A subtle rise in the waveforms after electron collection can be seen for the Auger events. The increase in the amplitude of photopeak events caused an increase in the photopeak centroid of near-

plane energy spectra, visible in Figure 4.20a. This extra charge also affects the prompt-final ratio discussed in Chapter 5, shown in Figure 4.21. No Auger recombination was observed during operation at -1000 V, shown in Fig. 25b, which occurred 13 days before operation at -1250 V. Less Auger recombination was observed at the beginning of operation at -1250, but grew in over the first few hours, as evidenced in Figure 4.22, and then reduced again by the end of the measurement. (The response from pixel 70, which was used for the other figures, has poor statistics when separated by time, so the response of all pixels is shown in Figure 4.22.) The increase in Auger recombination over time was consistent with previous observations [35], but the cause of the subsequent decrease in Auger recombination later in the measurement is unknown.

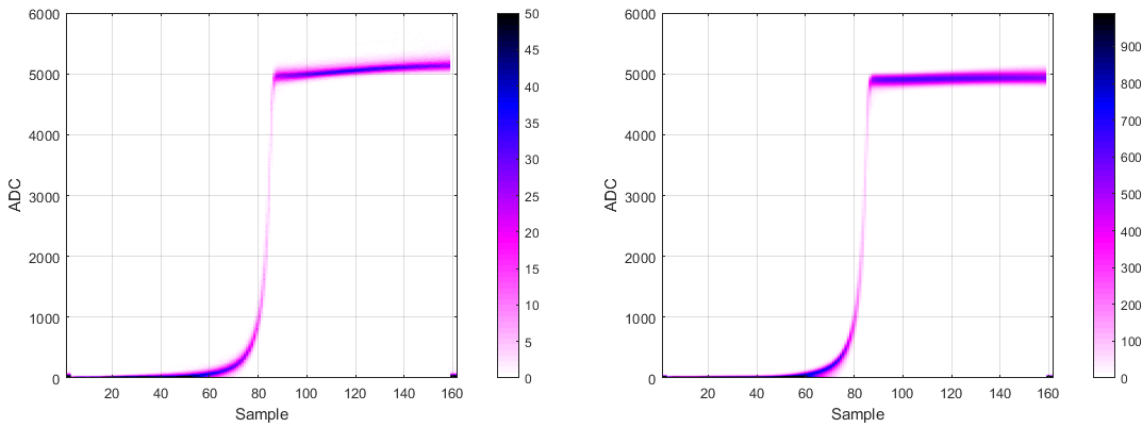


Figure 4.19. Bivariate histograms showing superposed pixel waveforms (amplitude vs. digitized sample number) from a) photopeak events exhibiting Auger recombination b) ordinary photopeak events which occurred at a slightly shallower depth in 935-38AS3 at -1250 V.

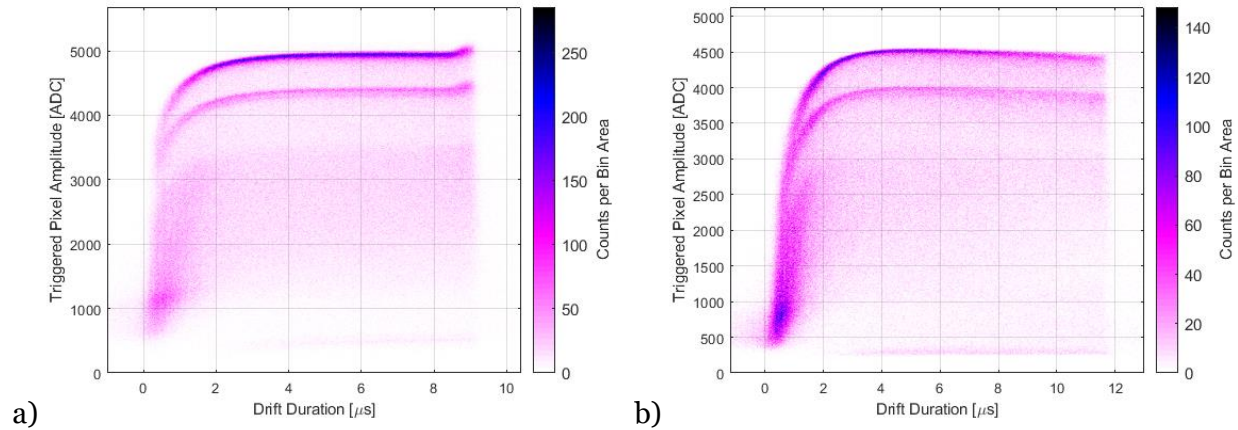


Figure 4.20. Bivariate histogram showing response of pixel 70 from 935-38AS3 at a) -1250 V and b) -1000 V. Most pixels were similar.

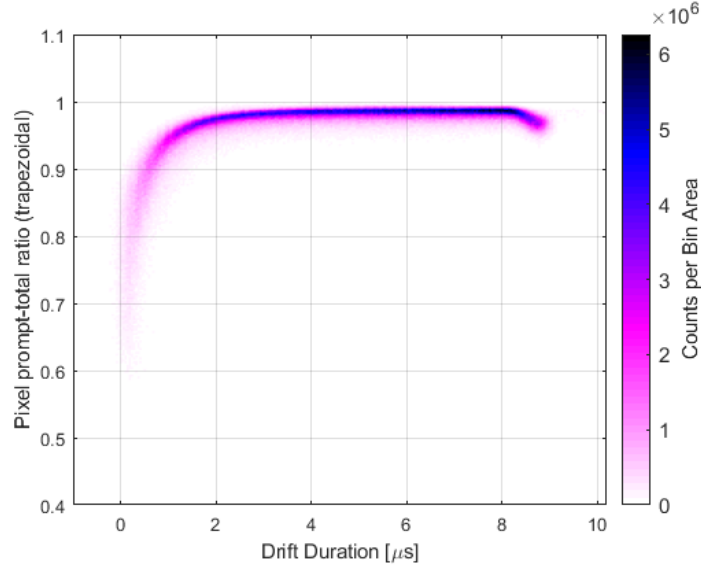


Figure 4.21. Relation between prompt-final ratio and drift duration for pixel 70 of 935-38AS3 at -1250 V showing near-plane distortion from Auger recombination (drift durations greater than 8 μ s).

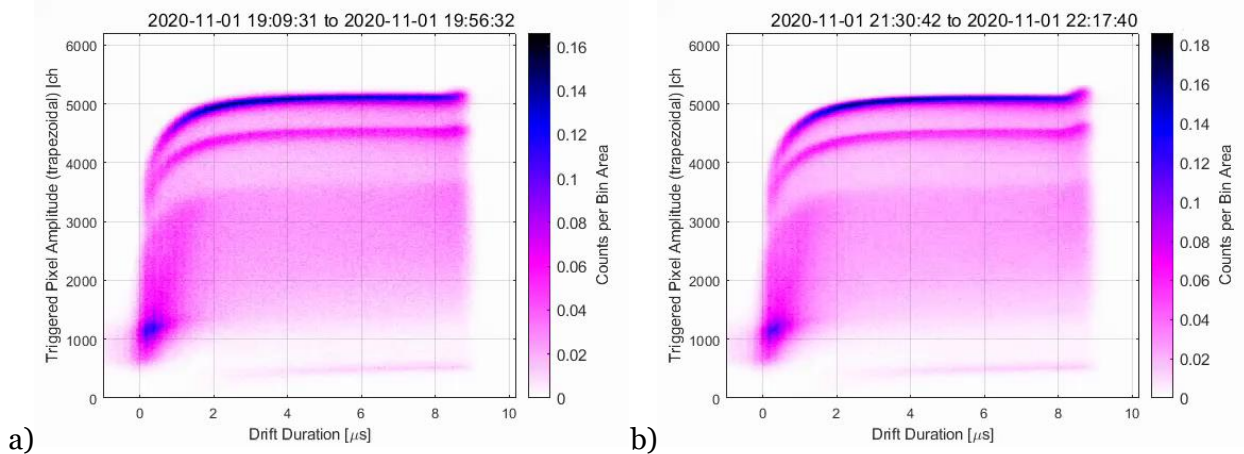
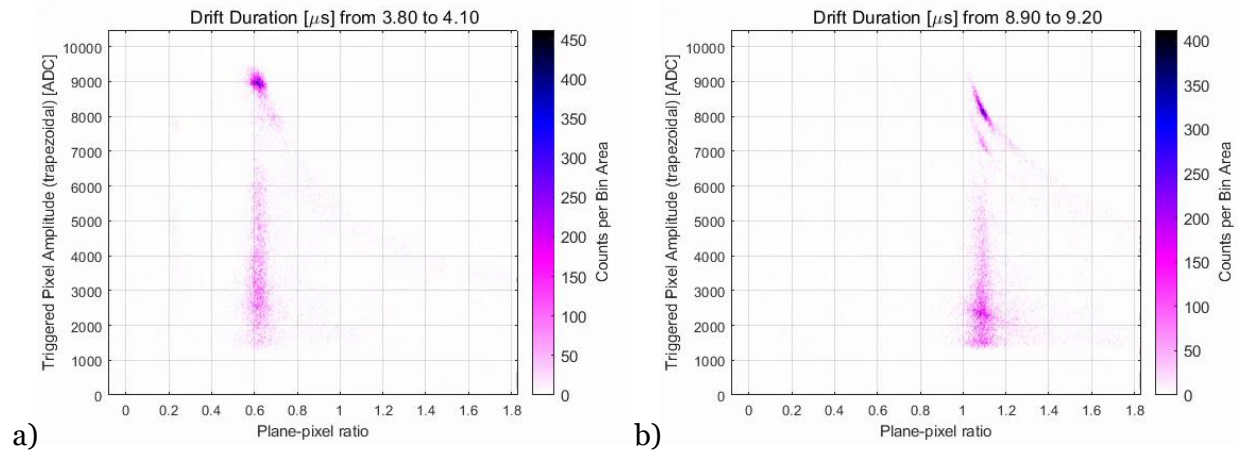
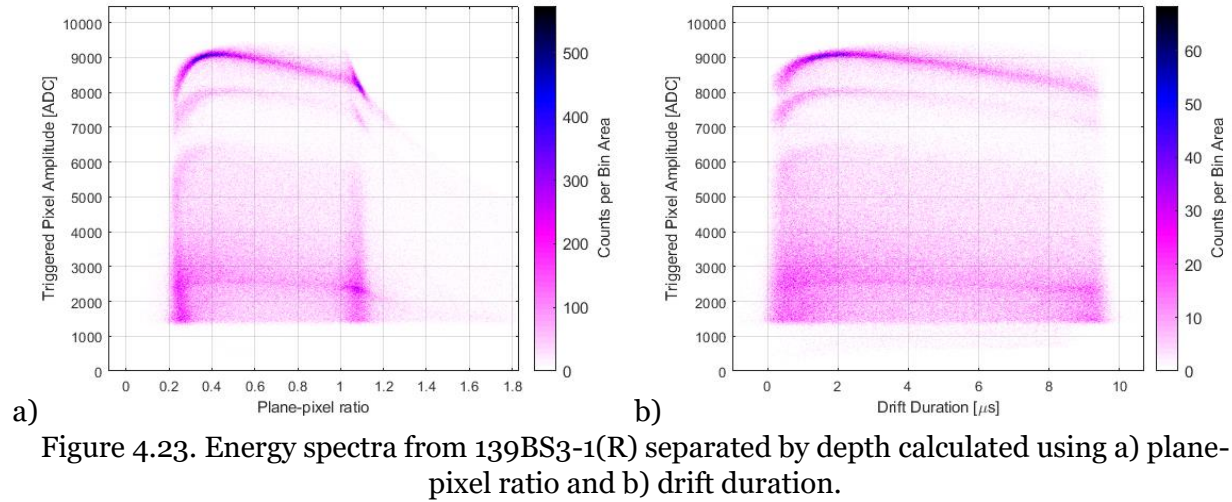


Figure 4.22. Bivariate histogram showing response of all pixels from 935-38AS3 during operation at -1250 V a) at the beginning of the measurement and b) over two hours into the measurement.

4.2.5 Variable Incomplete Charge Collection

A strange feature was noticed in the plane-pixel-ratio-separated energy spectra of 139BS3-1(R), shown in Figure 4.23a at $x > 1$, $y > 6500$. The feature did not appear in the drift-duration-separated spectra shown in Figure 4.23b. The events in the feature were isolated by separating events by drift duration, examples of which are shown in Figure 4.24. It was found that the feature in Figure 4.23a is caused by hole-collection events

(corroborated by waveform shape, not shown; see Chapter 5 for elucidation), but this feature was not observed in other detectors which experienced hole-collection.



The effect of hole collection on planar cathode waveforms was previously shown to distort plane-pixel-ratio reconstructions of all near-plane events to be reconstructed to the plane surface because the complementary hole motion causes complete charge induction on the plane [35], but any relation between pixel amplitude and plane-pixel ratio at these depths was not discussed. An inverse relation between pixel amplitude and plane-pixel ratio does exist of course, thus any photopeak hole-collection events with significant variance in pixel amplitude will produce the feature in Figure 4.23.

An inverse relation between pixel amplitude and plane-pixel ratio can similarly be seen at other depths for events with atypical plane-pixel ratios, such as those events with plane-pixel ratio above 0.65 in Figure 4.24a. These aberrations must occur because there is a larger deficit in the pixel signal than in the plane signal due to some mechanism such as incomplete charge collection. The bivariate distribution of plane amplitude and pixel amplitude for the events in Figure 4.24 are shown in Figure 4.25. Plane amplitudes have zero correlation with pixel amplitudes along the band of events between $5000 < y < 6000$ in Figure 4.25a which form the photopeak and tail in Figure 4.24a. These events and the distortion of the plane-pixel ratio in Figure 4.24a therefore correspond to charge sharing events. The same is faintly present in Figure 4.25b but another relation is clear. Plane amplitudes are positively correlated with pixel amplitudes for most photopeak events in Figure 4.25b indicating that charge trapping caused the variation in pixel amplitude of these events. This weak correlation is present for distributions from all deep depths in this dataset but approaches zero correlation for mid-to-near-pixel depths, which is why it is not pronounced in Figure 4.25a. This is consistent with the charge trapping model presented in Chapter 6, which is elaborated there. This correlation has likely not been studied before because the variation in plane amplitude due to depth uncertainty ordinarily obscures the variance in plane amplitude due to charge trapping, but the only variation in plane amplitude for hole-collection events is due to electron or hole collection efficiency. The variation in pixel amplitude is larger than the variation in plane amplitude, so the variation must be due to variation in electron trapping, not hole trapping, for these cathode-side events.

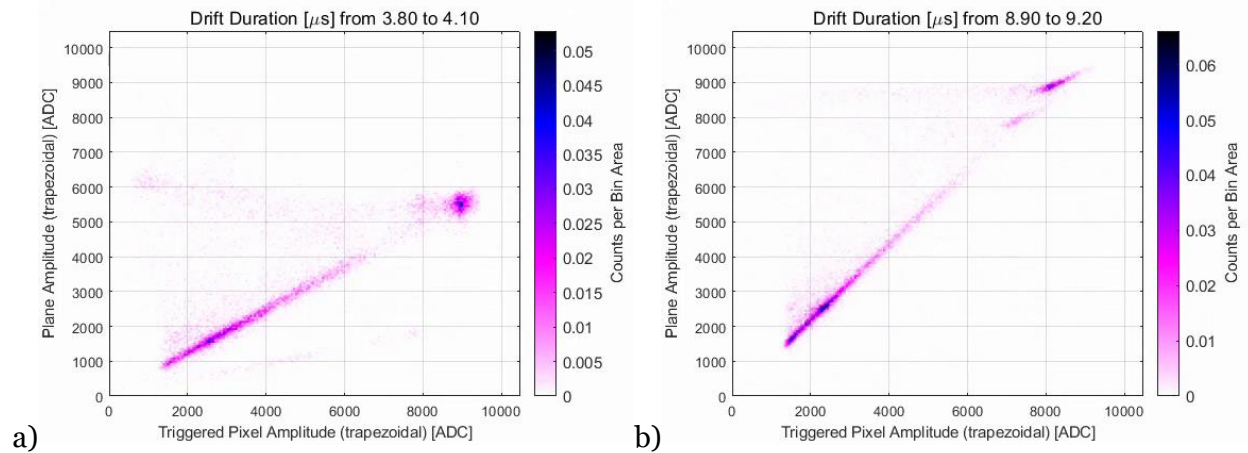


Figure 4.25. Bivariate histograms showing relations between plane amplitude and pixel amplitude for the events shown in Figure 4.24.

4.2.6 Subpixel Variations

Data from 171BS5-2(R) was analyzed using the subpixel-position reconstruction technique of opposing-neighbor ratios (ONR) [33]. Only the subpixel positions of the center pixel of this 3x3-pixel array were reconstructed because the technique requires neighbor-pixel waveforms. Depth-gain curves were observed to vary across the subpixel positions and the distributions of partial energy depositions changed across the subpixel positions. This may be because the ONR is biased by charge leakage but is likely because charge leakage actually varies as a function of subpixel position due to a lateral electric field. The presence of a lateral field is further supported by an asymmetry in single-pixel counts recorded at positive ONR and negative ONR, visible in Figure 4.26. See Section 4.2.3 on binary distributions in TlBr for more information on low-single-pixel-count regions. Low-SP regions in subpixel regions may also be caused by the immigration of events from one subpixel position to another due to a lateral electric field component (observed in another detector, 935-38AS3, reported in Section 7.1.2).

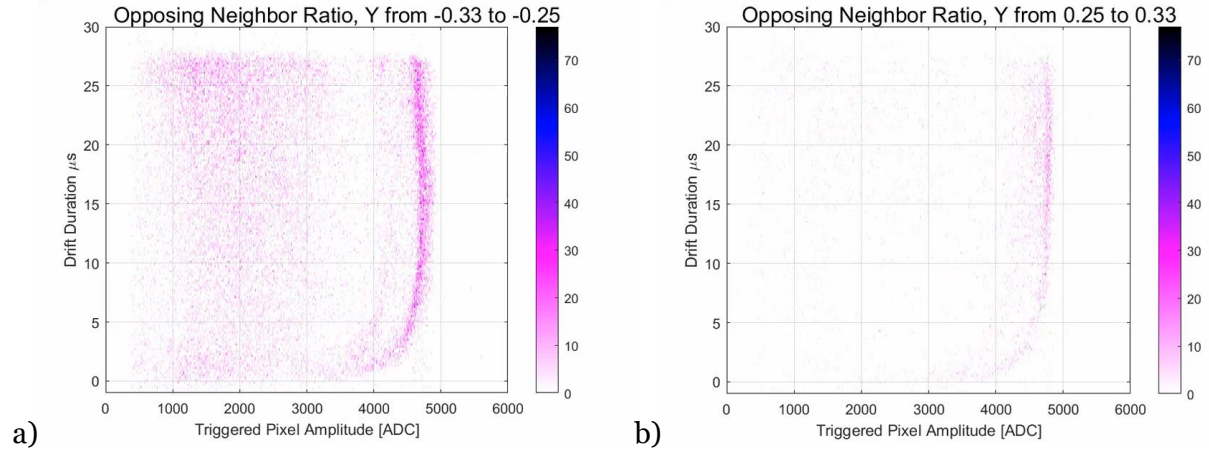


Figure 4.26. Bivariate histograms showing depth-separated energy spectra for 171BS5-2(R) given different subpixel slices equidistant from the center of the pixel. Color scale shows counts per bin area.

4.2.7 Inter-pixel Shorting in ASIC Systems

Errors in flip-chip bonding of 11×11-pixel TlBr detectors sometimes resulted in low resistances between neighboring pixels, verified by ohmmeter measurements. An easy method to identify pixels with low resistances between them was discovered using an ASIC-based readout system.

The nominal feedback resistance of the anodes' integrating charge preamplifiers in the ASIC is 10 k Ω according to the ASIC manufacturer's datasheets, though it can be

varied to fit the device under test. This means that charge integrated on a pixel's preamplifier may discharge significantly through an e.g., 12-k Ω path into another pixel's preamplifier.

Preamplifier inputs were connected through varying resistors (11.6 Ω , 120.7 Ω , 12.07 k Ω , and 1.01 M Ω) to recreate the effects of different low-resistance paths between pixels. Cell calibrations were performed, and signatures of low-resistance paths were documented, shown in Figure 4.27–Figure 4.31. Cell calibrations measure the baselines of the cells within the circular buffer which hold waveform samples; they are generally the first hardware operation performed after installing a new crystal, and can be performed before biasing, so cell calibrations offer a convenient opportunity to test for low-resistance paths between pixels. A thorough explanation of the differences between these signatures has not been developed.

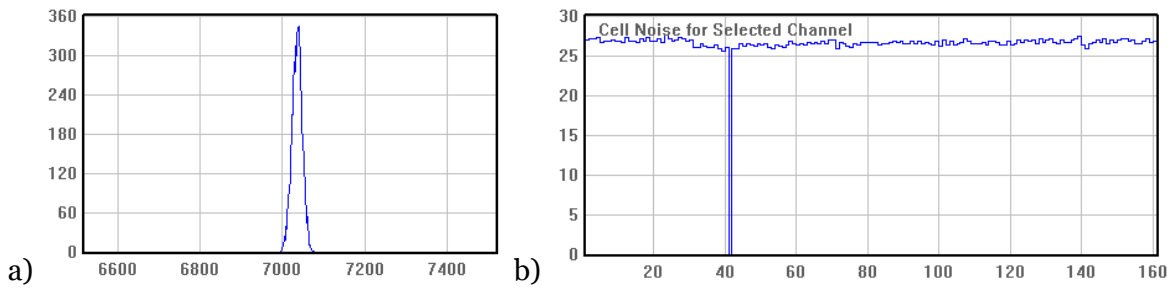


Figure 4.27. Cell calibration of a typical channel without low-resistance paths to other channels.
a) a cell's response to a pulser. b) "FWHM of cells' responses to pulser" vs. "cell index".

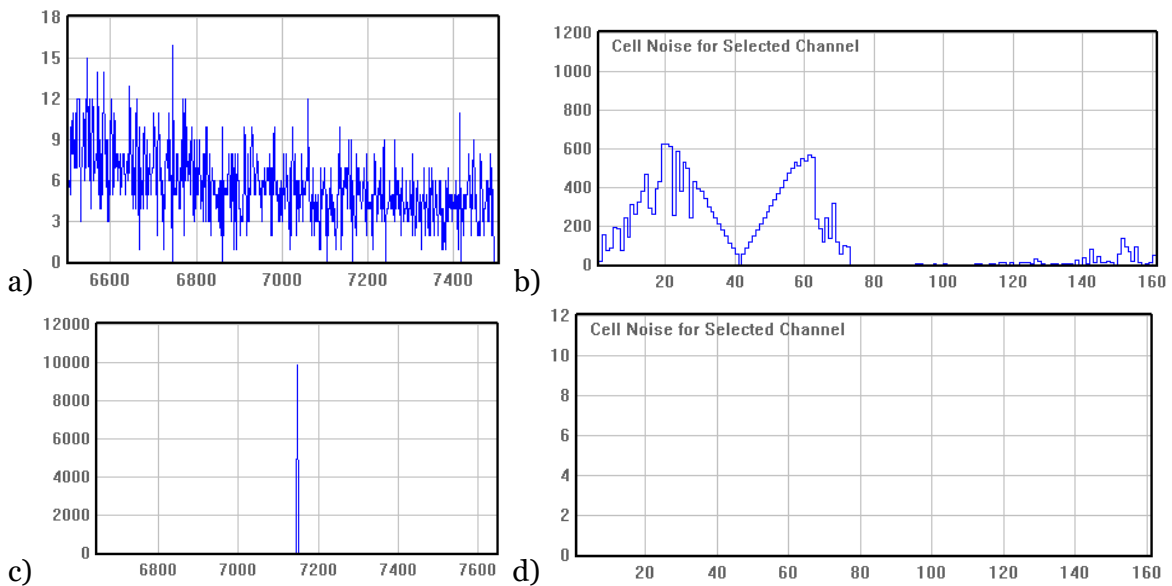


Figure 4.28. a-b) Cell calibration of one channel with a $11.6\ \Omega$ resistance path to another channel. c-d) Cell calibration of the connected channel.

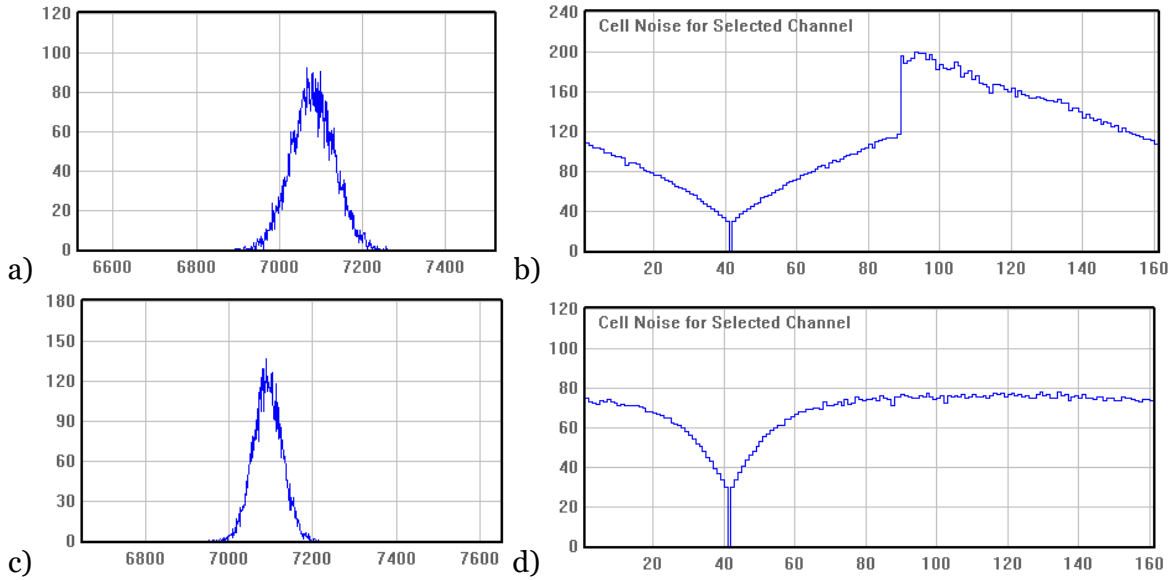


Figure 4.29. a-b) Cell calibration of one channel with a $120.7\ \Omega$ resistance path to another channel. c-d) Cell calibration of the connected channel.

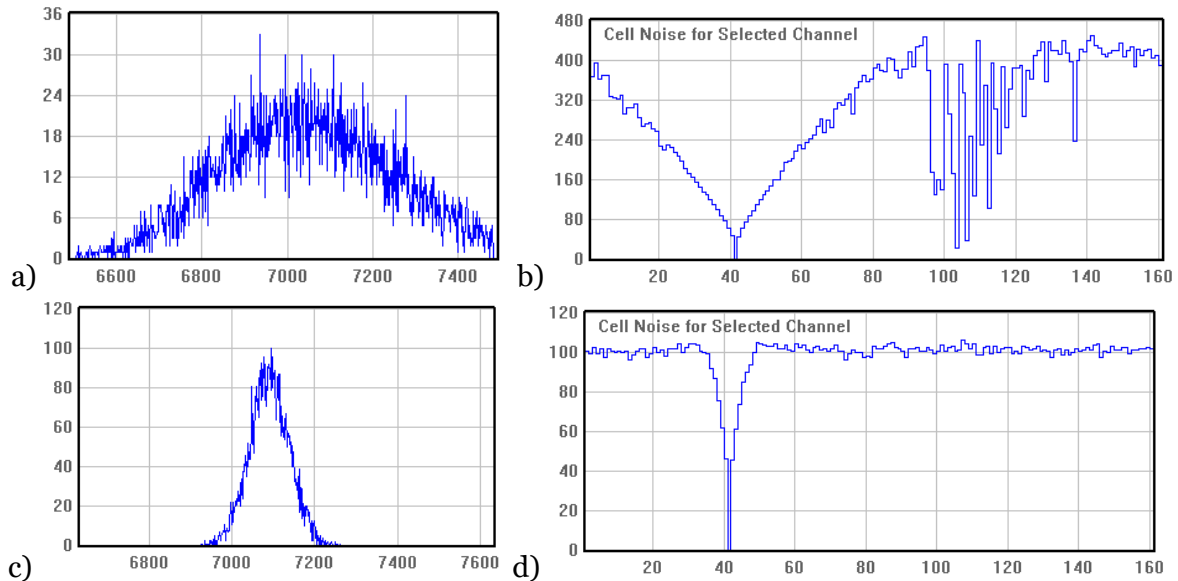


Figure 4.30. a-b) Cell calibration of one channel with a $12.07\ \text{k}\Omega$ resistance path to another channel. c-d) Cell calibration of the connected channel.

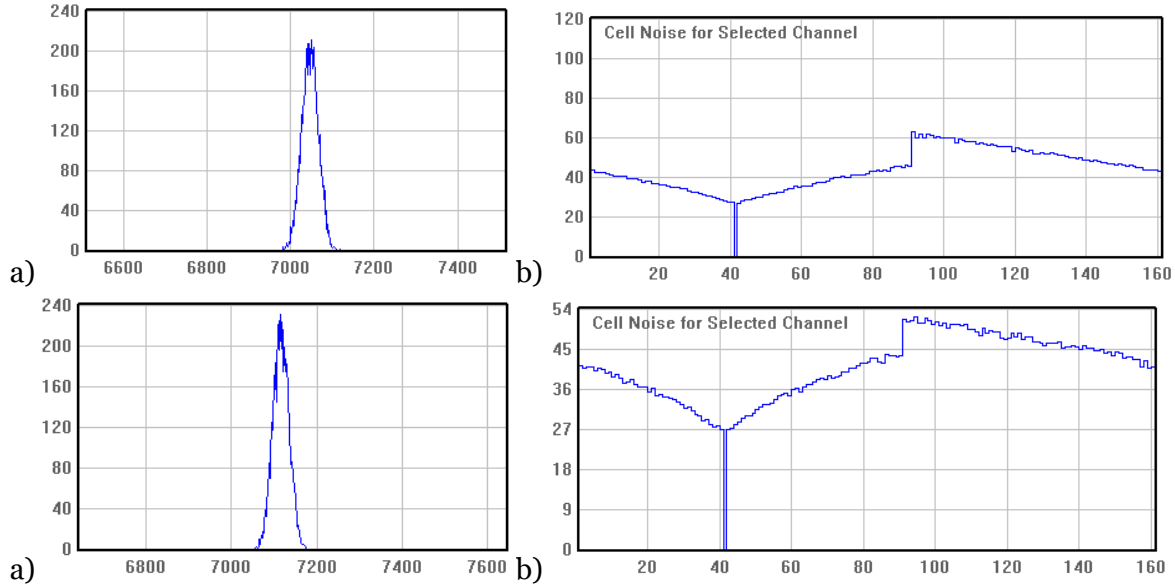


Figure 4.31. a-b) Cell calibration of one channel with a 1.01 MΩ resistance path to another channel. c-d) Cell calibration of the connected channel.

Cell calibrations of samples 150B2 and 150B3 were visually compared to these signatures, shown in Table 4.2. 120 Ω and 1 MΩ signatures were distinguished by average cell noise. Many pixels of 150B3 match these signatures, evidencing low-resistance paths which can only be fixed by refabrication.

Table 4.2 Low resistance paths found between pixels of two flip-chip-bonded crystals.

Crystal	12 Ω matches	120 Ω matches	12 kΩ matches	1 MΩ matches
150B2	2	0	0	0
150B3	2	5	7	22

4.2.8 Electrical Treeing

150BA4 was unique in that it was fabricated with a guard ring around the planar cathode. It was HCl-etched and manufactured with platinum contacts. It showed 3% FWHM at 662 keV for all single-pixel events self-calibrated and 2.3% best-pixel. Large frequent spurious current spikes through all electrodes were noticed after nearly six days of operation at -2000 V, so operation was halted. Electrical treeing and some discoloration were observed along the surface of the crystal upon inspection, shown in Figure 4.32.

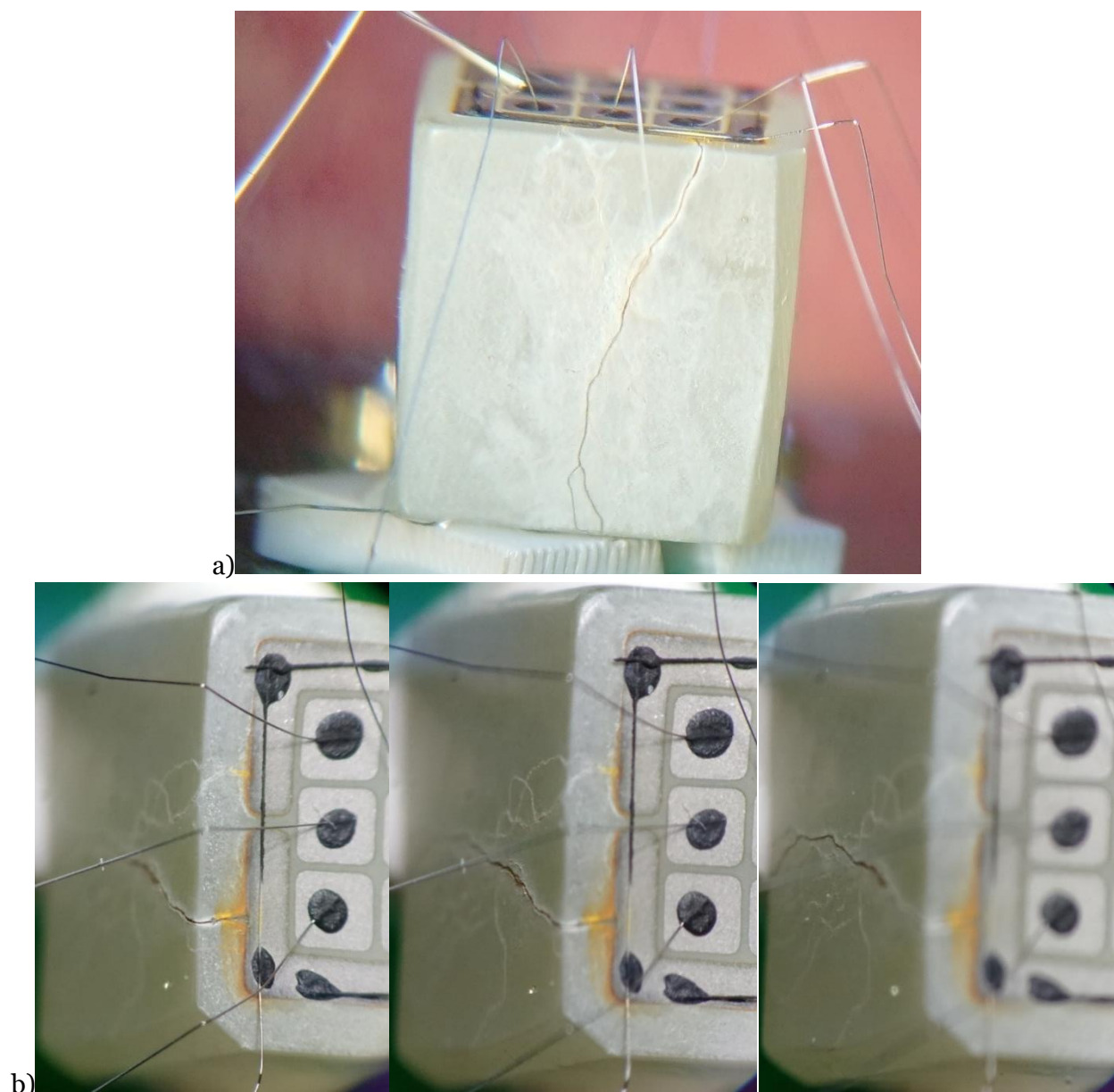


Figure 4.32. a) A photo from the side and b) a series of photos with different focal lengths of TLBr crystal 150BA4 showing the electrical tree which developed during extended high bias.

This electrical tree is visually similar but not identical to dendrite or fern formation previously observed in TLBr [37]. Perhaps this is pyrolysis caused by continued high bias after the formation of a dendrite which reacted with the air or surface layer to form a low resistance path. It was not known for how long the high current had been present.

150BA4 showed 5.6% all single-pixel and 3.7% best-pixel FWHM at 662 keV after the formation of the electrical tree, which may be incidental if caused by bulk changes,

and experienced intermittent baseline instability at -1000 V, significantly reducing its potential operating voltages. Electrical treeing was not observed in any other crystals.

Chapter 5 Ambipolar Pixel Sensitivity

5.1 Simulation

5.1.1 *Signal Induction*

To demonstrate the variety of waveform shapes, theoretical waveforms were generated for events at different depths and for different electron-hole mobility ratios assuming a 5-mm-thick TlBr detector with no charge trapping—the planar electrode of which is biased to -1000 V—and given a 51.2 μs sampling window centered on the electron collection times. The simulated waveforms are shown in Figure 5.1. This sampling window is typical for experiments performed at the University of Michigan on TlBr detectors. If another material is being considered, such as a slower halide perovskite which is positively biased, the timescale will slow and the waveform polarities will flip, but the shapes will remain the same, thus the role of “electron” and “hole” hereafter can be reversed if holes are the higher-mobility carrier and are collected by the pixel electrode.

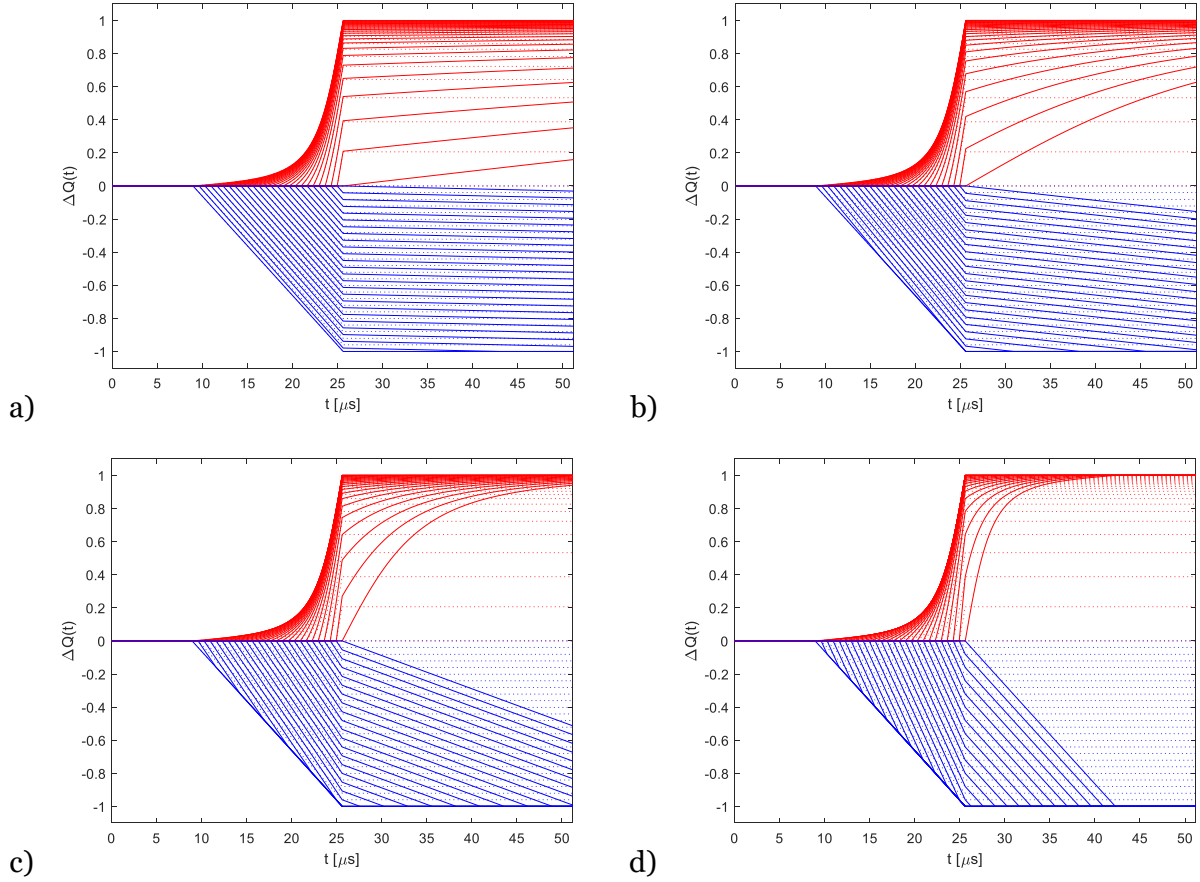


Figure 5.1. Theoretical pixel- (red) and plane- (blue) electrode pulse waveform pairs for events at depths throughout the detector for material with an electron-hole mobility ratio of a) 50, b) 10, c) 3, and d) 1. Dotted lines show final amplitudes excluding hole signal.

Pulse waveform pairs shown in Figure 5.1a-d exhibit different waveform amplitudes at the moment of electron collection at $t = 26 \mu s$ dependent on the depth of interaction which was used to generate them. At $t = 26 \mu s$, the amplitude of the pixel waveforms (red) is the same for most depths, and the amplitude of the plane waveforms (blue) is linearly related to depth for most depths. For the purpose of this work, the key variation between the responses from detectors with different electron-hole mobility ratios is the shape of the pixel waveform beginning at the time of electron collection. Figure 5.1a displays pixel waveforms in which the amplitude at the moment of electron collection is easy to determine because of a distinct point of inflection, but the amplitude after electron collection does not change significantly within the sampling window. Conversely, Figure 5.1d displays pixel waveforms in which there is significant change in

amplitude after electron collection for near-pixel depths of interaction, but the amplitude at the moment of electron collection for these waveforms is difficult to determine.

The additional signal induced by holes on the planar electrode increases the amplitude of the planar signal by a constant amount except when holes are collected within the sampling window. This increase in amplitude causes an overestimate of the depth of interaction by the plane-pixel ratio and can be fitted and removed if necessary [11]. The additional signal induced by holes on the pixel electrode benefits performance by restoring the gain deficit caused by the near-pixel weighting potential gradient, thus it does not systematically distort the plane-pixel ratio, but spatial variations in hole mobility-lifetime product may degrade depth resolution if hole signal is significant.⁴

The additional signal induced by holes does not affect the planar signal start time, but it may reduce the precision of and systematically increase the pixel stop time for very near-pixel events in materials whose electron-hole mobility ratios approach unity.

5.1.2 Novel Depth Parameter

Pixel electrode's pulse waveform shapes shown in Figure 5.1 exhibit dependence on interaction depth, especially for near-pixel interactions. These exhibit a fast rise, either linear or slightly concave, due to ambipolar motion followed by a slower convex rise due to hole motion. Assuming no charge trapping, ideal preamplifiers, and an infinite collection window, the waveform amplitudes at the moment of electron collection, A_{prompt} , and at the moment all charge is collected, A_{final} , and their ratio can be derived using the Shockley-Ramo theorem with the pixel weighting potential from Figure 1.1.

$$A_{prompt} \propto -q \left[1 - \phi_{w,pixel} \left(x_0 \cdot \left(1 + \frac{\mu_h}{\mu_e} \right) \right) \right] \quad \text{Equation 5.1}$$

$$A_{final} \propto -q \quad \text{Equation 5.2}$$

$$\frac{A_{prompt}}{A_{final}} = 1 - \phi_{w,pixel} \left(x_0 \cdot \left(1 + \frac{\mu_h}{\mu_e} \right) \right) \quad \text{Equation 5.3}$$

⁴ This additional signal will cause some low amplitude events to pass experimental thresholds which they otherwise would not have, mitigating the weighting potential dead region present in unipolar-sensitive pixelated detectors.

If the waveform amplitude at the inflection between these two rises can be measured, then the ratio of this prompt amplitude to the final amplitude yields a parameter which is strongly dependent on interaction depth for interactions near the pixel. The dependence on the electron-hole mobility ratio means that the prompt-final ratio has a greater depth sensitivity for detectors with more equivalent mobilities if the inflection time is known, but in practice, equal electron and hole mobilities cause a weak inflection which is difficult to pick off, as in Figure 5.1d. On the other extreme, great disparity in mobilities will allow easier inflection pickoff, but may restrict hole signal within the sampling window, reducing the measured final amplitude, as in Figure 5.1a, reducing its signal-to-noise ratio in practice. An intermediate electron-hole mobility ratio of between about three and ten (Figure 5.1b-c) is therefore desirable. The predicted relation between the prompt-final ratio and interaction depth was simulated using waveforms like those shown in Figure 5.1 and is shown in Figure 5.2.

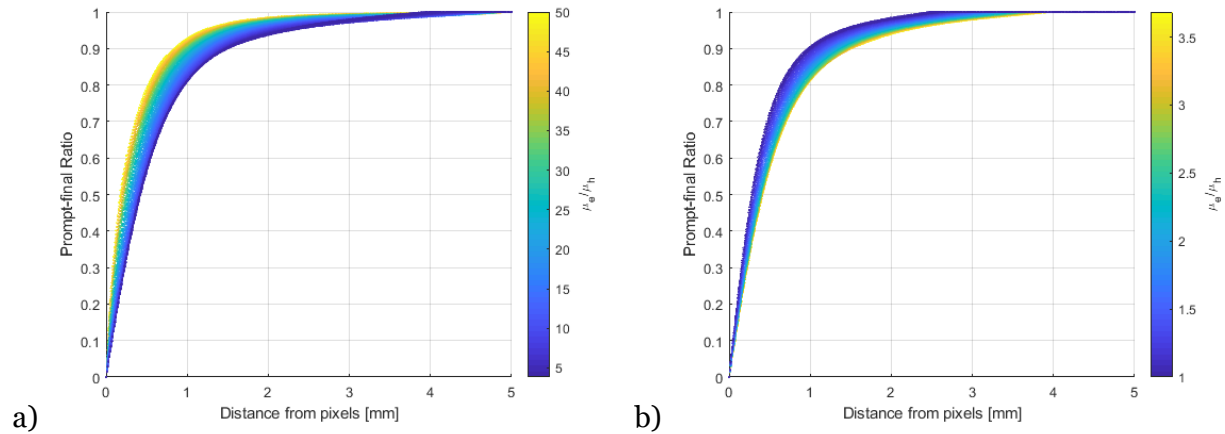


Figure 5.2. Relations between the new depth parameter and depth of interaction from simulated waveforms given a) high and b) low electron-hole mobility ratios and assuming electron collection time is known.

5.2 Experimental Validation

5.2.1 Signal Induction

A 5-mm-thick TlBr crystal with 3×3 1-mm-pitch pixels (crystal 139BS3-1(R)) was biased to -1000 V and flood irradiated with Cs-137 gamma rays. The responses were recorded as described in Chapter 2. Because of pixel-to-pixel variance within the device, results are only shown for the best performing pixel.

Experimental waveforms were observed which match the simulated waveforms shown in Figure 5.1. Figure 5.3a shows example photopeak pulse waveforms from interaction depths near the planar electrode in which both electrons and holes were collected within the sampling window because of high hole mobility. Figure 5.3b shows example photopeak pulse waveforms from interaction depths very near the collecting pixel electrode showing hole-induced signal component on the pixel and plane electrodes.

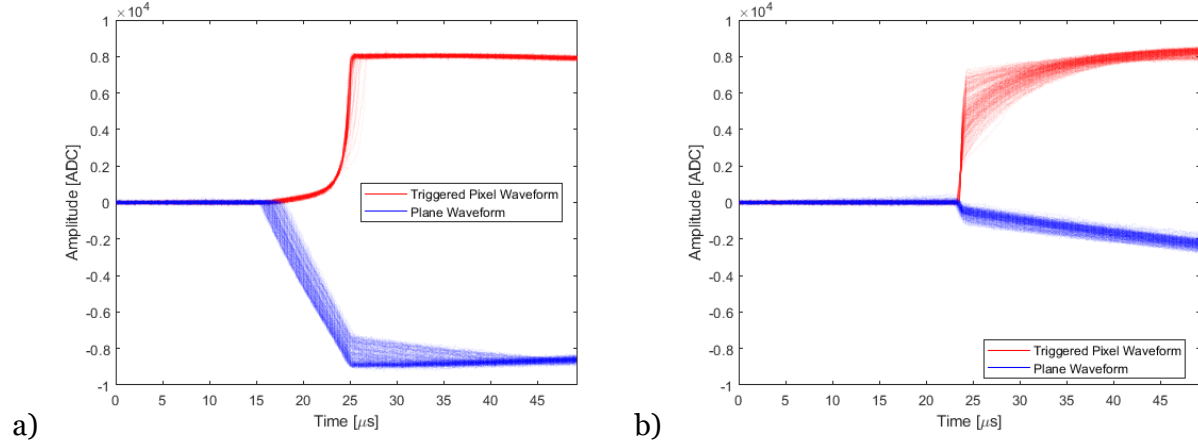


Figure 5.3. 200 typical pairs of photopeak pulse waveforms showing hole induced signal from interactions which occurred a) near the planar electrode and b) near the pixel electrode. Cf. Fig. 2b.

5.2.2 Novel Depth Parameter

Waveform inflections with physical significance—the time of gamma-ray interaction and the time of electron collection—were identified using digital CR-(RC)ⁿ shapers and constant fraction thresholds tuned to the dataset. Prompt amplitude was found using prompt subtraction [30] and final amplitude was found using trapezoidal filtering to calculate the prompt-final ratio.

The experimental relation between prompt-final ratio and drift duration shown in Figure 5.4 validated the simulated relation shown in Figure 5.2.

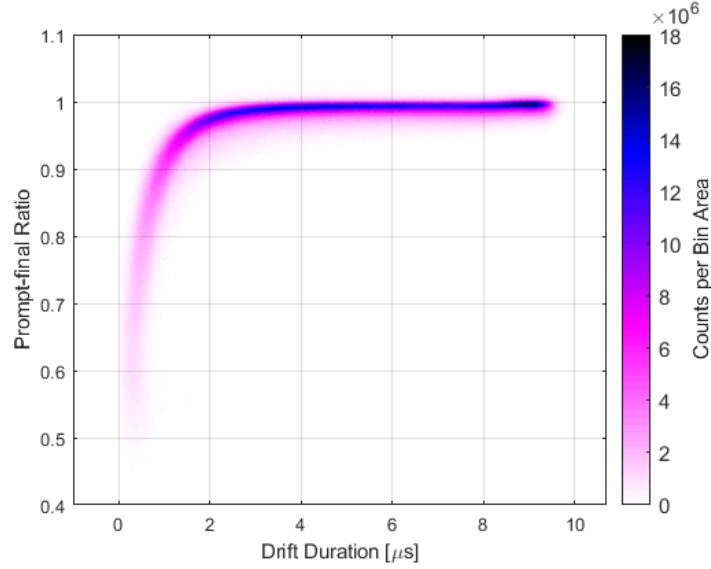


Figure 5.4. Prompt-final ratio versus drift duration for all single-pixel Cs-137 gamma-ray interactions in ambipolar-sensitive TlBr. Cf. Figure 5.2.

The relation between photopeak centroid and prompt-final ratio was found for interaction depths within a pixel pitch of the pixel surface. The interaction depth was determined by the drift durations. This relation was used to self-calibrate the energy spectrum. Next, the relation between photopeak centroid and drift duration was found and used to self-calibrate the energy spectrum. “Self-calibration” herein means that the calibration was applied to the same data from which it was generated. Figure 5.5 compares the relations between waveform amplitude and both plane-pixel ratio and prompt-final ratio, for events with interaction depths within a pixel-pitch of the pixel surface as determined by the drift duration. The top band of events in Figure 5.5b are the photopeaks used for calibration. Narrower photopeaks are visible for low prompt-final-ratio values in Figure 5.5b than those for low plane-pixel-ratio values in Figure 5.5a. Figure 5.6 shows the result of the prompt-final-ratio calibration on the relation between waveform amplitude and drift duration. More uniform photopeak positions are visible near pixel.

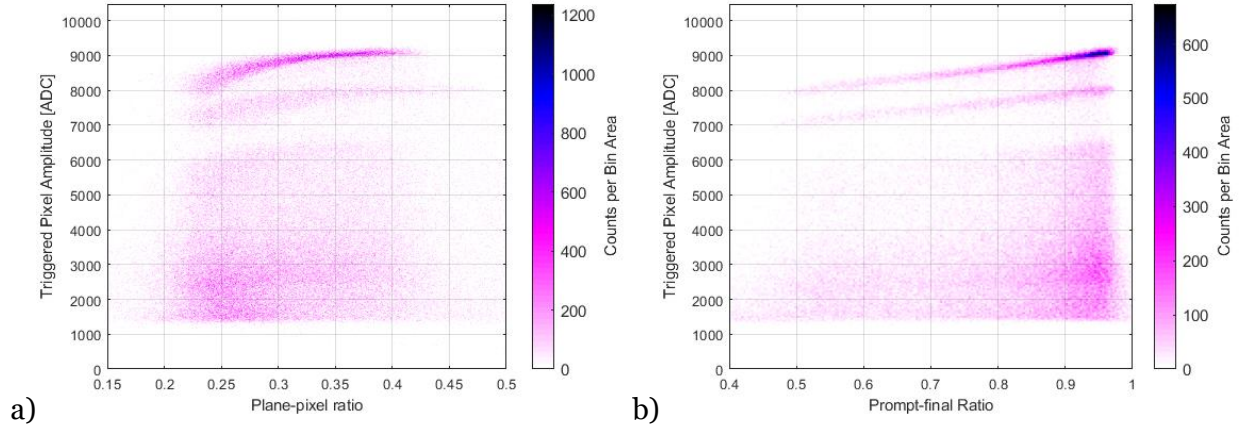


Figure 5.5. Waveform amplitude versus a) plane-pixel ratio and b) prompt-final ratio for Cs-137 gamma-ray interactions within a pixel pitch of the pixel surface as determined by the drift duration.

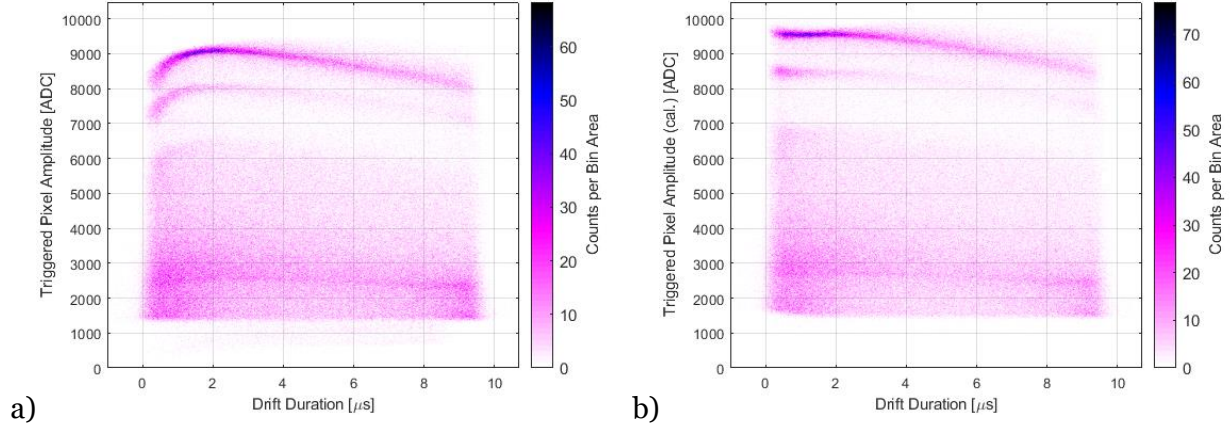


Figure 5.6. Waveform amplitude vs. drift duration a) before and b) after calibration using prompt-final ratio.

The additional calibration only improved performance. Figure 5.7 shows the energy spectra with and without calibrations yielding the energy resolutions listed in Table 1. The addition of the prompt-final-ratio calibration improved the FWHM at 662 keV by between 16% and 21% (3-4 keV). The improvement in resolution is significant because charge from near-pixel events drifts for only a short duration and experiences little trapping and because the fraction of events which lie near-pixel is appreciable (roughly equivalent to the pitch-thickness ratio, which is one fifth here).

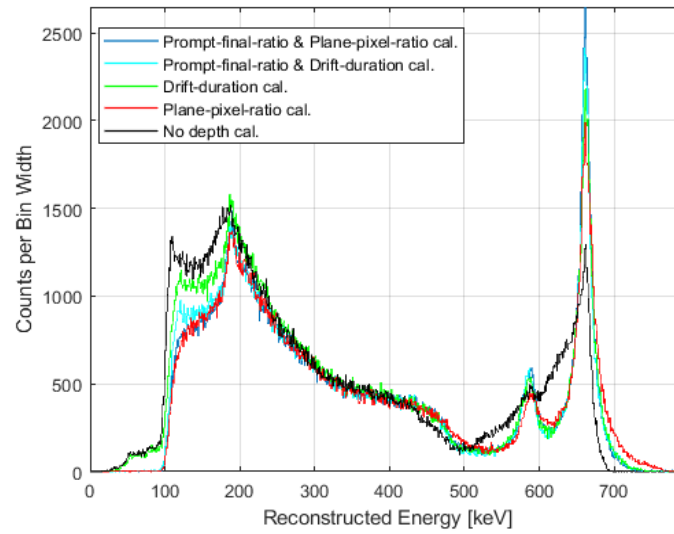


Figure 5.7. Cs-137 energy spectra measured by ambipolar-sensitive TlBr self-calibrated using the methods discussed.

Table 5.1. Energy resolutions from different calibrations.

Self-calibration Method	FWHM at 662 keV
None	3.93%
Plane-pixel ratio	2.73%
Drift-duration	2.52%
Prompt-final ratio then plane-pixel ratio	2.14%
Prompt-final ratio then drift duration	2.10%

Chapter 6 Treating Incomplete Charge Collection

6.1 Methods of Identification

Two methods of identifying ICC in hole-mobile semiconductors were developed and applied to the responses of pixelated TlBr detectors to flood irradiations of Cs-137 gamma rays. The first method compares charge reconstructed using different signals and the second method compares depths of interaction reconstructed using different signals. Pixel signal induction by charge which becomes trapped (e.g. [38]) was not included in the models used in these methods, but trapped plane signal was.

6.1.1 Comparing Charge Reconstructions

The first ICC-identification method starts as follows. The charge freed in each event is estimated from the amplitude of the pixel signal, A_{pixel} , yielding the pixel reconstruction,

$$\langle q \rangle_{pixel} = A_{pixel} \quad \text{Equation 6.1}$$

The drift distance of the freed electrons for each event, d_e , is found by measuring the drift durations of each event using the start time from the plane signal and the stop time from the pixel signal and assuming a constant drift velocity. The charge freed in each event is again estimated by dividing the amplitude of the plane signal, A_{plane} , by the fraction of the crystal thickness through which the charge drifted, (the electron drift distance d_e divided by the crystal thickness D), since the plane amplitude is proportional to the distance drifted [8], yielding the plane reconstruction

$$\langle q \rangle_{plane} = A_{plane} \frac{D}{d_e} \quad \text{Equation 6.2}$$

These two reconstructions theoretically agree for events which have complete charge collection and no hole-induced signal and which are not within the nonlinear weighting potential near the pixel electrode surface [9].

To account for hole-induced signal due to high hole mobility, the plane signal was derived analytically from the typical charge trapping model and the Shockley-Ramo

theorem [8] presented in Section 1.1 assuming homogeneous material properties, a linear weighting potential, and negligible detrapping yields the charge induced on the planar electrode as a function of time, yielding

$$\Delta Q_{plane}(t) = \Delta Q_e(t) + \Delta Q_h(t) \quad \text{Equation 6.3}$$

$$\Delta Q(t) = \int_{t'=0}^t \frac{dq(t')}{dt'} \cdot \phi_w(x(t')) dt' - q \left(1 - e^{-\frac{t}{\tau}} \right) \cdot \phi_w(x(t=0)) \quad \text{Equation 6.4}$$

$$\frac{dq(t')}{dt'} = \frac{d}{dt'} q e^{-\frac{t'}{\tau}} = -\frac{q}{\tau} e^{-\frac{t'}{\tau}} \quad \text{Equation 6.5}$$

$$\Delta Q(t) = \int_{t'=0}^t -\frac{q}{\tau} e^{-\frac{t'}{\tau}} \cdot \phi_w(x(t')) dt' - q \left(1 - e^{-\frac{t}{\tau}} \right) \cdot \phi_w(x(t=0)) \quad \text{Equation 6.6}$$

$$\Delta Q(t) = \int_{t'=0}^t -\frac{q}{\tau} e^{-\frac{t'}{\tau}} \cdot \left(1 - \frac{x_0 + \mu E t'}{D} \right) dt' - q \left(1 - e^{-\frac{t}{\tau}} \right) \left(1 - \frac{x_0}{D} \right) \quad \text{Equation 6.7}$$

Evaluating the integral and including charge collection times,

$$\begin{aligned} \Delta Q_e(t) &= \begin{cases} \frac{q\mu_e E t}{D} e^{-\frac{t}{\tau_e}} + \frac{q}{D} \left((\mu\tau)_e E + d_e - D - e^{-\frac{t}{\tau_e}} (\mu_e E (\tau_e + t) + d_e - D) \right), & 0 \leq t \leq \frac{d_e}{\mu_e E} \\ \frac{q d_e}{D} e^{-\frac{d_e}{(\mu\tau)_e E}} + \frac{q}{D} \left((\mu\tau)_e E + d_e - D - e^{-\frac{d_e}{(\mu\tau)_e E}} (\mu\tau_e E + 2d_e - D) \right), & t > \frac{d_e}{\mu_e E} \end{cases} \end{aligned} \quad \text{Equation 6.8}$$

$$\begin{aligned} \Delta Q_h(t) &= \begin{cases} \frac{q\mu_h E t}{D} e^{-\frac{t}{\tau_h}} + \frac{q}{D} \left((\mu\tau)_h E + d_e - D - e^{-\frac{t}{\tau_h}} (\mu_h E (\tau_h + t) + d_e - D) \right), & 0 \leq t \leq \frac{D - d_e}{\mu_h E} \\ q \left(1 - \frac{d_e}{D} \right) e^{-\frac{D - d_e}{(\mu\tau)_h E}} + \frac{q}{D} \left((\mu\tau)_h E + d_e - D - e^{-\frac{D - d_e}{(\mu\tau)_h E}} ((\mu\tau)_h E) \right), & t > \frac{D - d_e}{\mu_h E} \end{cases} \end{aligned} \quad \text{Equation 6.9}$$

where d_e is the electron drift distance, D is the detector thickness, E is the electric field, q is the charge freed by the gamma-ray interaction (assumed to be unity for the simulation), and μ and τ are the mobility and lifetime of either electrons or holes, denoted by subscript.

Discontinuities exist at the moments of charge collection, after which the charge induced does not change. Assuming an ideal preamplifier, the induced charge is

proportional to the preamplifier output. In practice, the preamplifier output is digitized into 512 samples at a sampling frequency of 5 MHz (a 102.4 μs window), with the electron collection time roughly centered in the window. Waveforms were simulated using Equation 6.3, Equation 6.8, and Equation 6.9 with the values in Table 6.1. The waveforms were aligned by electron collection time, truncated to match the experimental digitization window (shown in Figure 6.1), and their maximum amplitudes and drift distances were recorded to employ Equation 6.2. Figure 6.2 shows the reconstructed charge using Equation 6.2 from simulated waveforms like that shown in Figure 6.1.

Table 6.1. Values used to simulate waveforms.

Symbol	Value	Unit
q	1	unit charge
τ_e	3×10^{-4}	s
τ_h	3×10^{-5}	s
μ_e	30	cm^2/Vs
μ_h	3	cm^2/Vs
E	1000	V/cm
D	1	cm
d_e	0 to D	cm

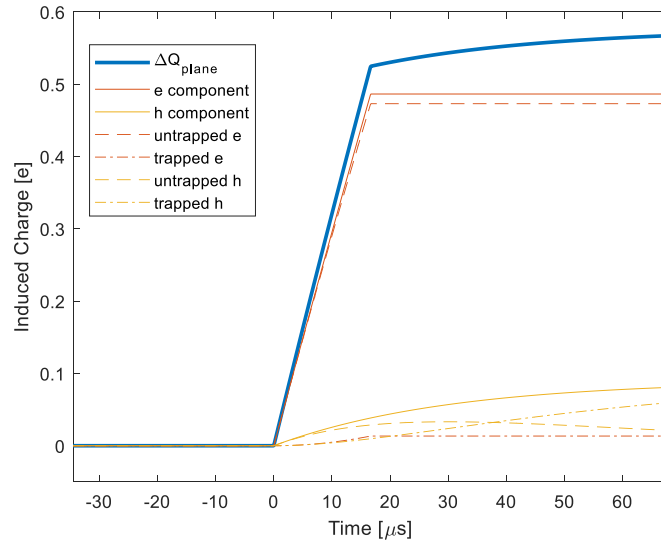


Figure 6.1. Simulated planar waveform in blue from an event which occurred at half the thickness of the detector. Components of the waveform from electron and hole motion are shown in orange and yellow.

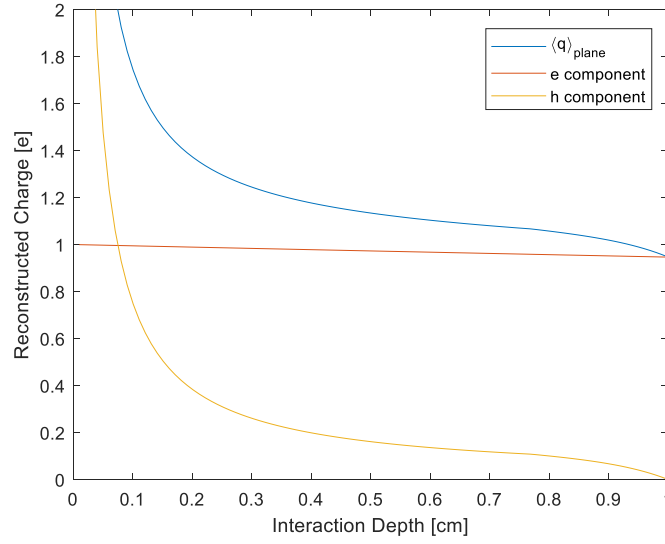


Figure 6.2. Reconstruction of a unit charge from simulated waveforms from all depths of interaction (where 0 is the pixel-electrode surface) showing electron and hole components.

The maximum plane amplitude can be approximated from Figure 6.2 as

$$A_{plane} = q \frac{d_e}{D} + q \frac{d_h}{D} \quad \text{Equation 6.10}$$

where d_h is the effective drift distance of the holes, equal to the maximum of Equation 6.9 during the digitization window if electron trapping is negligible. Equation 6.2 and Equation 6.10 can be combined to isolate the distortion of the plane reconstruction by the hole signal,

$$\langle q \rangle_{plane} = q + q \frac{d_h}{d_e} \quad \text{Equation 6.11}$$

Collection of the holes is not observed at most depths because of the short sampling window, but most holes become trapped by the end of the sampling window at most depths anyway due to a low hole lifetime. These deficits restrict d_h to a small nearly constant value regardless of interaction depth, thus the hole distortion is proportional to $1/d_e$, shown in Figure 6.2. Ballistic deficit from too fast a shaping filter can also reduce the effective hole drift distance.⁵

⁵ Holes are collected for events near the cathode, reducing the hole distortion.

After the plane reconstructions of the freed charges for each event are calculated, the values of q and qd_h from Equation 6.11 can be fit from the plane reconstruction vs. depth of interaction, as in Figure 6.2; their ratio yields d_h (equal to 0.083 cm for this simulation).⁶

Combining Equation 6.2 and Equation 6.11 and solving for q gives the informed plane reconstruction making use of d_h ,

$$\langle q \rangle'_{plane} = \frac{A_{plane}}{d_e/D} \left(1 + \frac{d_h}{d_e} \right)^{-1} \quad \text{Equation 6.12}$$

where A_{plane} and d_e are event-specific values, d_h is an experiment-specific constant, and D is the thickness of the crystal.

The new plane reconstruction should be unaffected by hole signal, thus it should be equal to the pixel reconstruction except for events which suffer incomplete charge collection or events which occur near the pixel (a small fraction of the total active volume). The ratio between the pixel reconstruction and the informed plane reconstruction is calculated for each event,

$$f = \frac{\langle q \rangle_{pixel}}{\langle q \rangle'_{plane}} \quad \text{Equation 6.13}$$

It is intuitively the fraction of freed charge collected by the triggered pixel for events suffering from severe charge trapping or charge leakage. For multi-interaction events, f is nonphysical. f is then used to screen events for ICC: a window of acceptance around $f \approx 1$ is set and events with f outside the window are removed from the final energy spectrum created ordinarily by depth-calibrating the pixel reconstruction [9].

If the type of ICC is known for each event and if the amplitude of the plane signal, the depth of interaction from drift duration, and d_h/d_e are measured with high precision, the informed plane reconstruction from Equation 6.12 should be taken as the true freed charge instead of the pixel reconstruction for events experiencing charge leakage. In practice, the type of ICC is not usually known, and the plane reconstruction is much noisier than the pixel reconstruction, so it is most practical to simply screen ICC events.

⁶ d_h will always be less than the product of $\mu_h E$ and the sampling duration after the interaction time (68 μs in Figure 6.1) because of charge trapping ($\mu_h E \cdot 68 \mu s = 0.21 \text{ cm}$ in the simulated example).

6.1.2 Comparing Depth Reconstructions

The second ICC-identification method starts as follows. The drift distance of the freed electrons for each event is found by measuring the drift durations of each event as in the first method, then is divided by the detector thickness to give the unitless depth reconstructed from timings, the time reconstruction,

$$\langle d_e/D \rangle_{time}$$

Next, the unitless depth reconstruction is found by dividing the amplitude of the plane signal by the amplitude of the pixel signal (conventionally the cathode-anode ratio, CAR) [8], the CAR reconstruction,

$$\langle d_e/D \rangle_{CAR} = \frac{A_{plane}}{A_{pixel}} \quad \text{Equation 6.14}$$

These two reconstructions theoretically agree for events which have complete charge collection and no hole-induced signal, with a small deviation for events which occur near the pixel due to the pixel weighting-potential shape. Hole-induced pixel signal mitigates this deviation. Hole-induced plane signal causes a systematic increase in CAR reconstructions [35] proportional to d_h/d_e at all depths of interaction except near the planar electrode where holes are collected, as discussed in the previous section.

ICC will affect the CAR reconstruction in subtly different ways depending on the type of ICC. Charge trapping and charge leakage were simulated numerically using calculated weighting potentials and assuming uniform material properties. Charge which is trapped mid-drift because of a poor electron mobility-lifetime product or a weak electric field will induce insignificant charge on the pixel electrode but may induce significant charge on the planar electrode, increasing the CAR reconstruction as shown in Figure 6.3. Trapped charge was assumed to induce zero charge on the collecting pixel in the simulated model. Charge leakage decreases the induced charge on the pixel, also increasing the CAR reconstruction as shown in Figure 6.4.⁷ Multiple interactions at the same depth can be treated as charge leakage. Multiple interactions at different depths were not simulated but may increase or decrease the CAR reconstruction.

⁷ Some mechanism like diffusion will cause the fraction collected to be dependent on depth of interaction.

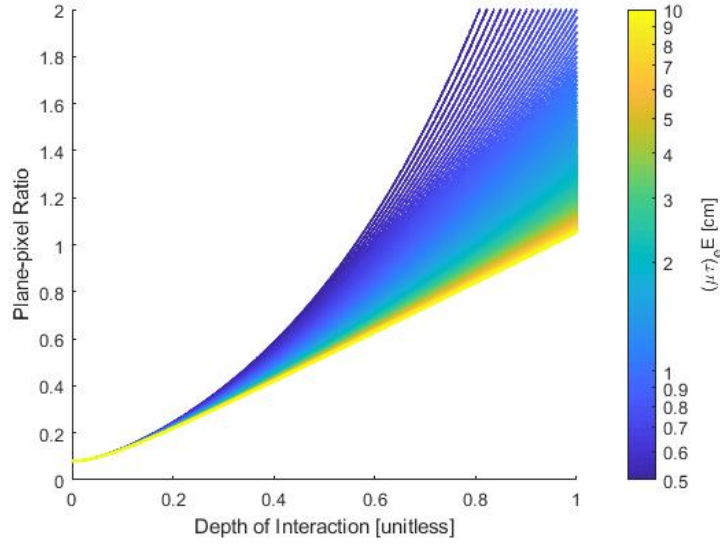


Figure 6.3. Simulated distortion of CAR reconstruction for different amounts of electron trapping.

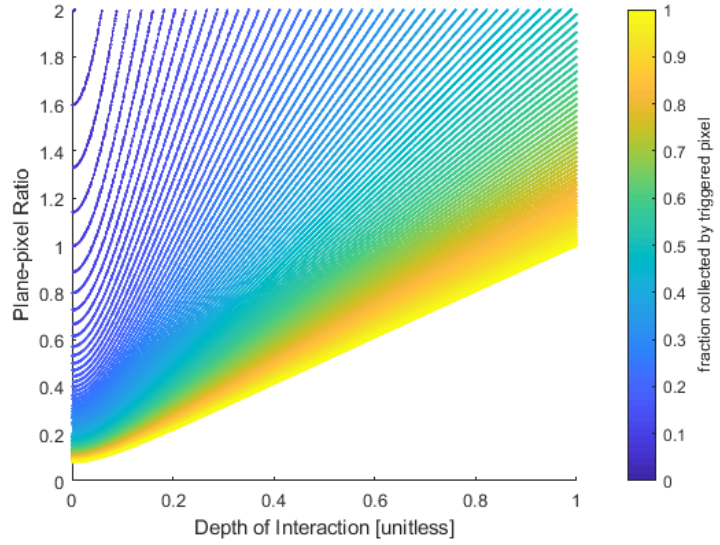


Figure 6.4. Simulated distortion of CAR reconstruction for different amounts of charge leakage.

Time reconstructions should not be affected by hole-motion nor ICC but may be affected by nonuniform drift velocities caused by space charge.

After the time reconstruction and CAR reconstruction have been calculated for all events, the relation between time reconstruction and CAR reconstruction is found from photopeak events. Photopeak events are chosen because they should not exhibit ICC. The relation should match one curve of Figure 6.3, with distortion from hole-motion as described if hole mobility is sufficiently high. It is not necessary that the corresponding $(\mu\tau)_e$ or fraction collected is identified. Boundaries around this curve are set according to

the uncertainty of the relation and events of any energy which lie outside of the boundaries are removed from the final energy spectrum created ordinarily by depth-calibrating the pixel reconstruction.

If the type of ICC is known for each event, if the CAR reconstruction and time reconstruction are measured with high precision, and if hole signal is negligible or removable, the $(\mu\tau)_e E$ or fraction collected can be calculated from the curves in Figure 6.3 and Figure 6.4 and the charge deficit due to charge trapping and charge leakage can be corrected. In practice, the type of ICC is not usually known, and hole signal is difficult to account for, so it is most practical to simply screen ICC events.

6.2 Experimental Results

The two techniques were applied to the responses of two TlBr detectors manufactured by Radiation Monitoring Devices, Inc. operated at room temperature. One detector, 171BS5-1(R), was 1-cm thick with 3×3 1.72-mm-pitch pixels and the other, 935-38AS3, was 5-mm thick with 11×11 1-mm-pitch pixels. Both detectors were flood irradiated with Cs-137 gamma rays. Detector responses were recorded using the methods described in Chapter 2. The results are presented in the following sections.

The reader is also encouraged to review the investigation presented in Section 4.2.5 which includes identification of and differentiation between different types of ICC.

6.2.1 Comparing Charge Reconstructions

A depth-calibrated energy spectrum was generated from the single-pixel response of the 3×3 -pixel TlBr detector.

The naïve plane reconstruction following Equation 6.2 yielded the distribution shown in Figure 6.5; the photopeak band of which resembles the distorted charge reconstruction predicted in Figure 6.2.

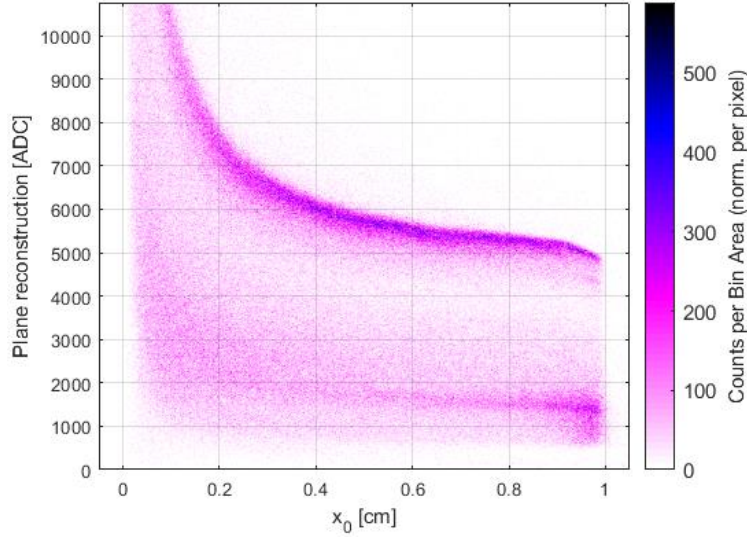


Figure 6.5. Charge freed under one TlBr pixel during Cs-137 flood irradiation reconstructed using the naïve method in Equation 6.2 plotted vs. interaction depth.

Values of q and qd_h from Equation 6.11 were fit from the curve formed by the photopeak centroids of Figure 6.5 and their ratio was taken, yielding $d_h = 0.12 \text{ cm}$, the effective drift distance of the holes before they were trapped or before they drifted out of the digitization window. In this crystal, d_h varied slightly between pixels because of a nonuniform $(\mu\tau)_h$, so only the results of one pixel are shown here. Equation 6.12 and Equation 6.13 were applied. The values of the energy deposited vs. f for each recorded event are shown in Figure 6.6. Full-energy events exhibiting charge sharing follow a diagonal band. Notably, most thallium x-ray-escape events fall in the diagonal band, evidencing that most thallium x rays do not leave the crystal. Screening thresholds shown as vertical lines in Figure 6.6 were applied and the resulting energy spectra are shown in Figure 6.7. The fraction of all events which comprised the photopeak (the photofraction) increased from 14% to 26% and the total counts in the photopeak (the photopeak efficiency) decreased 10% between the unscreened spectrum and the most heavily screened ($f > 0.95$) spectrum.

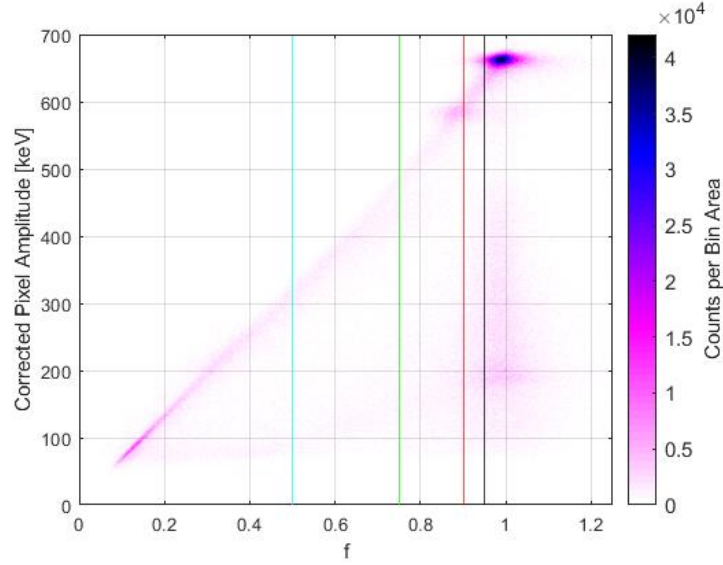


Figure 6.6. Energy deposited vs. f (Equation 6.13) for all events recorded by one pixel of a TlBr detector irradiated by Cs-137.

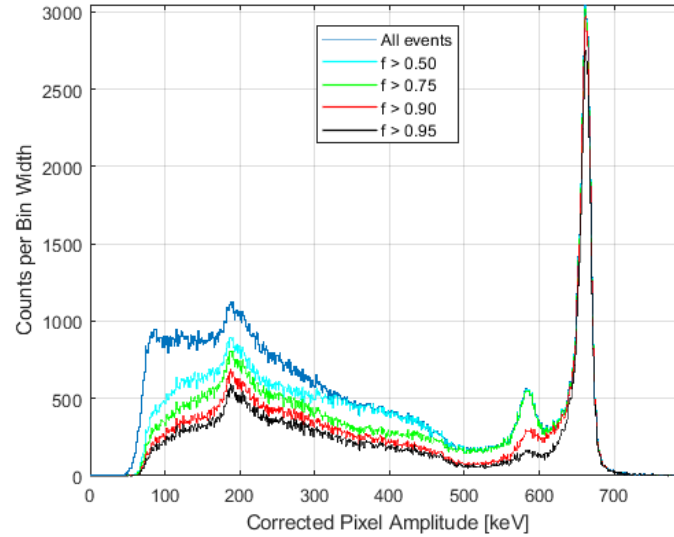


Figure 6.7. Energy spectra of Cs-137 gamma rays recorded by TlBr before and after screening events for ICC.

6.2.2 Comparing Depth Reconstructions

A detailed example of processing, including ICC screening by comparing depth-reconstructions, of 935-38AS3 is given in Section 3.3, and the results are given in Section 7.1.1. The highlight is that ICC-screening improved the best pixel's energy resolution at 662 keV from 1.5% to 1.4% and increased the photofraction from 16% to 29% while

decreasing the photopeak efficiency by 17% (likely due to misclassification of events which experienced complete charge collection).

6.3 Inferences on Hole Transport

The results just shown were from one pixel, but the fits to extract d_h were performed for all nine pixels and the results are shown in Table 6.2. Variation in the first and second parameter, q and qd_h , between pixels was expected because these parameters were affected by preamplifier gain, which varied between pixels. Their quotient, d_h , should not have been dependent on preamplifier gain, yet there was a large variance in d_h between pixels.

Table 6.2. Fit parameters for all pixels.

Pixel	q [ADC]	qd_h	d_h [cm]
1	4450	670	0.15
2	4550	1030	0.23
3	4200	550	0.13
4	4290	570	0.13
5	4260	560	0.13
6	4240	520	0.12
7	4180	530	0.13
8	4010	540	0.14
9	4110	530	0.13
Mean	4250	610	0.14
Rel. Std. Dev.	4%	27%	23%

The variation in d_h must have been due to a difference in μ_h , τ_h , or electric field profile between pixels. The variation was suspected to be limited to $(\mu\tau)_h$ because no significant difference in drift-duration distributions or single-pixel counts was observed between pixels which would have indicated a variation in electric field profile.

This lateral variation in d_h affects the depth reconstruction from plane-pixel ratio. There is likely a sub-pixel variation in d_h which reduces the precision of the plane-pixel ratio as a depth reconstruction.

Chapter 7 Best Performance

7.1 Performance of TlBr

TlBr detectors tested over the course of this work generally showed between 2.5% and 3.5% energy resolution or worse for all single-pixel events, self-calibrated, and best pixels sometimes approached 1.5%. The resolution observed was strongly affected by those time-dependent phenomena discussed in Chapter 4 and how much of their transience was integrated into the nominal resolution. The resolution was also affected by some settings such as the trigger thresholds; too low a threshold allowed noise triggers which increased electronic dead time, requiring longer measurements which integrated more transient behavior and degraded nominal resolution; too high a threshold hindered anticoincidence, misclassifying charge-shared events as single-pixel events which degraded observed resolution. Resolutions also varied with processing techniques because of the different ways in which anomalies discussed in Chapter 4 affected depth-calibrations. That is not to say experimental or processing settings were chosen incorrectly, but that unpredictability prevented settings from being optimized for each detector.

Most TlBr detectors recently tested at the University of Michigan have been 3×3 -pixel detectors since they offer higher yield and are easier to manufacture than flip-chip-bonded 11×11 -pixel detectors, but 3×3 -pixel detectors are only an intermediate step in the research and development process toward the goal of 11×11 -pixel deployable CZT sisters, thus the performance of larger 11×11 -pixel TlBr detectors is of greatest practical interest.

7.1.1 11×11 -pixel Detectors

11×11 -pixel detectors experienced pixel-to-pixel shorting (150B3) and low-count regions (150B2) as described in Sections 4.2.7 and 4.2.3, and experienced poor contact adhesion after flip-chip bonding which led to mechanical failure (150B4). Some experienced increasing leakage currents during operation, described in Section 4.2.1, which prevented further spectroscopic characterization (178BS3, 171A2).

935-38AS3 performed the best of the 11×11 -pixel detectors, so its response was studied in detail. It exhibited Auger recombination as described in Section 4.2.4, the extra charge from which was corrected for by calibrating near-plane signals using the prompt-final ratio (PFR, labeled “pfr” in Figure 7.1), detailed in Section 3.3.2. The PFR was also used to calibrate near-pixel signal deficit due to the weighting potential as it was intended to be used in Chapter 5. The application of these two depth-specific calibrations caused a mismatch in the relation between the photopeak centroid and depth which was corrected when self-calibrating with drift duration (“dur” in Figure 7.1).

A high trigger threshold was used during its characterization to avoid noise triggers, but this increased the fraction of events which experienced charge sharing. Events which experienced incomplete charge collection (ICC) were removed according to the technique in Chapter 6 by comparing depth reconstructions (“ICC” in Figure 7.1). The voxels were then classed according to their energy resolution and screened by their class’s aggregate energy resolution according to the technique described in Chapter 3 (“vox” in Figure 7.1). In this case, all voxels with energy resolution above 1.8% were removed.

The results along each step are shown in Table 7.1 and Figure 7.1. Note that both screening techniques can be implemented arbitrarily aggressively, and their relative order should affect both of their efficacies. The figure of merit (FOM) listed in table 3 is the photopeak counts divided by the energy resolution, which is the same as the normalized FOM defined by the sponsor of this project. Photopeak counts were calculated as the counts within a FWHM on either side of the photopeak mode. “Raw” includes corrections for pixel-to-pixel variations in preamplifier gain (“ch” in Figure 7.1). The energy resolutions for each pixel between steps are shown in Figure 7.2. A pixel map of the resolutions would not be meaningful after the last step because worse pixels have more voxels removed from the dataset.⁸

⁸ This dataset was used as an example in Section 3.3 to demonstrate processing techniques.

Table 7.1. Performance of 935-38AS3 at -1250 V before and after each processing step. Improvements relative to the raw performance are shaded green.

	Raw	PFR- & dur-corr.	Screened ICC	Screened Voxels
Single-pixel FWHM	4.00%	2.17%	2.13%	1.56%
Best-pixel FWHM	1.95%	1.52%	1.42%	N/A
Photofraction	15.0%	15.7%	29.0%	33.4%
Rel. Photopeak Cts	1	1.05	0.87	0.21
Rel. FOM	1	1.94	1.64	0.55

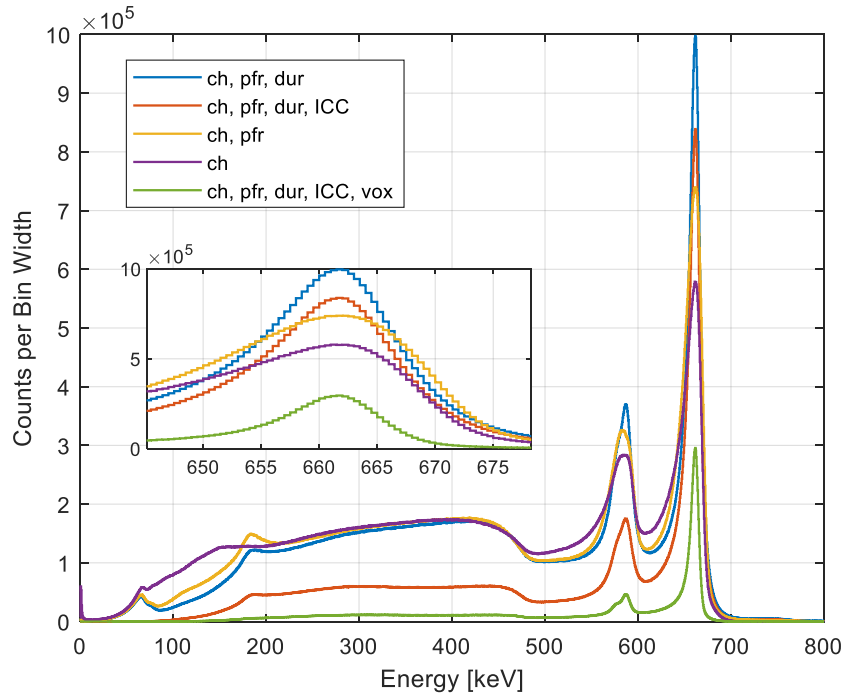


Figure 7.1. Overall single-pixel energy spectra from each step of processing listed in Table 3.

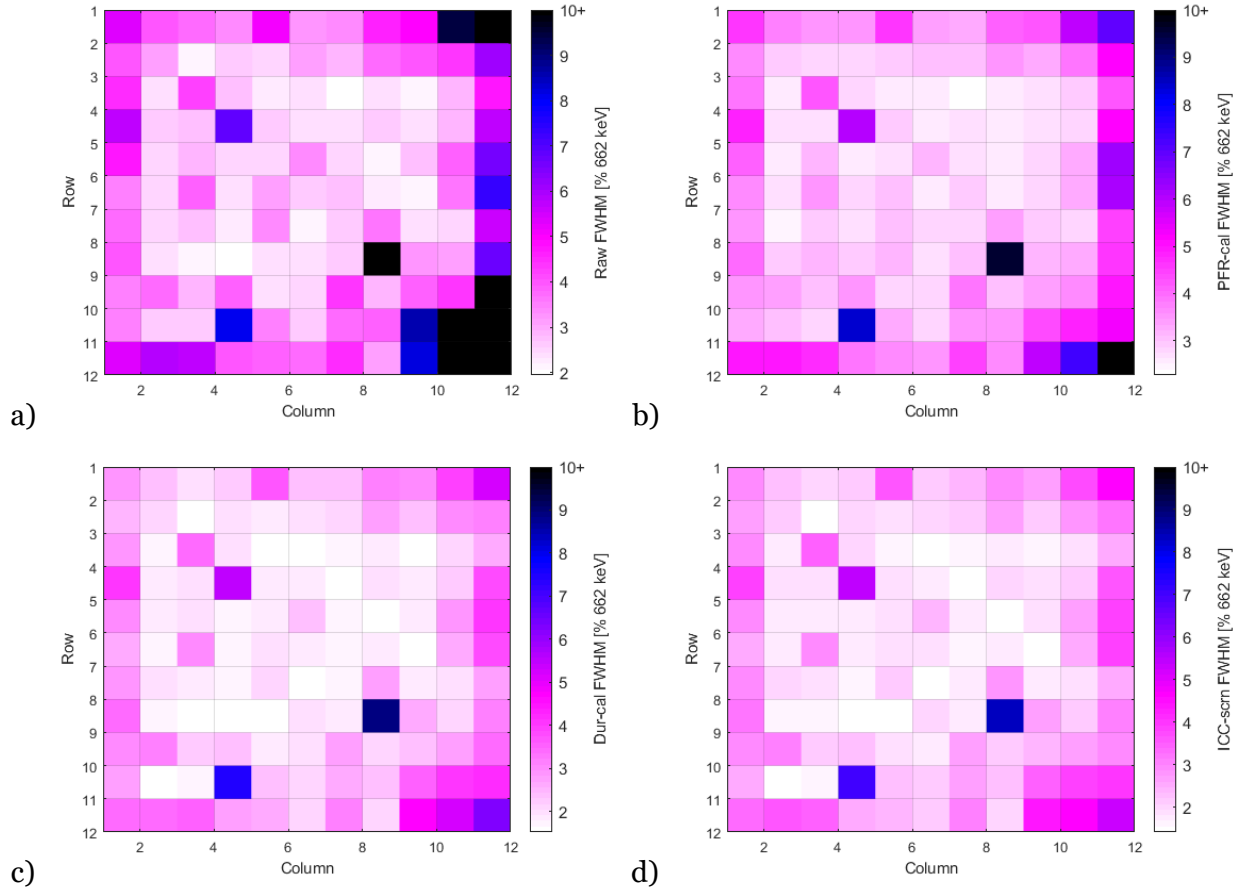


Figure 7.2. Pixel resolutions a) before any correction, b) after calibrating by PFR, c) after also calibrating by drift duration, and d) after also removing ICC events.

A steep near-pixel weighting potential gradient reduced the resolution of near-pixel events in the raw spectrum, which was corrected by PFR calibration. This introduced an artifact previously mentioned and exemplified in Section 3.3.2 which was removed during drift-duration calibration. The combined improvement in energy resolution from PFR and drift duration calibration was significant. Few events were removed from the energy spectrum during these two calibrations, no more than 6% of all events, and they were abnormal events with nonphysical depth reconstructions.

Events with physically meaningful depth and energy reconstructions but which were identified as experiencing incomplete charge collection were removed from the energy spectrum during the ICC-screening step which improved resolution at the cost of photopeak counts but most significantly improved the photofraction by removing events outside of the photopeak. This step reduced the FOM, so it may be seen as detrimental from some perspectives, but a reduction in the continuum beneath the photopeak is

important in decreasing the uncertainty in the photopeak counts when using a spectrometer for passive nondestructive assay [39].

Energy resolution improved of course after voxels with resolution worse than 1.8% were removed from the dataset, and photofraction slightly improved but at a tremendous cost of photopeak counts. Voxel screening could not be implemented in a practical source-location application but could be useful in spectroscopically identifying a source given no limitation by counts. The criterion that voxel energy resolution must be below 1.8% was semi-arbitrarily chosen here because it produced a good resolution while using more than a few voxels, but the curves relating the criterion to the parameters in the first column of Table 7.1, shown in Figure 7.3, allow a user to set a screening criterion to optimize performance according to their desired tradeoff between e.g. photopeak efficiency and energy resolution. The sharp drop in photofraction at a criterion of 1.4% was because voxels calculated to have resolutions below that criterion had poor statistics; few counts existed in these voxels.

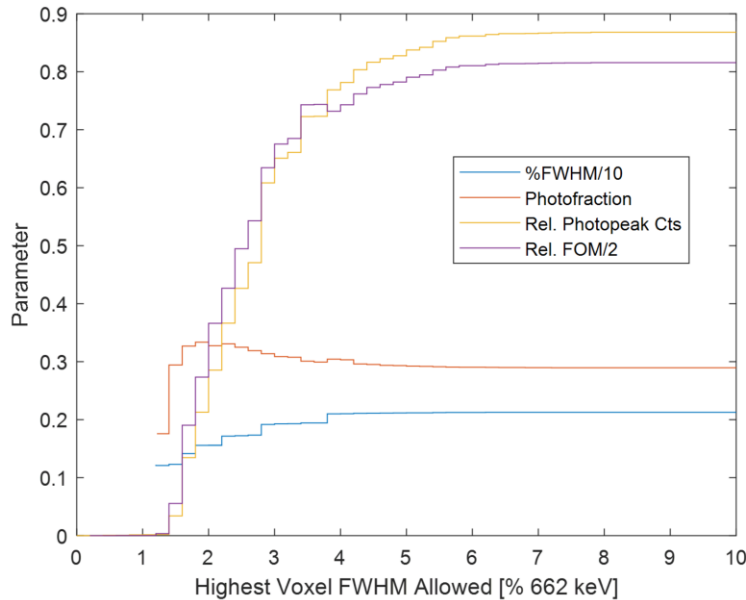


Figure 7.3. Relationship between selective criterion (voxel energy resolution) and Table 3 parameters from 935-38AS3 (after depth corrections and screening of incomplete charge collection).

7.1.2 Performance Limitations

Performance seemed limited by both spatial and temporal variations in charge collection efficiency. Figure 7.4 shows the maximum drift durations for each pixel at -1250 V over 5 mm. Maximum drift durations varied by about 5.5% and formed a clear

trend: top right pixels had the lowest drift durations and bottom left pixels had the highest drift durations. Longer drift durations increase trapping, all else equal, and arise from inhomogeneities in either the electric field or the electron mobility throughout the bulk. A gradient in impurity concentration or a slight deviation from parallel in the geometry of one electrode relative to the other were suspected as possible causes. Variations in charge collection efficiency from pixel to pixel were corrected when preamplifier gain is calibrated and when depth corrections were applied, but a gradient within a pixel was not explicitly corrected. Evidence is also presented for sub-pixel variations in Section 4.2.6. Sub-pixel calibrations are expected to further improve performance but require excellent statistics to be implemented, thus are complicated by temporal variations in performance.

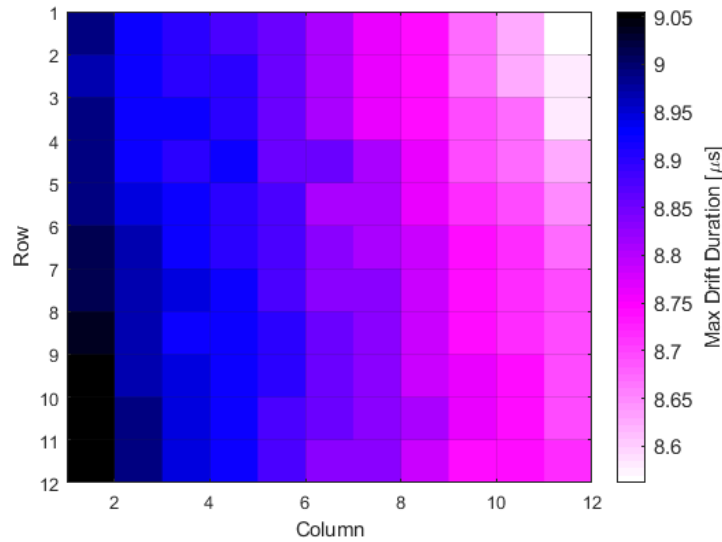
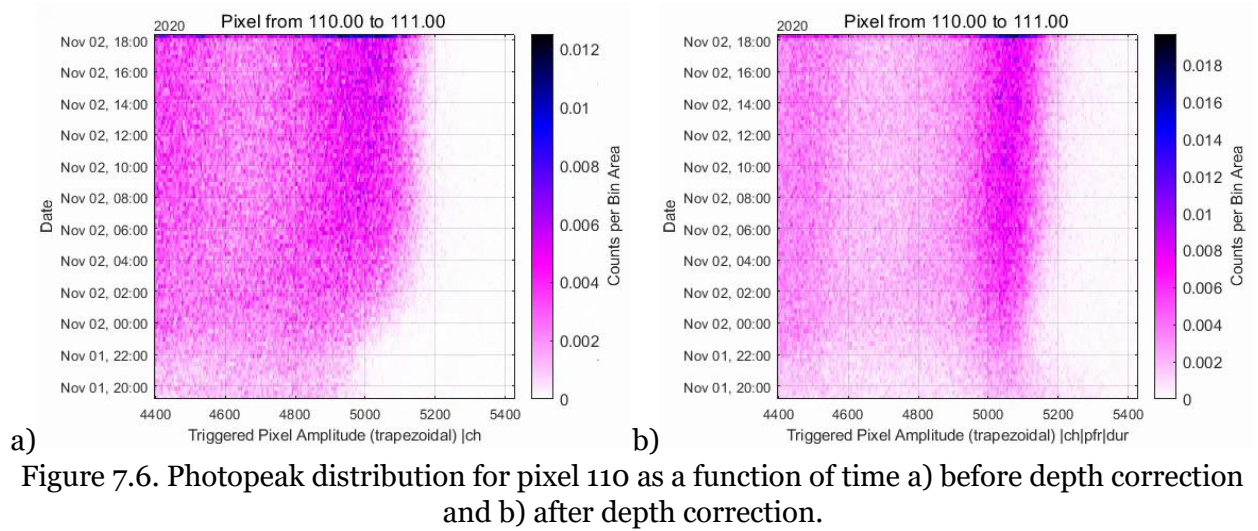
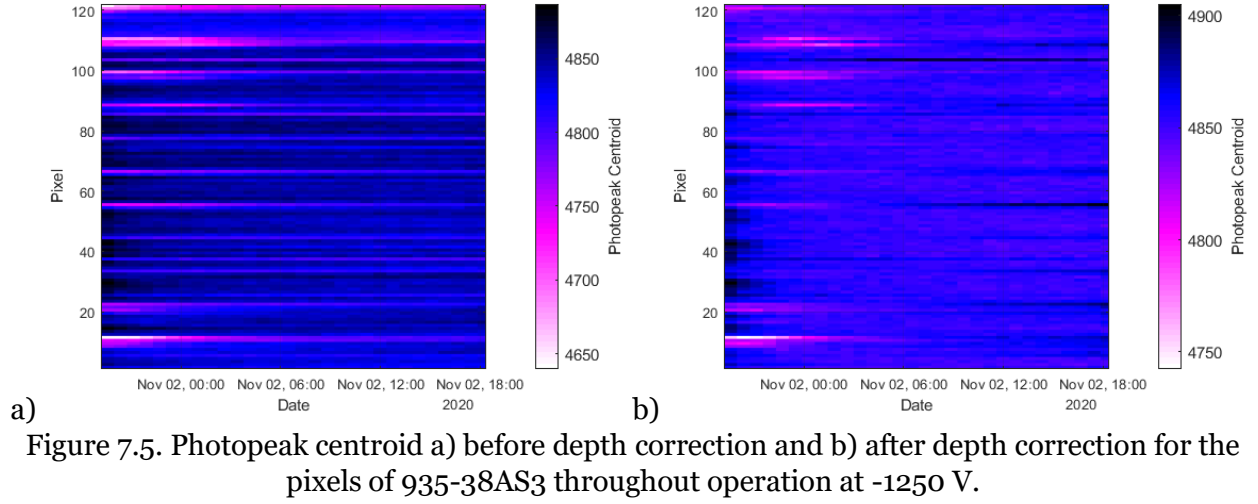


Figure 7.4. Maximum drift duration of each pixel of 935-38AS3 during operation at -1250 V.

Figure 7.5a shows the changes in photopeak centroids for each pixel before depth calibrations (before both PFR and drift duration) as a function of measurement time. Most pixels' gain decreased in amplitude over the first six hours, but some strictly increased. Temperature fluctuations were suspected to be the initiator of these changes because of observations of other detectors discussed in Section 4.2.1, but the reasons for different trends of different pixels is unknown. Depth correction reduced the magnitude of the changes in photopeak centroid with time, shown in Figure 7.5b, and for some pixels it almost removed the changes altogether. The depth correction of pixel 110 shows the most dramatic improvement over uncorrected performance for early events, shown in Figure 7.6.



Depth correction improved performance, even creating a photoppeak, because this change in performance was caused by a large low-single-pixel-count region leaving only the near-pixel region active at the beginning, the signal amplitudes from which were reduced by a steep weighting-potential gradient. This is evidenced by the depth-separated energy spectra integrated over the first two hours of operation shown in Figure 7.7. PFR calibration successfully reconstructed these events because the performance of the active region during early operation was mostly the same as during the rest of the operation period. The same is true of pixel 11, except the PFR calibration resulted in slightly wrong energy reconstructions likely because the electric field slightly changed or because hole mobility-lifetime product changed. The extent of low-SP regions in this crystal is shown in Figure 4.15 in Section 4.2.3.

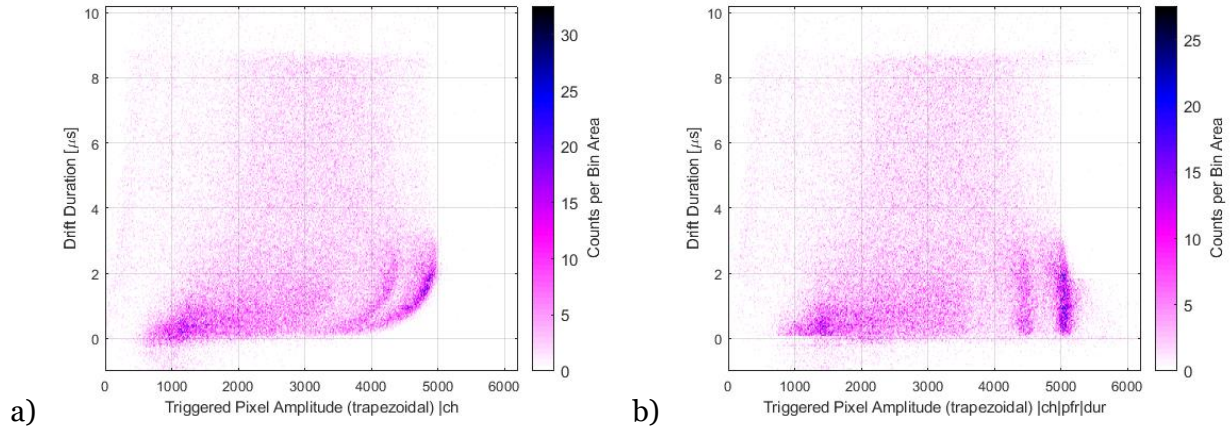


Figure 7.7. Depth-separated energy spectrum from pixel 110 from the first two hours of operation a) before depth correction and b) after depth correction.

These changes in centroid with time were next used to self-calibrate the response, but because the change cannot be predicted such a calibration only serves as an estimate of what the performance could be if the change was mitigated. Time-calibration was applied after channel-gain-calibration (“Raw” from Table 7.1) and then the same calibrations listed in Table 7.1 were applied. Results were negligibly better, which shows amplitude drift over time from e.g., temperature fluctuations affecting preamplifier gain are not a significant factor.

This does not mean temporal variations did not limit the resolution. Small fluctuations in depth-gain relationships because of changes in electron lifetime may still have been present, but a prohibitively high count rate would have been required to collect enough statistics per time bin to perform a depth correction for every time bin within a single measurement. Videos of the depth-separated energy spectra for individual pixels were studied and no further artifacts or changes could be identified, so the resolution must be limited by static (unchanging) material or electrode contact nonuniformities.

7.1.3 Bias and Calibration Dependence

Operating bias voltages were generally either 2 kV/cm or -1000 V, whichever was less, but radiation measurements were sometimes conducted during the periods between bias stepping as described in Section 2.3 which allowed the dependence of performance on operating bias to be studied.

10.3-mm-thick 128BAS3 was biased to -2000 V in steps of -400 V to optimize operating bias. This crystal had 3×3 1.72-mm-pitch Au/Cr pixels. Depth corrected

performance did not improve above -800 V as shown in Table 7.2. Resolution is typically expected to improve with increasing bias by decreasing charge-carrier drift duration, mitigating nonuniformities in charge-carrier lifetime. No significant hole motion was observed, average electron mobility was found to be independent of bias ($\mu_e = 23.8(2)$ cm²/Vs), and effects of trapping can be seen in uncalibrated depth-separated energy spectra such as Figure 7.8, thus it may be concluded that while electron lifetime is low enough to degrade raw spectra at low biases, any small-scale gradients in electron lifetime are not large enough to significantly degrade the energy resolution of calibrated spectra. Perhaps the resolution is limited by temporal fluctuations in electron lifetime caused by temperature fluctuations, or by spatial uniformity in ionization energy. Resolution may have been slightly worse at -2000 V than at lower voltages because of an increased leakage current, but leakage current was not measured during these measurements.

Table 7.2. Energy resolutions of 128BAS3 recording Cs-137 gamma rays, self-calibrated using plane-pixel ratio and using drift duration.

Day of operation	Bias Voltage	Plane-pixel ratio, FWHM		Drift duration, FWHM	
		Single-pixel	Best-pixel	Single-pixel	Best-pixel
1	-400 V	4.5%	3.3%	3.3%	2.6%
2	-800 V	2.3%	1.7%	2.0%	1.7%
3	-1200 V	2.1%	1.7%	2.0%	1.6%
4	-1600 V	2.1%	1.7%	2.0%	1.6%
5	-2000 V	2.4%	1.9%	2.1%	1.7%

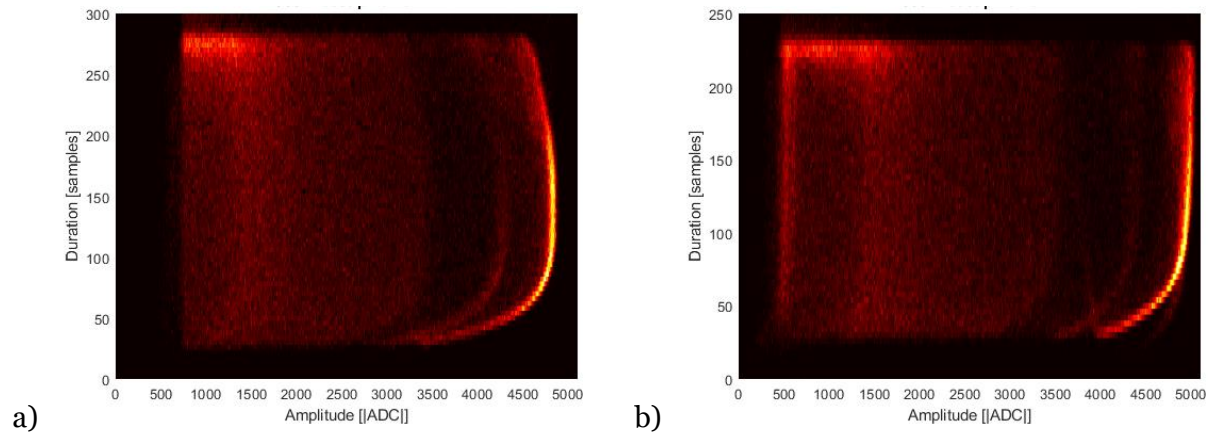


Figure 7.8. Raw drift-duration-separated energy spectra of Cs-137 as recorded by device 128BAS3 at a) -800 V and b) -2000 V.

Although the FWHMs were equivalent at -800 V and -2000 V after depth correction, the FWTM was better at -2000 V due to a high continuum beneath the photopeak, which can be seen in Figure 7.9. This may have been due to some regions of heavy trapping which are mitigated by the short drift duration at -2000 V, or it may have been due to a difference in incomplete charge collection.

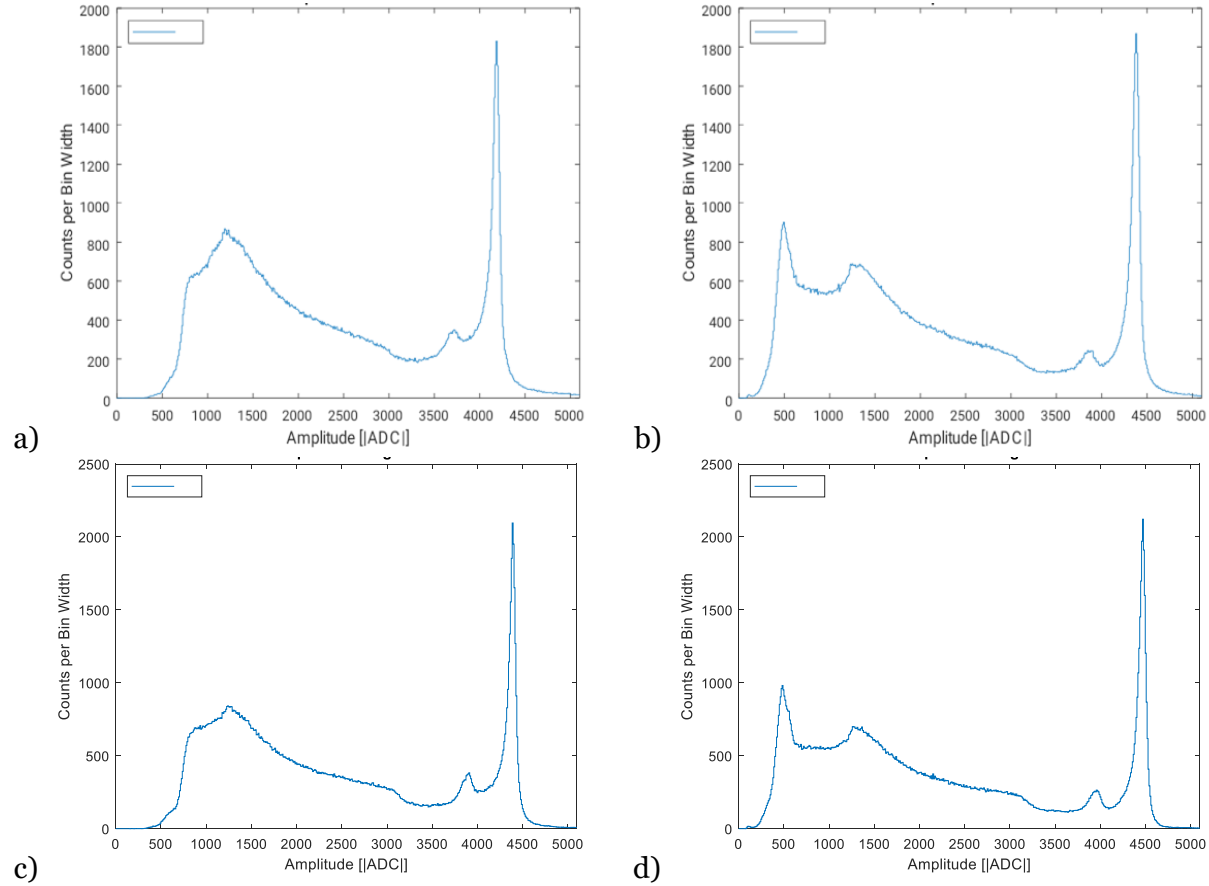


Figure 7.9. -800 V bias (a,c) and -2000 V bias (b,d) single-pixel spectra self-calibrated using plane-pixel ratio (a,b) and using drift duration (c,d) from device 128BAS3.

The latter explanation is evidenced by the lower trigger threshold used in the measurement at -2000 V which allowed Tl x rays (the most prominent of which are 70.8, 72.9, 82.6, and 85.9 keV) which escaped from interactions under the guard ring to cause triggers when they were absorbed under a pixel. These x rays have a mean free path of about 0.5 mm, large enough to significantly leak between pixels. The neighbor origin of the x rays could be known because they are reconstructed to depths throughout the thickness of the crystal (not shown) despite having a low mean free path, and the same

events are reconstructed to nonphysical depths when using the plane-pixel ratio (not shown), which is a sign of incomplete charge collection as explained in Chapter 6.

The higher hardware-trigger threshold at -800 V seems to have prevented the triggering of neighbor pixels during significant charge sharing, inappropriately demoting multi-pixel events to single-pixel events. The trigger threshold can significantly affect single-pixel spectra in this way. If the trigger threshold had been set consistently, the calibrated spectra produced at -800 V and -2000 V may have been identical. Setting the threshold consistently was complicated by changes in sampling frequency and digitizer range between measurements.

The difference in performance between calibrations using plane-pixel ratio and drift duration is compared in Table 7.2 and Figure 7.9 as well. Plane-pixel ratio (usually called cathode-anode ratio, CAR) has historically been used in CZT detectors for single-pixel events because of its high precision, while drift duration (usually called timing) has been used in CZT detectors for multi-pixel events because plane-pixel ratio is skewed by multiple interactions. Drift duration may work better in this example because charge-shared events are unsuccessfully calibrated when using plane-pixel ratio, or it may be because the near-pixel weighting potential gradient is slightly shallower when parameterized by drift duration instead of plane-pixel ratio, but this has not been proven. Calibrating by drift duration instead of plane-pixel ratio should be expected to perform better for detectors in which there is significant hole-induced signal because of artifacts like those shown in Section 4.2.5 and because of distortion of the plane-pixel ratio as discussed in Chapter 5, especially since a variation in hole transport properties was observed in Section 6.3 from which a lateral variation in plane-pixel-ratio distortion can be inferred.

Detector 935-38AS3, the performance at -1250 V of which is described in Section 7.1.1, was operated above -1000 V after unusually stable performance at -1000 V was observed. The leakage current during operation above -1000 V fluctuated slightly as shown in Figure 7.10. The overall single-pixel energy resolutions are shown in Table 7.3. A software memory error prevented data from being recorded during operation at -1500 V.

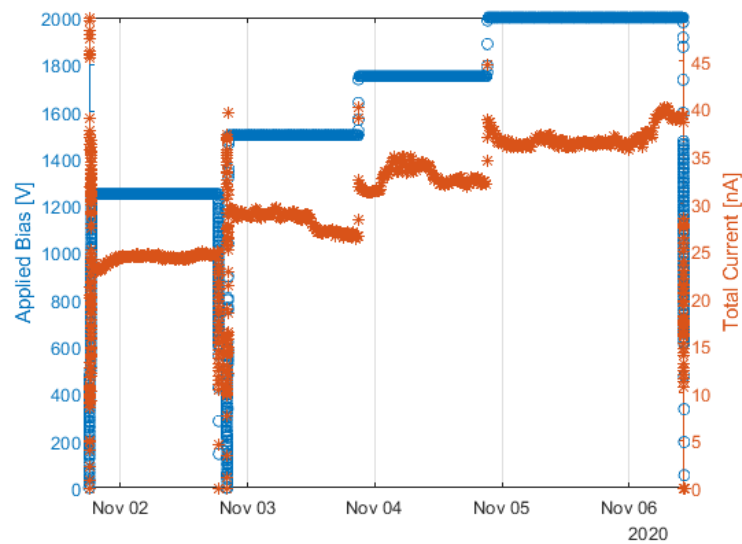


Figure 7.10. Bias and current for high-bias (>1000 V) testing of 935-38AS3. The actual voltage applied to the planar electrode was negative.

Table 7.3. Single-pixel drift-duration-calibrated energy resolutions of 935-38AS3.

	-1000 V	-1250 V	-1750 V	-2000 V
FWHM at 662 keV	3.2%	2.2%	3.5%	4.4%

Figure 7.11 shows the distributions of self-calibrated single-pixel resolutions for the pixels of 935-38AS3 at -1000 V, -1250 V, -1750 V, and -2000 V. In the best measurement (Figure 7.11b), the plurality of pixels had a better resolution (1.5-2%) than nearly all pixels in any other measurement—a stark improvement.

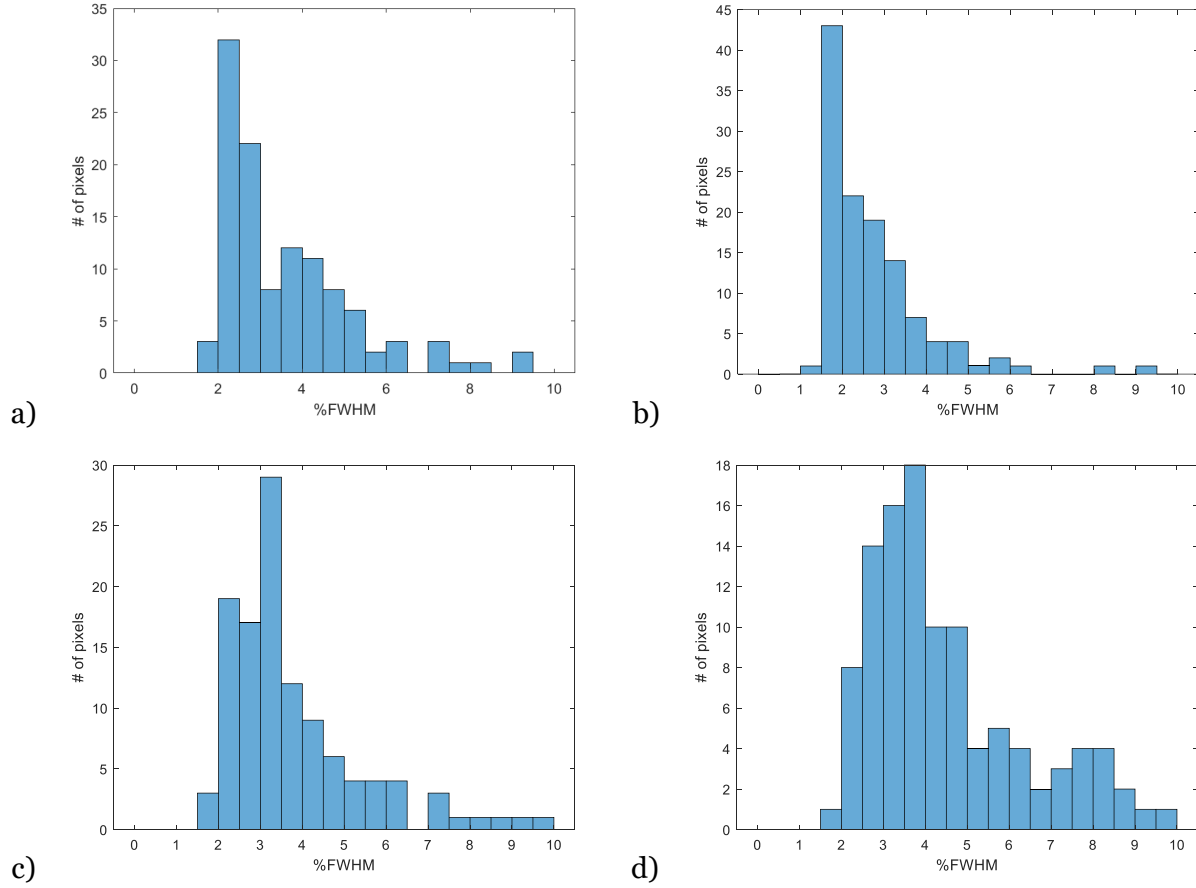


Figure 7.11. Distribution of self-calibrated single-pixel energy resolutions at 662 keV for the pixels of 935-38AS3 at a) -1000 V, b) -1250 V, c) -1750 V, and d) -2000 V.

The depth-separated energy spectra (not shown) for most pixels at -1750 V and -2000 V appeared to have degraded at all depths, so it is suspected that higher leakage currents caused more noise on the pixel signals which degraded resolution. -1250 V seems nearly optimal for this approximately 5-mm-thick crystal. N.b. the depth-corrected results shown in Table 7.1 were generated using a more careful depth calibration including more optimized binning and correction by prompt-final ratio which was not used to generate Figure 7.11. The distribution of pixel resolutions for the depth-corrected data shown in Table 7.1 is shown in Figure 7.12.

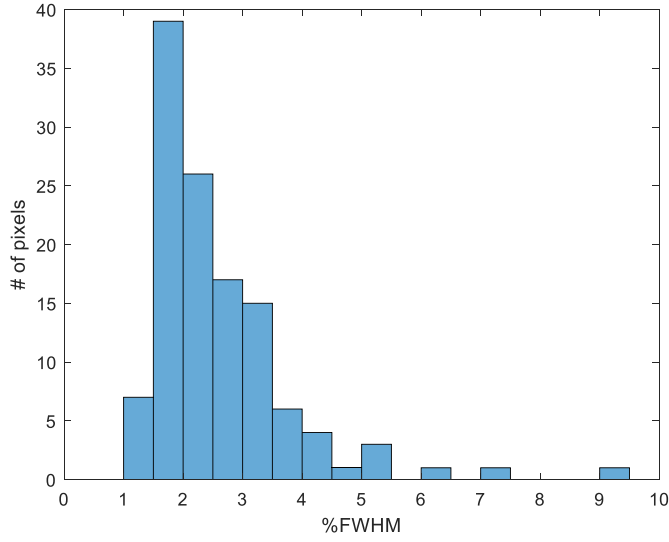


Figure 7.12. Distribution of self-calibrated single-pixel energy resolutions at 662 keV for the pixels of 935-38AS3 at -1250 V after thorough depth correction.

7.2 Performance of CdZnTeSe

Two $\text{Cd}_{0.90}\text{Zn}_{0.10}\text{Te}_{0.98}\text{Se}_{0.02}$ (CZTS) crystals with 2×2 -pixel anodes and planar cathodes were received by the University of Michigan from Utpal Roy of Brookhaven National Laboratory (BNL) and are described in Section 2.1.

BNL1-S2, the first CZTS crystal, was characterized for three consecutive days at three different operating voltages. Characterization revealed significant hole motion and variations in bulk material characteristics on a sub-pixel spatial scale, especially in electron drift speed. Later attempts to characterize the crystal revealed electrical breakdown and high leakage current at typically operational electric fields.

The resistivity of the crystal was measured from -1000 V to 500 V (applied to the cathode, with the anodes held at ground by preamplifiers) producing the IV curve shown in Figure 7.13. From -500 V to 500 V a resistivity of $5.3 \times 10^{10} \Omega \cdot \text{cm}$ was measured, but below about -700 V the resistivity dropped to $8.8 \times 10^9 \Omega \cdot \text{cm}$.

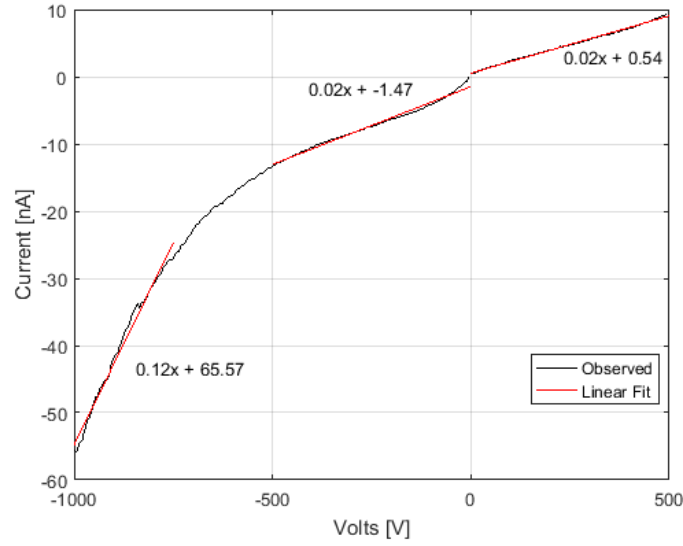


Figure 7.13. Total leakage current across crystal versus voltage applied to cathode showing nonlinearity.

Figure 7.14 shows the average electron drift time for interactions at each depth and the calculated average drift speed for each depth under two pixels. Not only did the drift speed vary with depth, but it also varied laterally across the crystal (inter-pixel). Space charge likely distorted the electric field in the crystal, but a variation in electron mobility has not been ruled out.

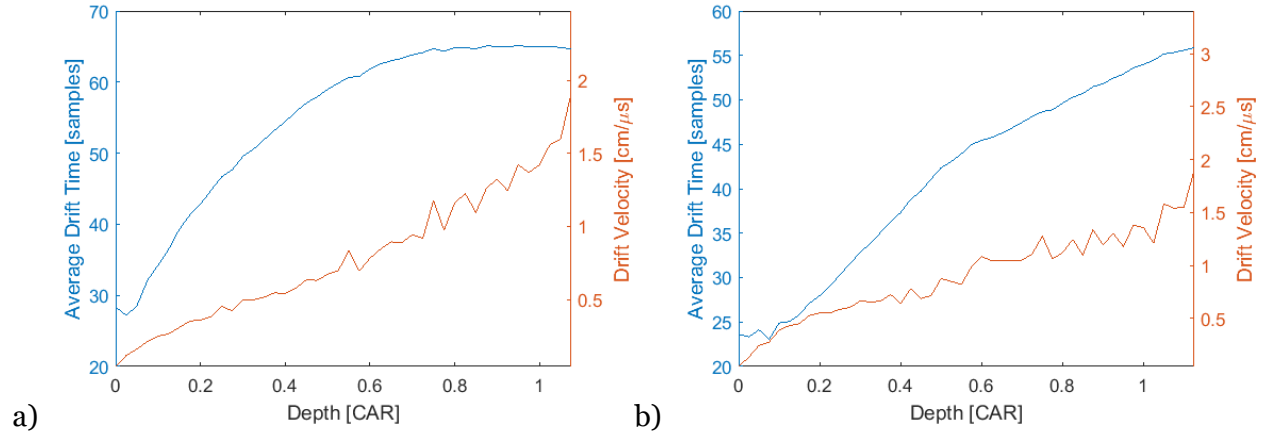


Figure 7.14. Average observed electron drift time and calculated electron drift speed for each depth bin under a) pixel 1 and b) pixel 2 during day 1 at -1000 V.

Because the electron drift speed was nonuniform in depth, the planar-cathode waveform was nonlinear and the inflection point marking the electron collection time was obscured. This reduced the accuracy of the cathode amplitude pickoff, which worsened

the depth-corrected energy resolution. Note that the pixel with more uniform drift speed (Figure 7.14b) had better resolution as shown in Table 7.4.

Table 7.4 shows the energy resolution calculated from Cs-137 energy spectra which were acquired at -1000 V, -750 V, and -500 V. Electrical breakdown was observed above 1000 V. This breakdown voltage decreased to -500 V after repeated cyclic biasing.

Table 7.4. Depth-corrected energy resolutions of a Cs-137 source.

Pixel	1000 V FWHM [%]	750 V FWHM [%]	500 V FWHM [%]
1	5.5	4.3	5.1
2	3.4	3.2	3.6
3	2.2	2.5	3.2
4	3.0	3.1	3.2

Photopeaks at all depths and on all pixels were accompanied by unusual low energy continua. Figure 7.15 highlights a photopeak and low energy continuum in a depth-corrected energy spectrum. Figure 7.16 shows examples of waveforms from this photopeak and continuum. The waveforms from the photopeak are as expected, but the anode waveforms from the continuum have notable variations in shape. These variations are caused by variations in charge cloud shape as it reaches the pixelated anode due to a laterally nonuniform drift speed, or nonuniform trapping-site density or detrapping probabilities, or both. This may have been a result of significant bulk material nonuniformity across the x-y plane within each pixel and would be mitigated by a higher bias, or it may have been the result of variable resistance between the bondless pins and the electrodes (this crystal was unbonded as described in Chapter 2). This crystal was sent back to BNL to be wire bonded, after which testing would reveal if the nonuniform drift velocity was from poor material or poor bondless contact, but it was not returned.

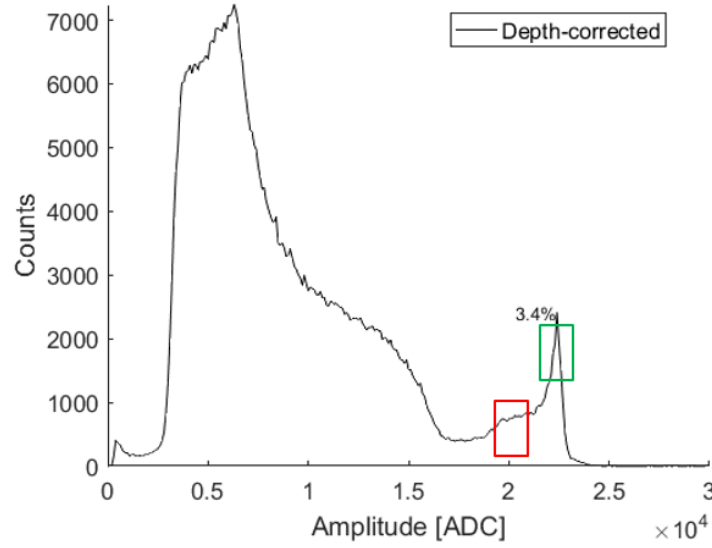


Figure 7.15. Depth-corrected anode energy spectrum from pixel 2 on day 1 with peak (green) and continuum (red) regions marked.

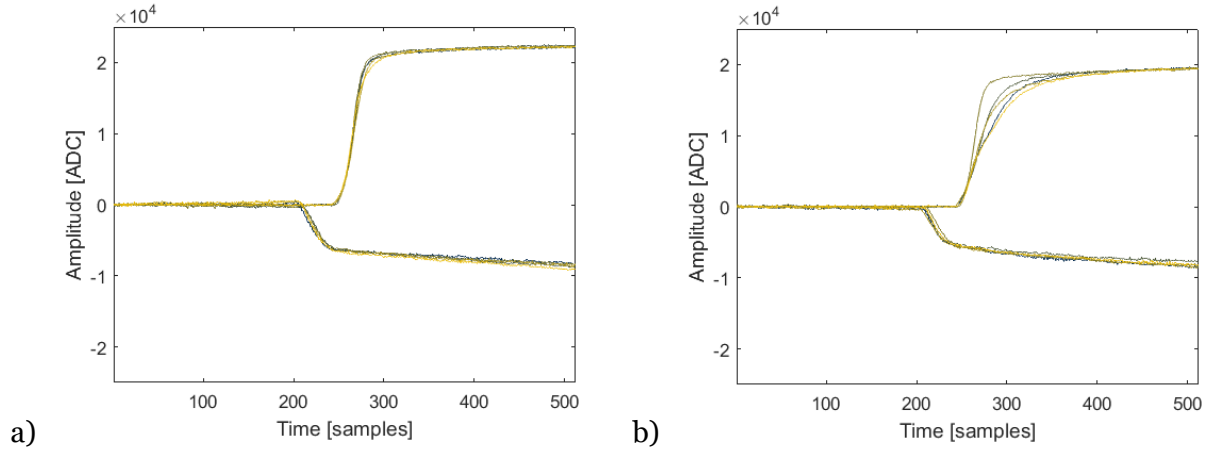


Figure 7.16. Typical waveforms comprising the a) peak of the depth-corrected energy spectrum and b) the continuum of the depth-corrected energy spectrum.

Hole motion was observed on waveforms, as evidenced by the slope at the end of the cathode waveforms in Figure 7.16. Hole collection was observed in events near the planar cathode, visible in the waveforms shown in Figure 7.17. The ratio of electron drift speed to hole drift speed was calculated to be about 0.05 from the waveform slopes but was mostly obscured by the spatially nonuniform drift speeds.

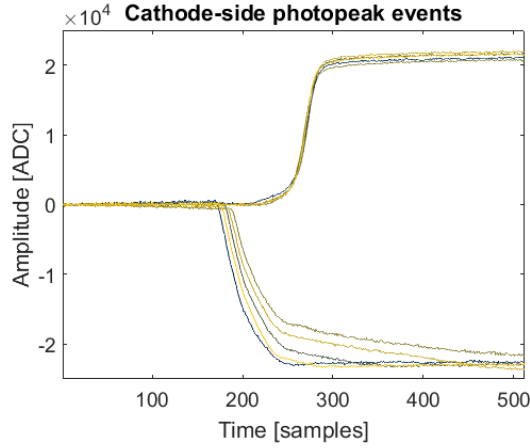


Figure 7.17. Waveforms from interactions near the planar cathode showing hole collection by the cathode.

BNL2-S2, the second CZTS crystal, was first operated with a very low bias of -10 V. Separation between a photopeak and Compton continuum could be discerned from bivariate histograms showing energy spectra separated by drift duration, shown in Figure 7.18.

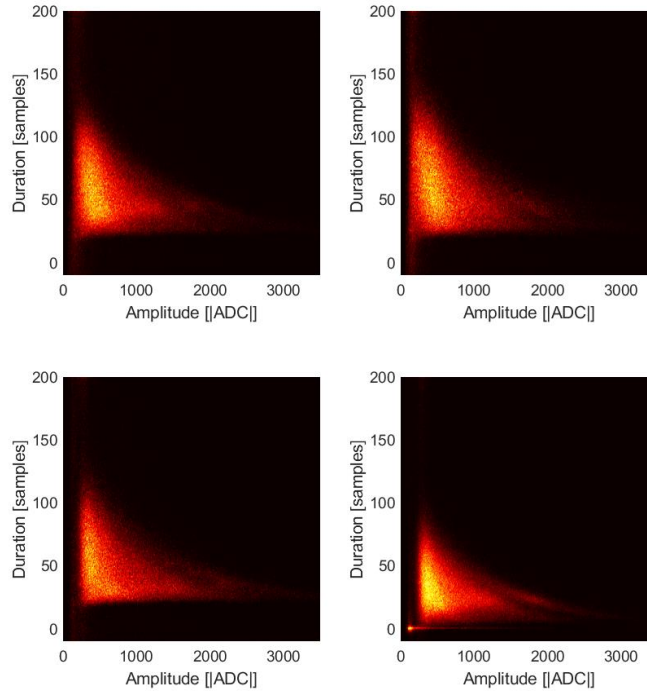


Figure 7.18. Drift duration vs. pixel amplitude of BNL2-S2 under Cs-137 irradiation at 10 °C and -10 V.

Shorting between grounded pins and the cathode occurred at biases above -2850 V. Electrical discharges occurred on most pixels at biases above -1000 V. These discharges were mitigated by cooling the detector to 10° C. Vibrations generated by the

environmental chamber used to cool the detector induced 50-100 Hz signals in the loose wire bonds. Strengthening the mechanical support and adhesion between the crystal and its carrier board, tautening the wire bonds, and trimming stray wire may have mitigated this noise. Grounding of the grid and guard ring would likely have significantly improved stability, but this required destruction of the crystal's adhesion to its carrier board, so it was not performed.

The best energy resolution observed was 7.4% overall, 4.5% best pixel after screening noise triggers in post processing as described in Section 4.1.1. The Frisch collar caused nonlinearity in the cathode signal which likely worsened depth calibration. The energy spectra before noise screening are shown in Figure 7.19 and the final spectrum after noise screening and combining all pixels is shown in Figure 7.20.

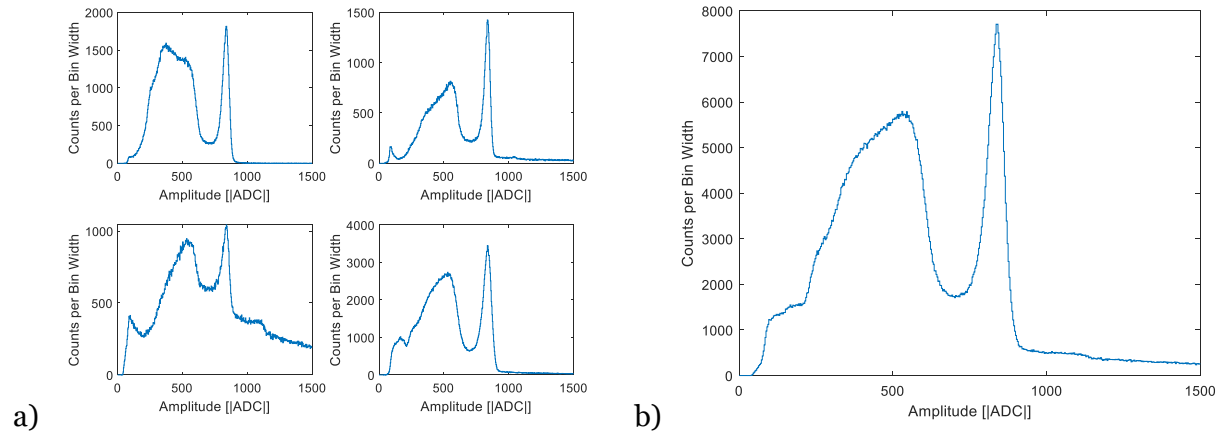


Figure 7.19. (a) Self-calibrated spectra for each pixel and (b) total single-pixel self-calibrated spectrum for BNL2-S2 at -2000 V irradiated by Cs-137 and at room temperature.

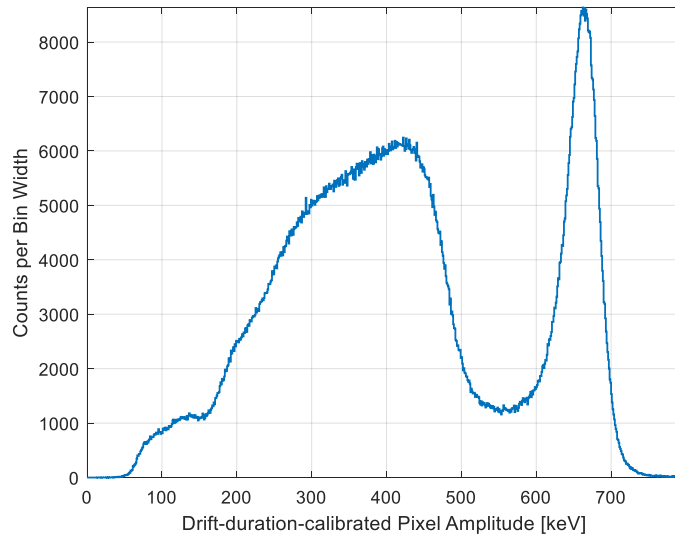


Figure 7.20. Energy spectrum from BNL2-S2 after screening noise triggers.

7.3 Performance of CsPbBr_3

A CsPbBr_3 crystal about 1-mm thick with planar electrodes was received from and tested with Yihui He and Mercouri Kanatzidis of Northwestern University, corroborating his 2018 results [5]. A new backplane to route connections between the electrodes, preamplifiers, digitizers, and power supplies was designed and assembled because capacitive coupling of both the anode and cathode were necessary as described in Chapter 2. Degradation of the energy spectrum was visible after days of periodic operation, shown in Figure 7.21, which was mitigated in future fabrications by changing the electrode materials [27]. Further testing of this device and others from Yihui He was performed at the University of Michigan by Matthew Petryk.

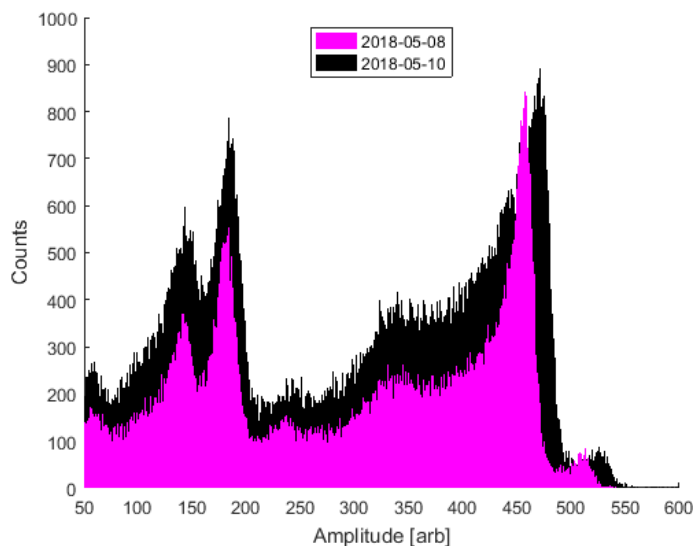


Figure 7.21. Co-57 spectra measured two days apart by a planar CsPbBr₃ detector using 1 μ s shaping analog electronics. Gain may be slightly different between measurements.

A CsPbBr₃ crystal with dimensions 8.12×6.72×3.27 mm³ having 2×2 1-mm² pixelated cathodes, a guard ring, and a 16-mm² planar anode was received from Teddy Feng and Jinsong Huang of the University of North Carolina. The resistivity was measured using an IV curve with about a 30 second dwell at each voltage during which an increase in leakage current was generally observed for negative voltages, shown in Figure 7.22. Most of the change in current was through the guard ring, likely a surface effect, as determined by the change in pixel leakage current shown in Figure 7.23, measured as described in Section 2.3. The resistivity was calculated from the IV relation at positive biases and is given in Table 7.5.⁹ The resistivity calculated for the planar anode includes surface leakage, so the resistivity calculated from the pixel cathodes should be a better measure of bulk properties. Of those, one pixel showed lower resistivity than the rest, perhaps because of a manufacturing error such as a low resistance path to the guard ring.

⁹ Pixel numbering is arbitrary; there were only four pixels.

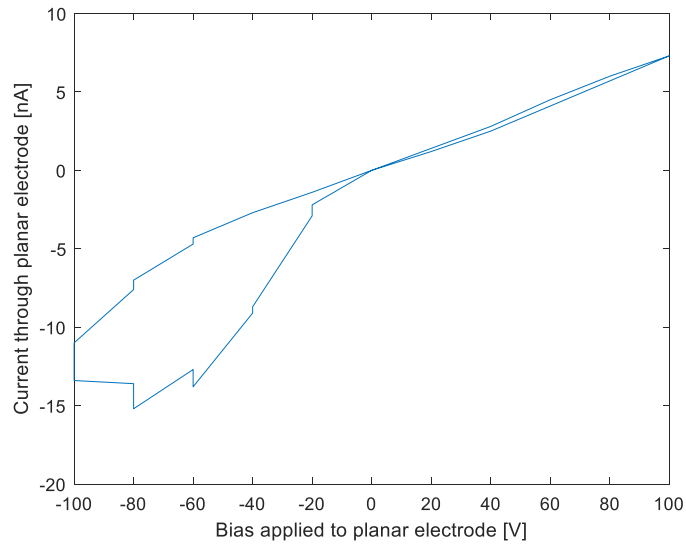


Figure 7.22. I-V curve measured from the CsPbBr₃ detector manufactured by Teddy Feng of UNC.

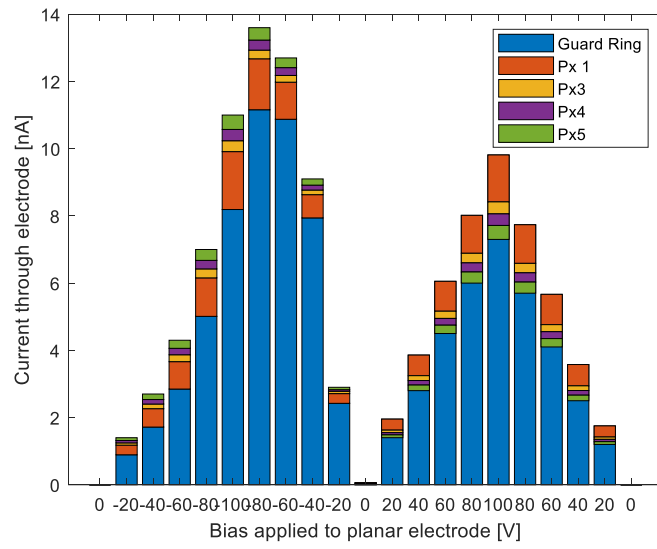


Figure 7.23. Leakage current components through the pixels and guard ring.

Table 7.5. Resistivity of each pixel calculated from the currents measured at positive biases.

Electrode	Calculated Resistivity (+V) [$\Omega\cdot\text{cm}$]
Pixel 1	2.22×10^9
Pixel 3	8.62×10^9
Pixel 4	7.39×10^9
Pixel 5	8.91×10^9
Plane	6.56×10^9
Average of pixel 3, 4, 5	$8.3(8)\times 10^9$

A low bias (50 V) was used during operation because of the unstable and high leakage current, yet the leakage current increased from about 5 nA to about 200 nA over one day of operation with most of the change occurring between hours five and seven. Gamma-ray-induced waveforms were recorded during the first few hours before noise triggers became overwhelming, but no energy spectrum could be reconstructed because of the severe trapping at this low bias.

Note that further collaboration with Yihui He and Mercouri Kanatzidis of Northwestern University in 2019 produced astounding results with CsPbBr₃ including an energy resolution of 1.6% to 1.4% FWHM at 662 keV with a high peak-to-Compton ratio from a 2×2-pixel 4.64-mm-thick detector, operated and analyzed by Matthew Petryk of the University of Michigan using the same equipment and techniques [27].

Chapter 8 Conclusion

8.1 Summary

Alternative room-temperature semiconductor (ARTS) materials were tested over the course of this work, including CdZnTeSe and CsPbBr₃, but most effort was spent testing TlBr.

Pixel ambipolar (electron- and hole-) sensitivity was common to all materials tested and will be an important concept in future studies of ARTS. Ambipolar pixel signal was found to mitigate the weighting-potential dead region and improve the accuracy of the plane-pixel ratio as a depth reconstruction method. A technique to extract near-pixel position from the pixel waveform shape caused by ambipolar signal was devised and implemented on TlBr detectors to improve energy resolution. This technique is applicable to any pixelated room-temperature semiconductor detector material whose electron- and hole- transport properties are similar within an order of magnitude, including some TlBr, CdZnTeSe, and halide perovskites.

Detectors of all materials tested were prone to noise triggers because of issues with either material stability or electrical mounting. This was addressed by increasing the trigger threshold and reducing the bias voltage in some cases, both of which increased the fraction of single-pixel events which experienced incomplete charge collection (ICC). Additionally, dramatic changes in electron lifetime were observed during the operation of some TlBr crystals which increased ICC. Two methods of identifying and screening incomplete charge collection (ICC) in pixelated gamma-ray spectrometers accommodating ambipolar signal were derived and applied to the responses of room-temperature TlBr.

Method 1—comparing charge reconstructions—relies on fitting and removing hole-induced contributions to the signal amplitude distributions, which assumes material properties such as hole mobility-lifetime product are homogeneous. Method 2—comparing depth reconstructions—is more robust to heterogeneous material properties because of its empirical implementation but requires better counting statistics than

method 1. Screening with method 1 is simple: an upper and lower bound are set; screening with method 2 is more complex: bounds around a correlation function are set. The two methods performed similarly. Both methods fundamentally rely on the difference in the effect of ICC on the pixel and plane signals caused by their weighting potentials. The fit of the hole component of the plane signal in TlBr when implementing method 1 revealed laterally nonuniform hole transport properties.

Several anomalies such as spatial variations in electron and hole transport properties and localized Auger recombination were observed in TlBr. Some anomalies were corrected in digital processing. The best recent performance of an 11x11 TlBr detector from the University of Michigan after all corrections was found to be between 1.4% and 2.1% FWHM at 662 keV dependent on the fraction of the active volume used.

8.2 Continuing Work

The improvement in the active volume by ambipolar signal should improve imaging results, though the focus of this work was on spectroscopy. Collimated measurements were not trusted to evaluate the uncertainty in depth associated with the prompt-final ratio because of subtle instabilities in the devices tested on the timescale of collimated measurements. If the prompt-final ratio has higher precision than the plane-pixel ratio for near-pixel events, the weighting-potential dead region in unipolar-sensitive imagers may become the high-resolution region in ambipolar-sensitive imagers.

The method of identifying ICC using charge reconstructions assumes that all ICC is from charge leakage, not charge trapping. If the mechanism of ICC was known for each event, and amplitude and timing pickoffs were sufficiently precise, the charge deficit from ICC could be calculated and the true energy could be reconstructed despite ICC, instead of simply removing the events which experienced ICC. The type of ICC was determined for some events in this work (Section 4.2.5), but a robust systematic approach has not yet been developed.

Calculation of the charge deficit from ICC assuming charge trapping was attempted for TlBr crystal 175CS5-4 because it provided a good example of a dramatic decrease in electron lifetime during operation which increased ICC, but the attempt failed because the model used did not allow for amplitude and timing uncertainty, did not include pixel signal induction from trapped charge, and did not allow for inhomogeneous charge

transport properties. The inclusion of pixel signal induction by trapped charge in the charge-trapping model of ICC event identification will be necessary before it is possible to reconstruct the charge deficit near-pixel.

The specific material property or properties (μ_h , τ_h , or E) responsible for the lateral variation in hole transport properties observed in TlBr during ICC-screening method 1 could not be discerned from the data but may be discernable in other datasets or with clever processing. Application of the technique to 11×11 -pixel detectors may reveal correlations between hole transport or its homogeneity and energy resolution or other performance metrics.

Other uses of redundant information may lead to other event screening techniques and discoveries. E.g. the method of calculating electric field strength using plane waveform slopes [35] and the method using the envelope of the plane waveform slopes from all depths (developed by collaborators at Lawrence Livermore National Laboratory) reveal information about drift velocity and charge trapping during the transit of a charge cloud. This information could be compared with aggregate parameters such as the distribution of drift durations vs. depth and photopeak centroid vs. depth. Redundant information could also come from separate hardware, such as a photodiode to detect Cerenkov emissions from photoelectrons, which has been implemented alongside charge-induction measurements [40]. The usefulness of event screening should extend well from spectroscopy into imaging, and inversely, calibrating with events whose image correlates to the calibration source location may also improve calibration and screening efficacy.

The depth calibration and tunable event screening methods developed in this work could be performed iteratively, with varying levels of strictness, which may lead to better performance. E.g., the calibration by prompt-final ratio could be determined from only events with high waveform reconstruction accuracy and no ICC and then applied to all events. A duration calibration could be performed next, and the new energy reconstruction could be used as the pixel-amplitude estimate in calculating the plane-pixel ratio which is finally used to screen ICC events in the final energy spectrum.

The transient phenomena observed in TlBr deserve further study to understand their cause and permanence or relaxation time, especially with respect to temperature. This should be enabled by more frequent use of the ASIC-based systems which offer better

environmental control. Quantitative estimates of the electron mobility-lifetime products as a function of time and position could be performed using techniques which model the marginal decrease in charge carrier population as a function of drift duration [41].

The most notable and misunderstood transient phenomenon in TlBr during this work was the change in leakage current, especially the rapid large spikes. Theories of microplasma breakdown and streamer formation were studied over the course of this work [42]–[48]. Evidence of negative differential resistance in TlBr was not found at biases used in this work. Electrical treeing along the surface of a crystal was observed, reported in Section 4.2.8. A predictive model which can be used to mitigate current transients during operation of TlBr is still needed.

Bibliography

- [1] B. Dönmez, Z. He, H. Kim, L. J. Cirignano, and K. S. Shah, “Collection of holes in thick TlBr detectors at low temperature,” *Nucl. Instruments Methods Phys. Res. Sect. A Accel. Spectrometers, Detect. Assoc. Equip.*, vol. 689, pp. 7–11, 2012, doi: 10.1016/j.nima.2012.06.020.
- [2] W. Koehler *et al.*, “Quantification of the Conditioning Phase in Cooled Pixelated TlBr Detectors,” *IEEE Trans. Nucl. Sci.*, vol. 62, no. 4, pp. 1785–1790, 2015, doi: 10.1109/TNS.2015.2448420.
- [3] K. Hitomi, N. Nagano, T. Onodera, S. Y. Kim, T. Ito, and K. Ishii, “Fabrication of double-sided thallium bromide strip detectors,” *Nucl. Instruments Methods Phys. Res. Sect. A Accel. Spectrometers, Detect. Assoc. Equip.*, vol. 823, pp. 15–19, 2016, doi: 10.1016/j.nima.2016.03.107.
- [4] H. Wei *et al.*, “Sensitive X-ray detectors made of methylammonium lead tribromide perovskite single crystals,” *Nat. Photonics*, vol. 10, no. 5, pp. 333–339, 2016, doi: 10.1038/nphoton.2016.41.
- [5] Y. He *et al.*, “High spectral resolution of gamma-rays at room temperature by perovskite CsPbBr₃ single crystals,” *Nat. Commun.*, vol. 9, no. 1, 2018, doi: 10.1038/s41467-018-04073-3.
- [6] S. K. Chaudhuri, M. Sajjad, J. W. Kleppinger, and K. C. Mandal, “Charge transport properties in CdZnTeSe semiconductor room-temperature γ -ray detectors,” *J. Appl. Phys.*, vol. 127, no. 24, 2020, doi: 10.1063/5.0006227.
- [7] H. Spieler, *Semiconductor Detector Systems*. 2007.
- [8] Z. He, “Review of the Shockley-Ramo theorem and its application in semiconductor gamma-ray detectors,” *Nucl. Instruments Methods Phys. Res. Sect. A Accel. Spectrometers, Detect. Assoc. Equip.*, vol. 463, no. 1–2, pp. 250–267, 2001, doi: 10.1016/S0168-9002(01)00223-6.
- [9] Z. He, W. Li, G. F. Knoll, D. K. Wehe, J. Berry, and C. M. Stahle, “3-D position sensitive CdZnTe gamma-ray spectrometers,” *Nucl. Instruments Methods Phys. Res. Sect. A Accel. Spectrometers, Detect. Assoc. Equip.*, vol. 422, no. 1–3, pp. 173–178, 1999, doi: 10.1016/S0168-9002(98)00950-4.
- [10] J. D. Eskin, H. H. Barrett, and H. B. Barber, “Signals induced in semiconductor gamma-ray imaging detectors,” *J. Appl. Phys.*, vol. 85, no. 2, pp. 647–659, 1999, doi: 10.1063/1.369198.

- [11] W. Koehler, Z. He, S. O'Neal, H. Kim, L. Cirignano, and K. Shah, "Digital signal processing in TlBr detectors: Accounting for the motion of holes," *2015 IEEE Nucl. Sci. Symp. Med. Imaging Conf. NSS/MIC 2015*, pp. 2–5, 2016, doi: 10.1109/NSSMIC.2015.7582282.
- [12] Y. Zhu, "Digital Signal Processing Methods for Pixelated 3-D Position Sensitive Room-Temperature Semiconductor Detectors," *PhD Thesis Univ. Michigan*, pp. 1–203, 2012, [Online]. Available: papers3://publication/uuid/B3220D9C-3012-4C2D-9276-A92EFA230813.
- [13] B. Williams, Y. F. Zhu, and Z. He, "Applications of principal component analysis for energy reconstruction in position-sensitive semiconductor detectors," *Nucl. Instruments Methods Phys. Res. Sect. A Accel. Spectrometers, Detect. Assoc. Equip.*, vol. 954, no. April 2019, 2020, doi: 10.1016/j.nima.2019.04.002.
- [14] A. E. Bolotnikov *et al.*, "Rejecting incomplete charge-collection events in CdZnTe and other semiconductor detectors," *Nucl. Instruments Methods Phys. Res. Sect. A Accel. Spectrometers, Detect. Assoc. Equip.*, 2012, doi: 10.1016/j.nima.2011.10.066.
- [15] H. Yang and Z. He, "Identification and reconstruction of Single-Pixel incomplete charge collection events," *IEEE Trans. Nucl. Sci.*, 2013, doi: 10.1109/TNS.2013.2251899.
- [16] J. Yang, Y. L. Li, Y. Tian, L. Xu, Y. M. Cai, and Y. J. Li, "Identification of single-pixel incomplete charge collection events by using cathode waveform in pixelated CdZnTe detectors," *J. Instrum.*, 2020, doi: 10.1088/1748-0221/15/09/P09017.
- [17] C. L. Thrall, W. R. Kaye, Z. He, H. Kim, L. Cirignano, and K. Shah, "Transient behavior in TlBr gamma-ray detectors and its analysis using 3-D position sensing," *IEEE Trans. Nucl. Sci.*, vol. 60, no. 2, pp. 1162–1167, 2013, doi: 10.1109/TNS.2012.2220567.
- [18] H. Kim *et al.*, "Thallium Bromide Gamma-Ray Spectrometers and Pixel Arrays," *Front. Phys.*, vol. 8, no. March, 2020, doi: 10.3389/fphy.2020.00055.
- [19] K. Hitomi, M. Matsumoto, O. Muroi, T. Shoji, and Y. Hiratate, "Thallium bromide optical and radiation detectors for X-ray and gamma-ray spectroscopy," *IEEE Trans. Nucl. Sci.*, vol. 49 II, no. 5, pp. 2526–2529, 2002, doi: 10.1109/TNS.2002.803851.
- [20] K. Hitomi, Y. Kikuchi, T. Shoji, and K. Ishii, "Polarization phenomena in TlBr detectors," *IEEE Trans. Nucl. Sci.*, vol. 56, no. 4, pp. 1859–1862, 2009, doi: 10.1109/TNS.2009.2013349.
- [21] B. Dönmez, C. L. Thrall, Z. He, L. J. Cirignano, H. Kim, and K. S. Shah, "Investigation of polarization effect with TlBr detectors at different operating temperatures," *IEEE Nucl. Sci. Symp. Conf. Rec.*, pp. 3773–3775, 2010, doi:

10.1109/NSSMIC.2010.5874517.

- [22] A. M. Conway *et al.*, “Fabrication methodology of enhanced stability room temperature TlBr gamma detectors,” *IEEE Trans. Nucl. Sci.*, vol. 60, no. 2, pp. 1231–1236, 2013, doi: 10.1109/TNS.2013.2252363.
- [23] J. Vaitkus *et al.*, “Investigation of degradation of electrical and photoelectrical properties in TlBr crystals,” *Nucl. Instruments Methods Phys. Res. Sect. A Accel. Spectrometers, Detect. Assoc. Equip.*, vol. 531, no. 1–2, pp. 192–196, 2004, doi: 10.1016/j.nima.2004.06.004.
- [24] W. Koehler *et al.*, “Quantitative investigation of room-temperature breakdown effects in pixelated TlBr detectors,” *IEEE Trans. Nucl. Sci.*, vol. 61, no. 5, pp. 2573–2578, 2014, doi: 10.1109/TNS.2014.2348535.
- [25] C. R. Leão and V. Lordi, “Ionic current and polarization effect in TlBr,” *Phys. Rev. B - Condens. Matter Mater. Phys.*, vol. 87, no. 8, pp. 25–28, 2013, doi: 10.1103/PhysRevB.87.081202.
- [26] X. W. Zhou *et al.*, “Molecular dynamics discovery of an extraordinary ionic migration mechanism in dislocation-containing TlBr crystals,” *Phys. Chem. Chem. Phys.*, vol. 22, no. 2, pp. 599–606, 2020, doi: 10.1039/c9cp04560k.
- [27] Y. He *et al.*, “CsPbBr₃ perovskite detectors with 1.4% energy resolution for high-energy γ -rays,” *Nat. Photonics*, vol. 15, no. 1, pp. 36–42, 2021, doi: 10.1038/s41566-020-00727-1.
- [28] J. T. Tisdale *et al.*, “Methylammonium Lead Tribromide Single Crystal Detectors towards Robust Gamma-Ray Photon Sensing,” *Adv. Opt. Mater.*, vol. 8, no. 10, pp. 1–9, 2020, doi: 10.1002/adom.202000233.
- [29] V. Gerrish, “Polarization and gain in mercuric iodide gamma-ray spectrometers,” *Nucl. Inst. Methods Phys. Res. A*, vol. 322, no. 3, pp. 402–413, 1992, doi: 10.1016/0168-9002(92)91205-N.
- [30] S. O’Neal, Z. He, and C. Leak, “Analysis of high-energy tailing in TlBr detectors,” *IEEE Trans. Nucl. Sci.*, vol. 65, no. 3, pp. 955–960, 2018, doi: 10.1109/TNS.2018.2804165.
- [31] V. Lordi, “Point defects in Cd(Zn)Te and TlBr: Theory,” *J. Cryst. Growth*, vol. 379, pp. 84–92, 2013, doi: 10.1016/j.jcrysgro.2013.03.003.
- [32] C. Zheng and O. Rubel, “Ionization Energy as a Stability Criterion for Halide Perovskites,” 2017.
- [33] Y. Zhu, S. E. Anderson, and Z. He, “Sub-pixel position sensing for pixelated, 3-D position sensitive, wide band-gap, semiconductor, gamma-ray detectors,” *IEEE Trans. Nucl. Sci.*, vol. 58, no. 3 PART 3, pp. 1400–1409, 2011, doi:

10.1109/TNS.2011.2132738.

- [34] V. T. Jordanov and G. F. Knoll, "Digital synthesis of pulse shapes in real time for high resolution radiation spectroscopy," *Nucl. Inst. Methods Phys. Res. A*, 1994, doi: 10.1016/0168-9002(94)91011-1.
- [35] W. Koehler, "Thallium Bromide as an Alternative Material for Room-Temperature Gamma-Ray Spectroscopy and Imaging," *Diss. U. Mich.*, 2016.
- [36] S. O'Neal *et al.*, "Improvements in room temperature lifetime of pixelated TlBr detectors from surface etching," *2015 IEEE Nucl. Sci. Symp. Med. Imaging Conf. NSS/MIC 2015*, 2016, doi: 10.1109/NSSMIC.2015.7582270.
- [37] A. Datta, P. Becla, and S. Motakef, "Visualization of TlBr ionic transport mechanism by the Accelerated Device Degradation technique," *Nucl. Instruments Methods Phys. Res. Sect. A Accel. Spectrometers, Detect. Assoc. Equip.*, vol. 784, pp. 37–43, 2015, doi: 10.1016/j.nima.2015.01.021.
- [38] W. Koehler, M. Streicher, S. O'Neal, and Z. He, "A Correction Factor to the Two-Bias Method for Determining Mobility-Lifetime Products in Pixelated Detectors," *IEEE Trans. Nucl. Sci.*, vol. 63, no. 3, pp. 1832–1838, 2016, doi: 10.1109/TNS.2016.2548420.
- [39] J. L. Parker, "General Topics in Passive Gamma-Ray Assay," *Passiv. Nondestruct. Assay Nucl. Mater.*, 1991.
- [40] G. Ariño-Estrada *et al.*, "First Cerenkov charge-induction (CCI) TlBr detector for TOF-PET and proton range verification," *Phys. Med. Biol.*, vol. 64, no. 17, 2019, doi: 10.1088/1361-6560/ab35c4.
- [41] Y. A. Boucher, F. Zhang, W. Kaye, and Z. He, "New measurement technique for the product of the electron mobility and mean free drift time for pixelated semiconductor detectors," *Nucl. Instruments Methods Phys. Res. Sect. A Accel. Spectrometers, Detect. Assoc. Equip.*, vol. 671, pp. 1–5, 2012, doi: 10.1016/j.nima.2011.12.008.
- [42] Y. Sun, S. A. Boggs, and R. Ramprasad, "The intrinsic electrical breakdown strength of insulators from first principles," *Appl. Phys. Lett.*, vol. 101, no. 13, 2012, doi: 10.1063/1.4755841.
- [43] W. Shi, C. Ma, L. Hou, G. Xie, L. Tian, and S. Wu, "Velocity of current filament at the high gain mode of GaAs power photoconductive switches," *Phys. B Condens. Matter*, vol. 406, no. 19, pp. 3741–3744, 2011, doi: 10.1016/j.physb.2011.06.082.
- [44] D. H. Auston, "Picosecond optoelectronic switching and gating in silicon," *Appl. Phys. Lett.*, vol. 26, no. 3, pp. 101–103, 1975, doi: 10.1063/1.88079.
- [45] G. M. Loubriel, F. J. Zutavern, H. P. Hjalmarsen, R. R. Gallegos, W. D. Helgeson,

- and M. W. O'Malley, "Measurement of the velocity of current filaments in optically triggered, high gain GaAs switches," *Appl. Phys. Lett.*, vol. 64, no. 24, pp. 3323–3325, 1994, doi: 10.1063/1.111266.
- [46] J. L. Hudgins, D. W. Bailey, R. A. Dougal, and V. Venkatesan, "Streamer Model for Ionization Growth in a Photoconductive Power Switch," *IEEE Trans. Power Electron.*, 1995, doi: 10.1109/63.406850.
- [47] G. B. Sretenović, I. B. Krstić, V. V. Kovačević, B. M. Obradović, and M. M. Kuraica, "The isolated head model of the plasma bullet/streamer propagation: Electric field-velocity relation," *J. Phys. D. Appl. Phys.*, 2014, doi: 10.1088/0022-3727/47/35/355201.
- [48] L. B. Loeb and J. M. Meek, "The mechanism of spark discharge in air at atmospheric pressure. I," *J. Appl. Phys.*, vol. 11, no. 6, pp. 438–447, 1940, doi: 10.1063/1.1712792.